Assembly of functional centers in the ribosomal 60S subunit

Daniel Musa Wilson

B.S. Molecular Biology and Biotechnology

Clarion University of Pennsylvania

Submitted in partial fulfillment of the requirements for the degree of

Doctor of Philosophy

Department of Biological Sciences

Carnegie Mellon University

November 5, 2020

Thesis Advisor: Dr. John L. Woolford, Jr.

Acknowledgements

Science is never done in isolation, and I would like to thank several people who have been important to my journey.

To Dr. John L. Woolford and Jelena Micic, you both have been mentors from me. Thank you both for teaching me how to be a better scientist and working so closely with me. You two made this all possible.

To my committee members, Dr. Jon Minden, Dr. Joel McManus, Dr. Fred Lanni, and Dr. Andrea Berman, thank you all for your insights, advice, pep talks and overall feedback.

To my current and past labmates, Amber LaPeruta, Fiona Fitzgerlad, and Stephanie Biedka, thank you all for being good friends and colleagues to me. I can't wait to see you all succeed in the things you want.

To my cohort, Amber LaPeruta, Teresa Spix, Iris Yang, Scott Keith, and Manning Huang, I always enjoyed spending time with you all and I'm happy that we experienced this crazy thing called graduate school together.

To my undergraduate lab family, Dr. Douglas Smith, Patrick Sheehan, Emma Carter, Michelle Clay, Becca Dudek, Alex Francette, Brandon Nielson, Wesley Schettler, Marcus Kilwein, and many others, thank you all for making me enjoy science and

helping me believe that I could go on to earn my Ph.D. Especially thanks to Dr. Douglas Smith, who encouraged me to do this.

To my extended family, thank you all for giving me moments to look forward to every year, when we get to spend time together.

To my pets, both here and gone, Jill, Calvin, Tesla, and Toby, (even though you can't read this) thank you for making me happy every single day.

To my wife, Amber Lucas Wilson, I don't know how I could have done this without you. I love you so much and feel so lucky to have met you in the middle of this whole experience. You make me a better person, thank you.

Finally, to my parents, Harold and Diane Wilson, thank you so much for everything that you have given me. Thank you for instilling in me the curiosity and drive necessary to pursue this degree. And thank you for always being there for me, no matter what. I love you both.

Abstract

Ribosomes are evolutionarily ancient nanomachines that are composed of ribosomal RNA (rRNA) and ribosomal proteins (r-proteins), and function to translate the genetic code in the form of mRNA to the functional units of a gene, proteins. Carrying out this task with speed and accuracy requires the rRNA to be folded and positioned precisely so that it can catalyze the reactions necessary to produce proteins. Therefore, the many complex steps involved in assembling ribosomes can be thought of as being centered around one goal; make sure that the rRNA matures properly.

R-proteins and assembly factors are proteins that evolved to ensure that the rRNA matures and stabilizes into functional centers, which carry out the various tasks of translation. For example, the small (40S) subunit of the ribosome contains the decoding center, which translates the genetic code in mRNA, while the large (60S) subunit contains the peptidyl transferase center (PTC), which synthesizes proteins. Answering questions concerning how these functional centers form and mature in eukaryotic cells has only become possible in recent years, thanks to advancements in cryo-electron microscopy (cryo-EM), a technique that enables researchers to visualize immature ribosomes in their native states.

My work discussed in this dissertation focuses on how the nascent polypeptide exit tunnel (NPET), another functional center of the 60S subunit, is assembled in the baker's yeast, *Saccharomyces cerevisiae*. This functional center acts as a passageway for newly synthesized protein chains to thread out of the large subunit and into the cytoplasm of the cell, where the protein then begins to fold. It is also the target of many antibiotics, including erythromycin. Far from being a passive tunnel, the NPET actively

interacts with proteins as they are being synthesized. These interactions are crucial in guiding early folding stages of proteins as well as situational control of gene expression.

By mutating r-protein L4 and assembly factors Nog1, Rei1, and Reh1 found inside the NPET and studying the mutant immature ribosomes using biochemistry and cryo-EM, my work revealed that a particular rRNA helix in the NPET (H74) must mature properly for the large subunit to complete maturation. These studies were the first to use cryo-EM to study how a mutation in a functional center affects ribosome assembly. The model I have built from these data has laid a foundation for future exploration of how functional centers are constructed during ribosome assembly.

TABLE OF CONTENTS

List of figures

List of tables

Chapter 1: INTRODUCTION

Entering the structural age of ribosome assembly

Ribosomes are composed of a small (40S) and large (60S) subunit which, together, translate the genetic code to produce proteins in all organisms. In eukaryotes, ribosome assembly starts in the nucleolus, a membrane-less compartment in the nucleus of the cell, and ends in the cytoplasm. This process begins with transcription of ribosomal DNA (rDNA) genes into ribosomal RNA (rRNA). Transcription of rDNA seeds formation of the nucleolus with co-transcriptional binding of ribosomal proteins (r-proteins) and assembly factors (AFs) to the rRNA transcript (Frottin et al., 2019; Peña et al., 2017; Woolford and Baserga, 2013). Binding of both r-proteins and AFs to the rRNA is necessary to fold, cut, trim, modify, and structure the rRNA, and occurs in a semi-hierarchical order (Duss et al., 2019; Gamalinda et al., 2014; Rodgers et al., 2019). While r-proteins remain in the ribosome as part of the mature structure and have no enzymatic activity, AFs bind to assembling ribosomes to perform one or more functions and are then released before maturation is complete. The crystal structure of the mature *S. cerevisiae* (yeast) ribosome revealed the structure and binding location of each r-protein along with the mature rRNA (Jenner et al., 2012), but cryo-EM structures of immature ribosomes bound to AFs have only recently been published (Barrio-Garcia et al., 2015; Greber et al., 2016, 2012; Kater et al., 2020, 2017; Leidig et al., 2014; Liang et al., 2020; Ma et al., 2017; Sanghai et al., 2018; Wu et al., 2016; Zhou et al., 2018). These cryo-EM structures have transformed the field of ribosome assembly.

Before advances in cryo-EM technology, the field of ribosome assembly depended heavily on biochemistry, molecular genetics, and crystal structures of the mature ribosome. Together, these methods uncovered fundamental principles of ribosome assembly that hold true to this day (Gamalinda and Woolford, 2014a; Strunk and Karbstein, 2009; Wilson et al., 2011; Woolford and Baserga, 2013). However, seeing really is believing, and cryo-EM offered the very first glimpses of what assembly factors, rRNA, and ribosomal proteins actually look like when bound to immature ribosomes (Kühlbrandt, 2014). For example, with a single experiment, the first atomic resolution cryo-EM structure of an immature 60S subunit revealed the structure of 17 never before seen AFs (Wu et al., 2016). No other experimental method offers nearly as much insight into ribosome assembly as cryo-EM. As a result, decades of previously gathered data were vindicated, new observations were made, and questions never before imagined became answerable (Biedka et al., 2017; Greber, 2016; Klinge and Woolford, 2019; Peña et al., 2017).

In just the past ~5 years, a total of 22 high-resolution wild type and 17 high-resolution mutant structures of yeast immature 60S subunits have been published (Barrio-Garcia et al., 2015; Greber et al., 2016; Kater et al., 2020, 2017; Ma et al., 2017; Micic et al., 2020; Sanghai et al., 2018; Thoms et al., 2018; Wilson et al., 2020; Wu et al., 2016; Zhou et al., 2018). **Table 1** lists the tagged proteins used to purify these particles along with their PDB code, reference, and subcellular localization. In this thesis, I will focus on two principles that have been consistently observed across all wild-type particles analyzed so far. These principles concern functional centers, structural features of the ribosome that carry out specific functions during translation: 1) AFs seem to cluster around functional centers and 2) rRNA making up functional centers does not

adopt mature conformations until late in assembly. These simple observations drove the major questions that led to the work presented in this thesis.

Table 0.1 Relevant cryo-EM particles of yeast pre-60S ribosomal subunits

Particle Name	EMD Code	PDB Code	Cellular Compartment	Resolution (Å)	Reference
Nsa1 State 2	7324	6C0F	Nucleolus	3.7	Sanghai *et al.* 2018
Nsa1 State 3	7445	6CB1	Nucleolus	4.6	Sanghai *et al.* 2018
Rpf1 Particle	6878	5Z3G	Nucleolus	3.65	Zhou *et al.* 2019
Nsa1 State A	3888	6EM3	Nucleolus	3.2	Kater *et al.* 2017
Nsa1 State B	3889	6EM4	Nucleolus	4.1	Kater *et al.* 2017
Nsa1 State C	3893	6EM1	Nucleolus	3.6	Kater *et al.* 2017
Nsa1 State D	3890	6EM5	Nucleolus	4.3	Kater *et al.* 2017
Nsa1 State E	3891	6ELZ	Nucleolus	3.3	Kater *et al.* 2017
State NE1	10841	6YLX	Nucleolus	3.9	Kater *et al.* 2020
State NE2	10842	6YLY	Nucleolus	3.8	Kater *et al.* 2020
Nog2 State 1	6615	3JCT	Nucleolus/ Nucleoplasm	3.08	Wu *et al.* 2016
Nog2 State 2	6616	n/a	Nucleoplasm	6.6	Wu *et al.* 2016

Rix1-Rea1 Particle	3199	6YLH	Nucleoplasm	3.1	Barrio-Garcia *et al.* 2016 & Kater *et al.* 2020
Rix1ΔC Particle	3200	n/a	Nucleoplasm	11.2	Barrio-Garcia *et al.* 2016
Rea1 K1089A Particle	3203	n/a	Nucleoplasm	8.9	Barrio-Garcia *et al.* 2016
Arx1 Particle	2528	4V7F	Nucleoplasm	8.7	Leidig *et al.* 2014
Cgr1Δ	0221	n/a	Nucleoplasm	12.0	Thoms *et al.* 2018
Cgr1Δ RRS1E102D	0222-0224	n/a	Nucleoplasm	14.0	Thoms *et al.* 2018
State C1	30110	n/a	Nucleoplasm	6.0	Micic *et al.* 2020
State C2	30111	n/a	Nucleoplasm	5.9	Micic *et al.* 2020
State C3	30112	n/a	Nucleoplasm	3.9	Micic *et al.* 2020
State C4	30108	6M62	Nucleoplasm	3.20	Micic *et al.* 2020
State E1	30113	n/a	Nucleoplasm	5.9	Micic *et al.* 2020
State E2	30109	n/a	Nucleoplasm	4.8	Micic *et al.* 2020

State N1	30172	n/a	Nucleoplasm	3.00	Wilson *et al.* 2020
State N2	30173	n/a	Nucleoplasm	4.25	Wilson *et al.* 2020
State N3	30175	n/a	Nucleoplasm	3.77	Wilson *et al.* 2020
State N4	30176	n/a	Nucleoplasm	4.21	Wilson *et al.* 2020
State R1	30170	7BT6	Nucleoplasm	3.12	Wilson *et al.* 2020
State R2	30174	7BTB	Nucleoplasm	3.22	Wilson *et al.* 2020
Late Nuclear	0369	6N8J	Nucleoplasm	3.5	Zhou *et al.* 2019
Early Cytoplasmic Immediate	0370	6N8K	Cytoplasm	3.6	Zhou *et al.* 2019
Early Cytoplasmic Late	0371	6N8L	Cytoplasm	3.6	Zhou *et al.* 2019
Pre-Lsg1	0372	6N8M	Cytoplasm	3.6	Zhou *et al.* 2019
Lsg1-Engaged	0373	6N8N	Cytoplasm	3.8	Zhou *et al.* 2019
Rpl10-Inserted	0374	6N8O	Cytoplasm	3.5	Zhou *et al.* 2019
Nmd3 Particle	9569	5H4P	Cytoplasm	3.07	Ma *et al.* 2017

Rei1 Particle	3152	5APN	Cytoplasm	3.91	Greber *et al.* 2016

Assembly and function of functional centers

Functional centers of the ribosome are composed mostly of rRNA and a few select r-proteins. These centers perform dynamic or catalytic functions essential to translation. However, it is thought that rRNA is sufficient for any catalytic activity that functional centers perform. Here, I propose that there are 5 structural features of the large subunit that can be treated as functional centers; the peptidyl transferase center (PTC), nascent polypeptide exit tunnel (NPET), GTPase activating center (GAC), L1 stalk, and the 5S ribonucleoprotein particle (RNP) (**Figure 1.1**). In this section I will summarize what is known about the functions of each functional center, how they mature during ribosome assembly, and what questions might be answered by future studies.

1.1.1 Function and assembly of the peptidyl transferase center

In eukaryotes, the peptidyl transferase center (PTC) is composed almost entirely of rRNA and r-proteins, L10 (uL16) and L3 (uL3). However, rRNA is thought to be sufficient for the catalytic activity of the PTC, likely making it one of the most ancient ribozymes (enzymatic RNA molecules) in the natural world. The PTC catalyzes two reactions in protein synthesis, peptide bond formation and peptide release (Polacek and Mankin, 2005). The protein synthesis reaction happens when an aminoacyl-tRNA anticodon enters the A-site and is matched to its codon in the decoding center of the small subunit. The ester bond linking the 3’ hydroxyl of the 3’ terminal ribose of the P-site tRNA undergoes aminolysis through a series of short-lived intermediates (Polacek and

Mankin, 2005). In bacteria, this series of reactions take place at an unimaginable speed of about 15-50 peptide bonds per second (Katunin et al., 2002). The peptide release reaction is driven by a nucleophilic attack from the oxygen in a water molecule. This reaction is less favorable than protein synthesis and requires precise coordination of the water molecule by the rRNA of the ribosomal PTC. The catalytic rate constant of peptide release has been measured in *in-vitro* assays occurring as fast as 0.5-1.5 per second for bacterial ribosomes (Zavialov et al., 2002). Nucleic acid base A2602 (A2971 in yeast) of the 23S rRNA in *Escherichia coli* large ribosomal subunits is thought to be especially important in coordination of these reactions (Polacek and Mankin, 2005). These facts highlight the precise positioning of rRNA required to carry out these reactions with such extreme efficiency and fidelity. This precise positioning of rRNA in the large subunit is guided during assembly by AFs and r-proteins.

The rRNA that makes up the PTC includes bases from helices 89, 90, and 93 and the linkers between them (**Figure 1.2**). In cryo-EM structure of assembling pre-60S subunits, these rRNAs only begin to become visible when the AF and GTPase Nog1 binds to Nsa1 state C particles (**Table 1**). At this point, rRNA helices 89 and 90 are visible and the N-terminal 4-helix bundle splits rRNA helix 89 in half (**Figure 1.2a**) (Wu et al., 2016). This splitting of rRNA helix 89 by the 4-helix bundle prevents maturation of this part of the PTC until Nog1 is released from pre-60S subunits during cytoplasmic stages of assembly by the AAA-ATPase Drg1 (Kappel et al., 2008; Lo et al., 2010). Once Nog1 is released, it is replaced by the AF Nmd3 and pre-60S subunits are exported into the cytoplasm. Nmd3 interacts with helix 89 via a histidine thumb motif and causes helix 89 to undergo several subtle rearrangements before being released by the

GTPase Lsg1 in one of the last steps of 60S subunit assembly (Hedges et al., 2005; Zhou et al., 2018).

More of the rRNA making up the PTC (helix 93) becomes visible in Nsa1 states D and E (**Figure 1.2a**), coinciding with the entry of AFs Noc3, Spb1, Nop2, and Nip7 (Kater et al., 2017). The binding of these AFs is likely responsible for stabilizing helix 93, which adopts a near mature conformation at this stage in assembly (Kater et al., 2017). The presence of assembly factors such as Nop2 and Nip7 prevents further maturation of the PTC rRNA. Nop2 and Nip7 must be released in order for the large junction of rRNA helices connected to H73 and 74 to undergo a dramatic rearrangement, which places helices 73 and 74 in near mature conformations. Once helices 73 and 74 have moved out of the way, the PTC is freed to bind downstream essential assembly factors.

In Nog2 state 1, all rRNA helices belonging to the PTC have become visible, including the linker between helix 89 and 90 (Wu et al., 2016). During these nucleolar/nucleoplasmic stages of large ribosomal subunit assembly, the immature PTC is bound by at 3 different GTPases, Nog1, Nog2, and Nug1, and the AF Nsa2 (**Figure 1.2a**). The presence of these AFs in the PTC prevents it from performing any reactions before the large subunit reaches maturity and likely are necessary to guide the rRNA to its proper conformation while avoiding non-productive kinetic traps from forming. Consistent with this interpretation, homologs of these GTPase AFs appear to be the last factors removed from the bacterial large subunit (Feng et al., 2014; Li et al., 2013; Zhang et al., 2014). Enzymatic functions of Nog2 and the AAA-ATPase Rea1 are thought to drive release of these AFs around the PTC just prior to export from the nucleus (Manikas et al., 2016; Matsuo et al., 2014). Once these AFs are released, the PTC is bound again by Nmd3, an AF essential for export of the pre-60S subunit from the nucleus to the

cytoplasm (Lo et al., 2010). In the cytoplasm, RP L10 (uL16) is loaded into the cleft between the 5S RNP and the P-stalk and extends an internal loop into the P-site (Patchett et al., 2017; Zhou et al., 2018). In fact, several RP internal loops seem to reach toward the PTC prior to loading of L10, including L3 (uL3), L16 (uL10), and L23 (uL23) (**Figure 1.2b**) This addition of L10 completes the PTC, but the PTC cannot function until all AFs bound to it have been released. This task is accomplished by the GTPase, Lsg1, which facilitates release of Nmd3 from pre-60S subunits (Hedges et al., 2005; Malyutin et al., 2017).

Certain residues in the PTC are also modified by methyltransferase AFs, such as Spb1 and Nop2, during assembly (Lapeyre and Purushothaman, 2004). However, the significance of these modifications during assembly is not well understood, so they are not discussed in detail here.

Overall, assembly of the PTC requires AFs to guide the stabilization, folding, and positioning of rRNA. Once the proper conformations are achieved, L10 is loaded onto pre-60S subunits and the final AFs are released. This reflects what has been found in bacterial ribosomes, where the PTC is heavily bound by AFs throughout ribosome assembly and is not licensed for function until the final stages of maturation (Jomaa et al., 2014). These structural observations have laid the groundwork for investigation into how exactly these proteins facilitate formation of the PTC. While mutations in L10 are known to be associated with T-cell leukemia (Patchett et al., 2017), no precise mutations

have yielded any insight into the detailed functions of PTC-binding AFs. Future structural studies of such mutants will hopefully offer answers to these questions.

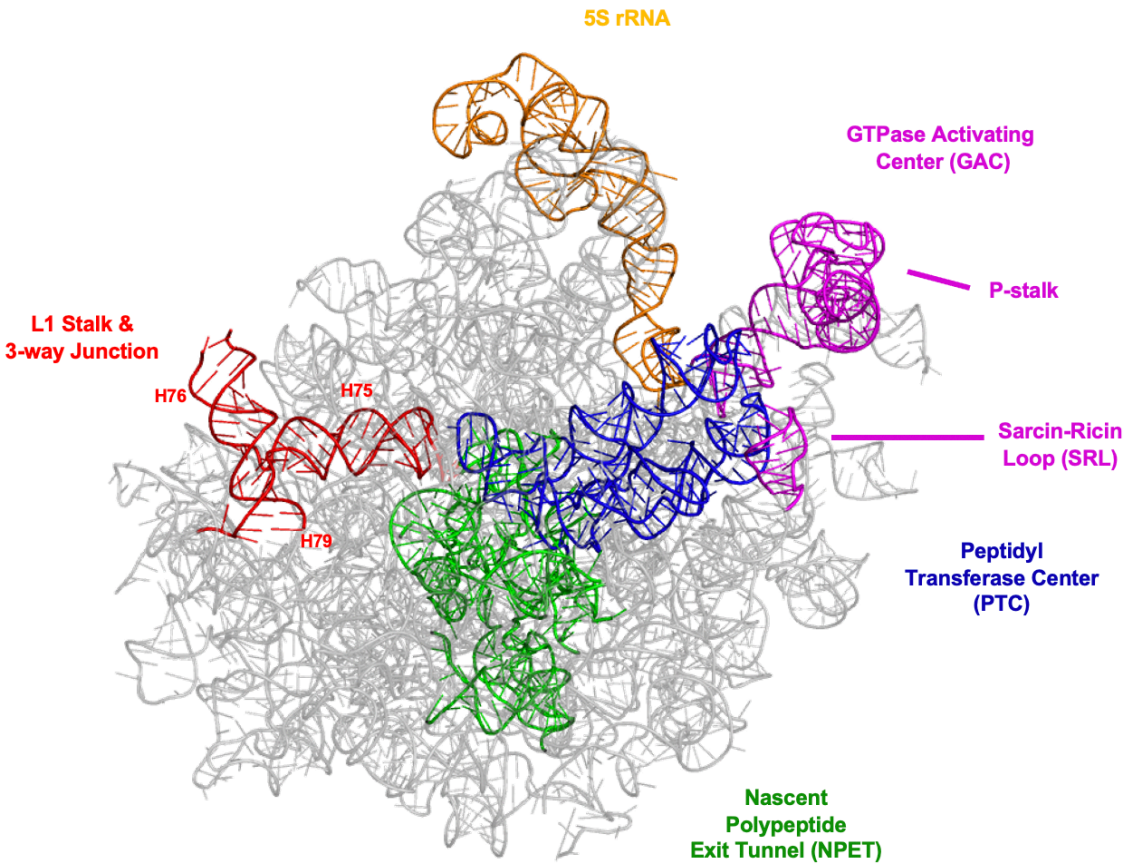

Figure 0.1 Functional centers of the large ribosomal subunit.

The mature 25S, 5.8S, and 5S rRNAs of the large ribosomal subunit shown apart from any ribosomal proteins (PDB: 4V88). Only a portion of the L1 stalk (H76) is resolved in this structure.

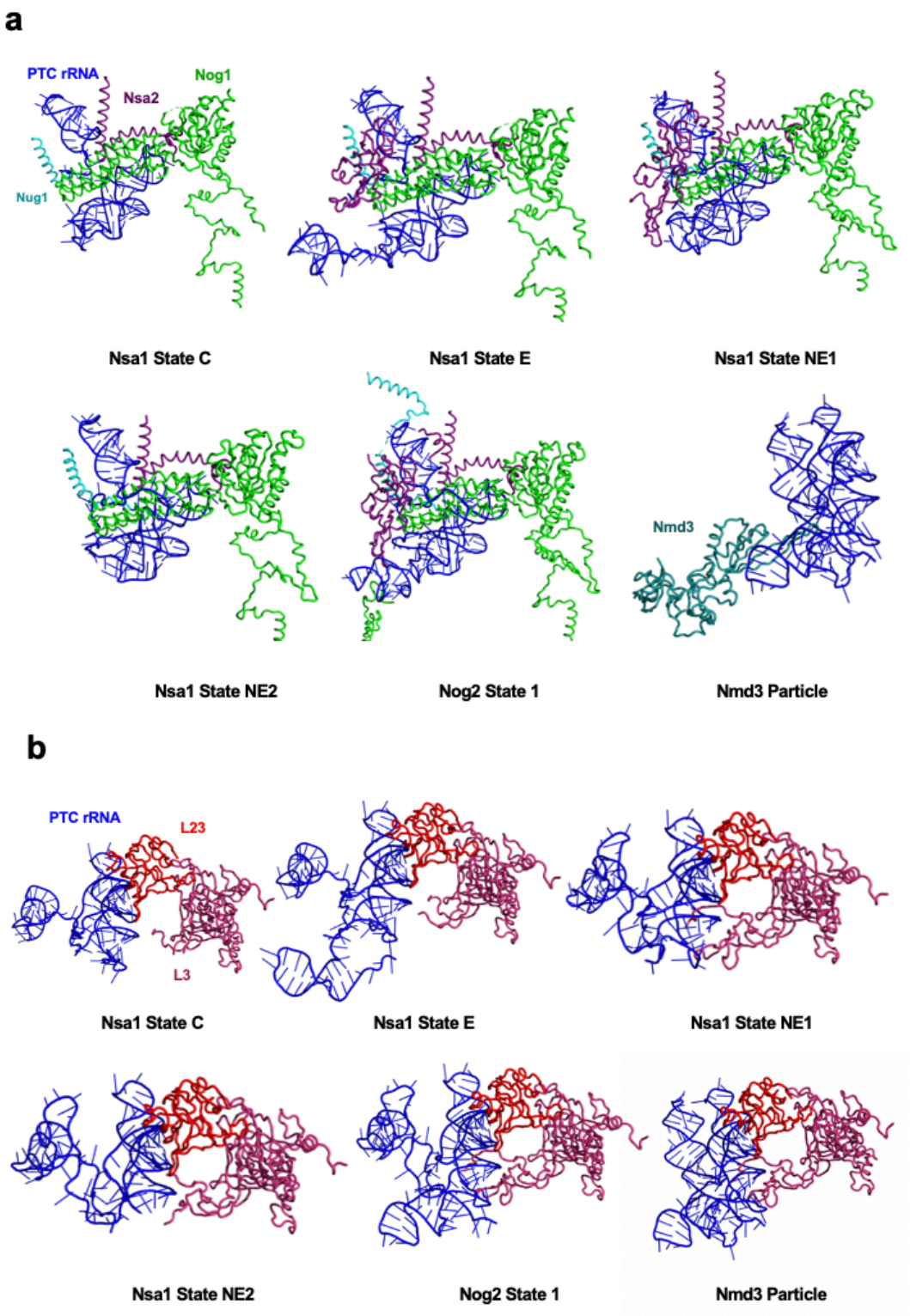
a
PTC rRNA
Nog1
Nsa2
Nug1
Nsa1 State C
Nsa1 State E
Nsa1 State NE1
Nsa1 State NE2
Nog2 State 1
Nmd3
Nmd3 Particle
b
PTC rRNA
L23
L3
Nsa1 State C
Nsa1 State E
Nsa1 State NE1
Nsa1 State NE2
Nog2 State 1
Nmd3 Particle

Figure 0.2 Assembly of the peptidyl transferase center.

(a) Ordered stages of assembly of the rRNA corresponding to the peptidyl transferase center (PTC) (blue), showing its interactions with assembly factors. **(b)** The same rRNA shown in **a**, depicting its interactions with ribosomal proteins as assembly proceeds. For the sake of displaying relevant portions of the proteins, the angles may not be identical across all panels.

1.1.2 Function and assembly of the nascent polypeptide exit tunnel

Nascent polypeptide chains synthesized in the PTC must be threaded out of the large subunit and into the cytoplasm where they can fold into a tertiary structure. The nascent polypeptide exit tunnel (NPET) provides a path from the PTC to the cytoplasm. The dimensions of the tunnel across all domains of life are, on average, 88.8 (+/- 6.0) angstroms long with a radius of 5.4 (+/- 0.4) angstroms (Dao Duc et al., 2019). The shape of the NPET roughly resembles that of a wine glass from bottom to top. The region closest to the PTC is rather narrow, with a radius on the order of ~2-4 angstroms, while the end that the nascent chain emerges from is wider, with a radius on the order of ~4-8 angstroms (Dao Duc et al., 2019).

Many biologists may think of the NPET as a passive conduit that hardly qualifies as a functional center. However, it has become increasingly clear over the past ~20 years that the NPET can actively interact with the growing nascent chain and function as a sensor of both specific polypeptide sequences and small molecular effectors, such as antibiotics, to modulate activity of the PTC and regulate the synthesis of particular proteins (Mankin, 2006; Vázquez-Laslop and Mankin, 2018). Examples of this can be found in both prokaryotes and eukaryotes (Mankin, 2011; Seefeldt et al., 2016; Su et al., 2017; Wilson et al., 2011; Wilson and Beckmann, 2011; Wu et al., 2012). It has also become clear that the dimensions of the NPET can influence protein folding as translation is occurring (Liutkute et al., 2020). Important for these functions are the constriction sites in the NPET (one for prokaryotes and two for eukaryotes) formed by the internal loops of RPs L4 (uL4) and L17 (uL22) (Dao Duc et al., 2019). The constriction sites are characterized by a narrowing of the NPET such that the internal

loops of L4 and L17 can interact with the nascent chain in order to coordinate ribosome stalling events (Davis et al., 2014; Seefeldt et al., 2015; Su et al., 2017; Wilson et al., 2011). In addition to L4 and L17, RP L39 (eL39), which is only found in eukaryotic ribosomes, also sits towards the wide end of the NPET (Jenner et al., 2012). The rest of the NPET, and thus the majority, is made up of rRNA from five of the six domains of 25S rRNA (**Figure 1.3b**). The rRNA nucleotides making up the NPET are more evolutionarily conserved on the side closer to the PTC and less conserved toward the tunnel exit (Dao Duc et al., 2019). Misassembling the NPET and its various dimensions can have severe negative consequences for gene expression, protein folding, and health (Liutkute et al., 2020).

Cryo-EM of pre-60S particles has offered a step-by-step manual for constructing the NPET (**Figure 1.3a**). The earliest precursor to a mature NPET can be seen in cryo-EM structures of Nsa1-associated particles, purified from early nucleolar stages of 60S subunit assembly. Nsa1 state 2 reveals an incomplete tunnel, consisting of rRNA mostly from domains I and II. At this stage, the tunnel domains (TDs) of L4 and L17, which form the constriction sites, are not visible and the AF Rrp14 can be seen in close proximity to the NPET, presumably preventing further maturation (Sanghai et al., 2018). In Nsa1 state C, the TD of L4, but not L17, becomes visible (more stable) and the N-terminus of AF Rpf1 can be seen occupying the lower portion of the NPET (Kater et al., 2017). Currently, there is no known function for the N-terminus of Rpf1. Next, in Nsa1 state E, most of the rRNA from domains II, III, and V that will compose the mature NPET are visible but are not yet in their mature positions. The TD of L17 also becomes more stable at this point, Rpf1 has been removed, and the C-terminus of Spb1 hooks into the upper portions of the NPET to interact with the TD of L4 and come into close proximity with the

TD of L17. Although not stated in the original publication, further examination of Nsa1 state E density maps reveal a strong argument for the loading of the eukaryotic-specific RP L39 during this time in assembly (**Figure 1.3a**). This suggests that removal of Rpf1 form the pre-60S ribosomal subunit may be a trigger for L39 to enter the NPET. Following state E are states NE1 and NE2 (Kater et al., 2020). In state NE1, L39 can more clearly be seen loaded into the lower, wider portion of the tunnel where it binds to rRNA helix 49a, which also becomes visible at this step. The C-terminus of Spb1 is still present in state NE1, but it has shifted in its position. In state NE2, Spb1 has exited the pre-60S subunit, coinciding with slight shifts in tunnel rRNA. All rRNA domains are mostly visible and in near mature positions at this point, except for domain V.

The transition from state NE2 to Nog2 state 1 involves drastic changes to the deeper portion of the NPET, in close proximity to the PTC (Wu et al., 2016). For the first time, domain V tunnel rRNA becomes visible and the long C-terminal extension of Nog1 is inserted into the NPET, interacting with L39 and the TD's of L4 and L17 at the constriction sites, and reaches almost to the PTC. Interestingly, rRNA helices 73 and 74 become visible only when the Nog1 C-terminus enters the NPET (**Figure 1.3a**) (Kater et al., 2020). The entry of the Nog1 C-terminus into the NPET also coincides with the appearance of AFs Arx1 and Alb1 at the binding platform outside of the NPET (Wu et al., 2016). The C-terminus of Nog1 remains inserted in the NPET during major remodeling events including cleavage and removal of the ITS2 spacer rRNA, rotation of the 5S RNP, and export from the nucleoplasm to the cytoplasm (Barrio-Garcia et al., 2015; Biedka et al., 2018; Zhou et al., 2018). Once the pre-60S subunit reaches the cytoplasm, the C-terminus of Nog1 is removed from the NPET by the AAA-ATPase Drg1 while the N-terminus is likely released later by its GTPase activity, although the latter is not

confirmed (Klingauf-Nerurkar et al., 2020; Zhou et al., 2018). Once Nog1 is released from the pre-60S subunit, the globular domain of Rei1 binds outside of the NPET and inserts its C-terminus into the NPET, essentially replacing the C-terminus of Nog1. This swap coincides with slight movements in domain V rRNA in the deepest regions of the NPET (**Figure 1.3b**). The biological significance of these subtle movements remains unclear. Once Rei1 is released, along with Arx1, by the ATPases Ssa1 and Jjj1, the NPET is again probed by the C-terminus of Reh1 (Ma et al., 2017). While the C-termini of Nog1 and Rei1 are conserved from yeast to humans, Reh1 is unique to only a few yeast species (Liang et al., 2020; Parnell and Bass, 2009). The mechanism of Reh1 release from the pre-60S subunit remains unknown, but its removal marks completion of the NPET. The biological significance of these events is discussed in much greater detail in Chapter 2, with a focus on the C-terminus of Nog1 and the tunnel domain of L4.

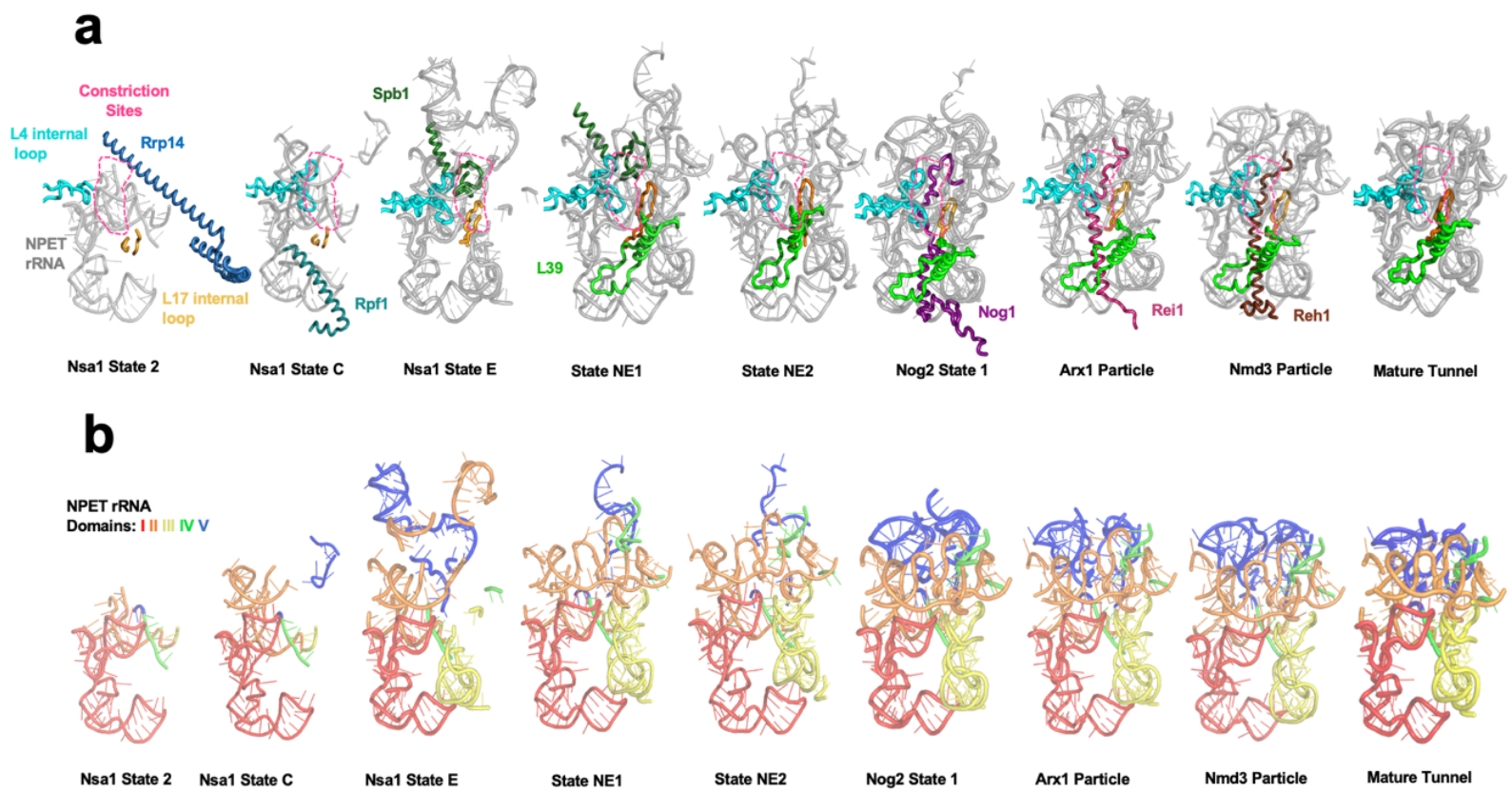
a
Constriction Sites
L4 internal loop
Rrp14
NPET rRNA
L17 internal loop
Spb1
Rpf1
L39
Nog1
Rei1
Reh1
Nsa1 State 2
Nsa1 State C
Nsa1 State E
State NE1
State NE2
Nog2 State 1
Arx1 Particle
Nmd3 Particle
Mature Tunnel
b
NPET rRNA
Domains: I II III IV V
Nsa1 State 2
Nsa1 State C
Nsa1 State E
State NE1
State NE2
Nog2 State 1
Arx1 Particle
Nmd3 Particle
Mature Tunnel

Figure 0.3. Ordered stages of nascent polypeptide exit tunnel assembly.

(a) The rRNA of the nascent polypeptide exit tunnel (NPET) and its interactions with relevant proteins as assembly proceeds. **(b)** The changing rRNA of the NPET color coded to each of the five rRNA domains contained within it. The assembly factors and ribosomal proteins have been removed from this figure in order to appreciate the rearrangements that the rRNA undergoes at each step.

1.1.3 Function and assembly of the GTPase-associated center

During translation, GTPases must be recruited and activated in order to provide energy for mechanical movement required for protein synthesis. Sometimes called the P-stalk, GTPase-activating region, or in this case the GTPase-associated center (GAC), this mobile element of the ribosome performs the aforementioned function and consists of the ribosomal proteins P0 and P1/P2, and a region of rRNA referred to as the sarcin-ricin loop (SRL) (Grela et al., 2019). The GAC is required to activate the GTPases that power the mechanical movements behind tRNA translocation. The GAC accomplishes this by inserting rRNA in the binding pocket of translational GTPases, which helps to position an amino acid (usually a histidine) in a conformation that activates GTP hydrolysis by holding a water molecule in close proximity to the gamma phosphate (Maracci and Rodnina, 2016; Voorhees and Ramakrishnan, 2013).

Assembly of GAC involves relatively few assembly factors and begins in Nsa1 state B, where the SRL in domain VI is visible by cryo-EM and the assembly factor Tif6 can be seen apparently stabilizing it. Next, in Nsa1 state B, the N-terminal, GTPase containing region of Nog1 is visible and the SRL can be seen pointing directly at the GTPase core of Nog1. Although this makes it tempting to speculate that the SRL facilitates GTP hydrolysis of Nog1, there is no further structural evidence to support this idea, despite extensive study by cryo-EM (Zhou et al., 2018). Additionally, rRNA from domain II making up the landing platform (P-stalk region) of the GAC can be seen at this stage, along with L9 (uL6) which can be seen bridging this region of domain II with the SRL in domain VI. Once Nog1 and this domain II rRNA become visible, Mrt4, an AF and paralog of the P0 protein, also binds to the P-stalk. The SRL, Nog1, and Mrt4 do not

undergo any rearrangements until pre-60S subunits reach the cytoplasm. The precise order of the following three steps remains unclear. Once in the cytoplasm, the AAA-ATPase Drg1 removes the AF Rlp24 and the Nog1 C-terminus from the NPET, a step that partially releases Nog1 from pre-60S subunits (Klingauf-Nerurkar et al., 2020). Around this time, the N-terminal domain of Nog1 is released from the PTC, presumably because of GTP hydrolysis, although evidence to support this idea or what activates the Nog1 GTPase activity remains frustratingly elusive (Zhou et al., 2018). These two events, release of the N-terminus and C-terminus of Nog1, appear to be independent of each other (Klingauf-Nerurkar et al., 2020; Zhou et al., 2018). Coinciding with these events, Mrt4 is released from the P-stalk and replaced with Yvh1 (Lo et al., 2010; Zhou et al., 2018). At this time, RP L40 (eL40) has bound between the P-stalk and L9. These events ultimately are completed by the transition from early cytoplasmic-late to pre-Lsg1 particles. Yvh1 remains on pre-60S particles until it is replaced by P0 and P1/P2, completing the GAC (Kemmler et al., 2009; Zhou et al., 2018). This process is visualized in **Figure 1.4**.

Although a thorough structural analysis of these steps in assembly has been done, additional biochemical experiments informed by these new structures have not yet been published. For now, these structures reaffirm previously published data showing that Mrt4 is a placeholder for Yvh1, which is a placeholder for P0. Future studies may help to solve unanswered questions, for example whether or not the orientation of the SRL in relation to the GTPase core of Nog1 holds any biological significance.

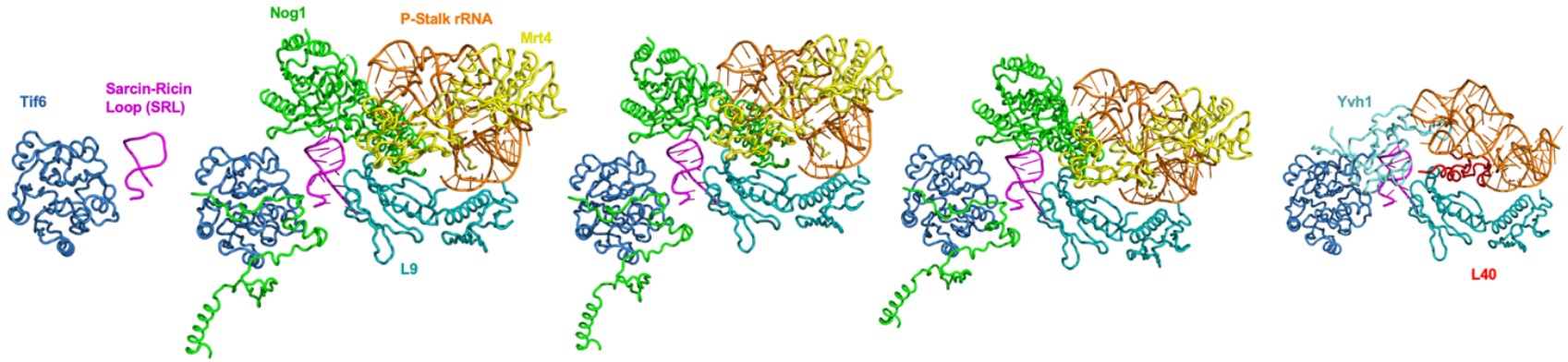
Tif6
Sarcin-Ricin
Loop (SRL)
Nog1
P-Stalk rRNA
Mrt4
L9
Yvh1
L40
Nsa1 State B
Nsa1 State C
Nsa1 State E
Nog2 State 1
Pre-Lsg1

Figure 0.4. Assembly of the GTPase activating center.

The ordered stages of the GTPase activating center (GAC), which includes the P-stalk and sarcin-ricin Loop. Only the relevant ribosomal proteins and assembly factors are shown. Colors of the GAC rRNA do not necessarily correspond to the color schemes assigned to rRNA domains in previous figures.

1.1.4 Assembly and function of the L1 stalk

The L1 stalk is a mobile element of the 60S subunit, composed of rRNA helix 76 and ribosomal protein L1. It is attached to a 3-way junction of H75, 76, and 79, with the helix 75 arm extending into the NPET and PTC via helices 73 and 74. During translation, the L1 stalk swings back and forth, transitioning between an open and a closed state, in order grab and release tRNA molecules from the E site to exit from translating ribosomes (Réblová et al., 2012; Voorhees and Ramakrishnan, 2013). Although this structure is not widely considered to be a functional center of the large subunit, its function during translation provides a strong argument in favor of it being a functional center. Additionally, assembly of the L1 stalk has become a focus of recent work.

During 60S subunit assembly, the L1 stalk undergoes a dramatic rearrangement in the transition from state NE1 to state NE2 (Kater et al., 2020). In state NE1, H74 is held in an immature conformation by Spb1, Nop2, and Nip7. As a result, the entire 3-way junction of rRNA helices 75, 76, and 79, which includes the L1 stalk, is in a flexible state that is difficult to visualize with cryo-EM (**Figure 1.5**). Once Spb1, Nop2, and Nip7 are removed (by an unclear mechanism, but possibly the enzymatic activity of Nop2), the base (helix 74) of this 3-way junction swings a full 45º towards the ITS2 structure and is locked down by ribosomal proteins L2 and L43. After docking into its mature position, the L1 stalk can be seen in an open conformation. During 5S RNP rotation, the next major remodeling event in 60S subunit assembly, multiple assembly factors are recruited to power structural rearrangements (Barrio-Garcia et al., 2015). When Sda1, one of these remodeling factors, binds to pre-60S subunits, the L1 stalk adopts a closed conformation (Barrio-Garcia et al., 2015; Wu et al., 2016). It is not known whether or not these two

events are dependent on each other or even if the closing of the L1 stalk is biologically significant during this particular step. Nevertheless, once Sda1 is released from the pre-60S subunit, the L1 stalk again adopts an open conformation (Wu et al., 2016). This cycle of opening and closing is repeated during cytoplasmic stages with the binding and release of the assembly factor Nmd3 (Malyutin et al., 2017). This movement of the L1 stalk may play essential roles in assembly while also serving as a test drive of functions to be performed during translation. Biochemical studies have only barely begun to address this question (Musalgaonkar et al., 2019).

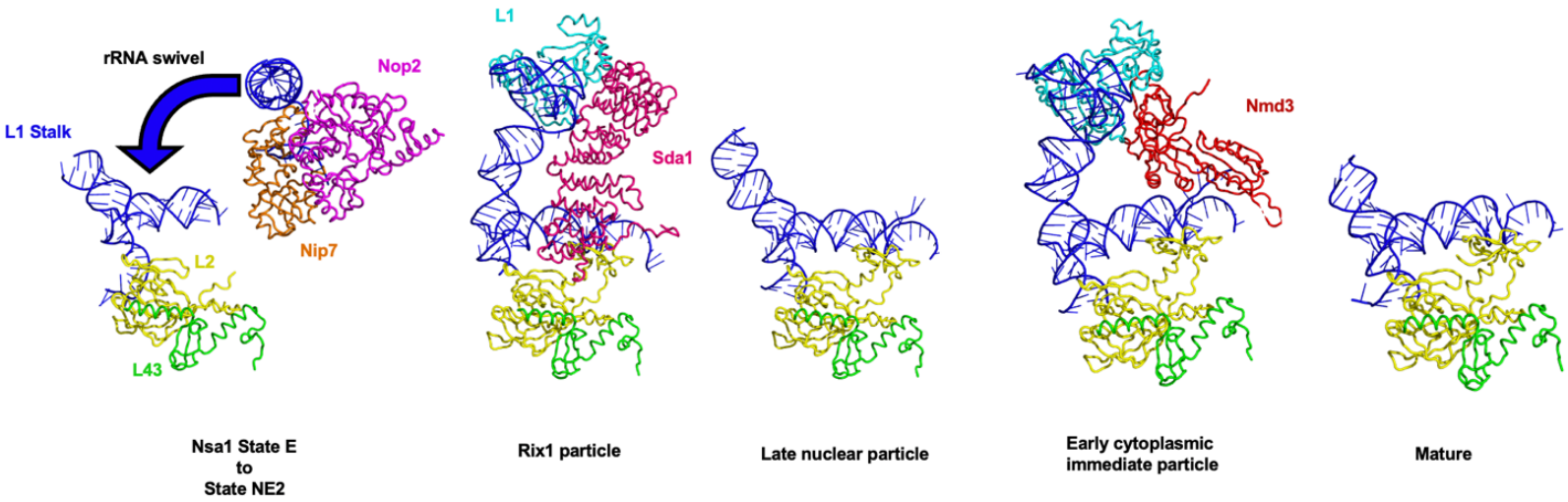
rRNA swivel
Nop2
L1 Stalk
Nip7
L2
L43
L1
Sda1
Nmd3
Nsa1 State E
to
State NE2
Rix1 particle
Late nuclear particle
Early cytoplasmic
immediate particle
Mature

Figure 0.5. Ordered stages of L1 stalk maturation.

The L1 stalk is shown attached to the 3-way junction of rRNA helices 75, 76, and 79 with relevant assembly factors and ribosomal proteins also shown. Ribosomal protein L1 is not resolved in each state, but it is present in each state.

1.1.5 Assembly and function of the 5S ribonucleoprotein particle

The 5S ribonucleoprotein particle (5S RNP), also referred to as the central protuberance, is composed of the 5S rRNA, which is transcribed separately from the other rDNA genes by RNA polymerase III, and RPs L5 and L11 (Woolford and Baserga, 2013). The 5S RNP is the only part of the large subunit that is assembled separately before being loaded onto pre-ribosomes between the GAC and the L1 stalk, and right above the PTC (Jenner et al., 2012). This unique position raises the possibility that the 5S RNP can coordinate communication between all functional centers in the large subunit (Dontsova and Dinman, 2005). Indeed, mutagenesis experiments have supported the idea that 5S rRNA can allosterically receive and react to signals from other functional centers of the large and small subunits (Smith et al., 2001). Additionally, the 5S RNP needs to be autonomous from the ribosome in order to maintain optimal ribosome function, implying that it performs an important role in during translation (Huang et al., 2020). It should be stated that this interpretation of the 5S RNP as a functional center is not universal and some observations go against it, including the fact that mitochondrial ribosomes incorporate a tRNA and only L5 in place of a full, conventional 5S RNP (Kitakawa and Isono, 1991; Koripella et al., 2020). Although the questions of how the 5S RNP functions and whether or not it can be considered a functional center have not yet been clearly answered, this thesis will consider it a functional center based on all of the information discussed in this section.

In order to initially become tethered to the large subunit, the 5S RNP must form a complex with two assembly factors, Rpf2 and Rrs1 (Zhang et al., 2007). This tethering to the pre-ribosome happens relatively early in assembly of the large subunit, but exactly

when it occurs remains unclear, partly because this subcomplex is flexible and thus invisible to cryo-EM during early stages of assembly (Kater et al., 2020, 2017; Sanghai et al., 2018). The mechanisms that free the 3-way junction containing the L1 stalk to swivel into a more mature position are the same mechanisms that open up the steric space required for the 5S RNP to anchor onto the large subunit (Kater et al., 2020). This includes the release of Nop2, Nip7, Brx1, Ebp2, and Noc3, which is presumably initiated by the release of Erb1 and Ytm1 by the AAA-ATPase Rea1 (Kater et al., 2020; Konikkat et al., 2017). Once the 5S RNP is anchored, still in complex with Rpf2 and Rrs1, it is put onto pre-60S subunits backwards relative to its mature position (Leidig et al., 2014). Therefore, the 5S RNP must be rotated ~180º before maturation is complete (**Figure 1.6**). Specifically, it seems that this must occur before export from the nucleoplasm to the cytoplasm (Micic et al., 2020; Thoms et al., 2018). The mechanism of rotation is not entirely clear in the literature, but here it will be described the way I think is best supported by the structural data.

The first thing that must happen to allow rotation is the release of Rpf2 and Rrs1. These assembly factors hold the 5S RNP in a pre-rotated state (Barrio-Garcia et al., 2015; Wu et al., 2016). How this happens is perhaps the most unclear part of the rotation process, but recent structural data have offered clues. Initially, our lab thought that the assembly factor Sda1 competes with Rpf2 for binding sites on the pre-60S subunit. Consistent with this, depletion of Sda1 completely blocks 5S RNP rotation from occurring (Micic et al., 2020). Furthermore, truncation of the C-terminal domain of Rpf2 results in a failure to stabilize rRNA helix 69, which serves as a binding site for Sda1 (Micic et al., 2020). Mutant pre-60S particles lacking the C-terminal domain of Rpf2 also fail to release Rpf2 and Rrs1 and rotate the 5S RNP. The assembly factor Cgr1 has also

been found to help weaken the association of Rpf2 and Rrs1 to pre-60S subunits and facilitate initiation of 5S RNP rotation (Thoms et al., 2018). There is also evidence that the Rix1 complex, which is recruited by Sda1, plays a role in the release of Rpf2 and Rrs1. The N-terminal domain of Ipi1 (a component of the multimeric Rix1 complex) replaces the C-terminal domain of Rpf2 in pre-60S particles that have successfully undergone 5S RNP rotation (Kater et al., 2020). This suggests that the N-terminal domain of Ipi1 helps to dissociate Rpf2 from pre-60S particles after being recruited by Sda1. Possibly making the situation murky, however, is a mutant pre-60S particle containing a C-terminally truncated Rix1. The C-terminal domain of Rix1 is thought to help anchor the Rix1 subcomplex onto pre-60S particles. Cryo-EM has revealed that C-terminal truncation of Rix1 results in pre-60S particles that cannot undergo 5S RNP rotation and have not bound Sda1 (Barrio-Garcia et al., 2015). This inability to rotate may be explained by the fact that the Rix1 complex may not be able to anchor onto pre-60S particles and allow the N-terminal domain of Ipi1 to displace the Rpf2 C-terminus, but the lack of Sda1 is more difficult to explain. However, cryo-EM structures of these particles are low resolution and deserve revisiting.

Once Rpf2 and Rrs1 are released and Sda1 and the Rix1 complex have been bound by the pre-60S subunit, rRNA helix 38 also repositions itself after serving as a placeholder for the 5S rRNA. Last, the AAA-ATPase Rea1 is bound by the pre-60S subunit and Rsa4 repositions its N-terminal domain to face the body of Rea1 (Barrio-Garcia et al., 2015; Wu et al., 2016). These events mark the formation of the Nog2 state 2/Rix1 particle (Barrio-Garcia et al., 2015; Wu et al., 2016). Rea1 and Nog2 assist each other in their nucleotide hydrolysis and release from the pre-60S subunit (Matsuo et al., 2014). This results in the release of Rsa4, Sda1, the Rix1 complex, and Cgr1 from the

pre-60S subunit as well, enabling formation of the Nog2 state 3 particle and completion of the 5S RNP rotation process (Wu et al., 2016). Rotation of the 5S RNP also appears to be coupled to the construction of other functional centers (Micic et al., 2020).

One outstanding question remaining in this model concerns the role that RP L21 (eL21) plays in rotation of the 5S RNP. Depletion of L21 and mutagenesis of its interface with L5 have been shown to block rotation of the 5S RNP (unpublished, see Beril Tutuncuoglu's Thesis). These data have yet to be followed up and could potentially yield more insight into what stabilizes the 5S RNP in a mature, rotated state.

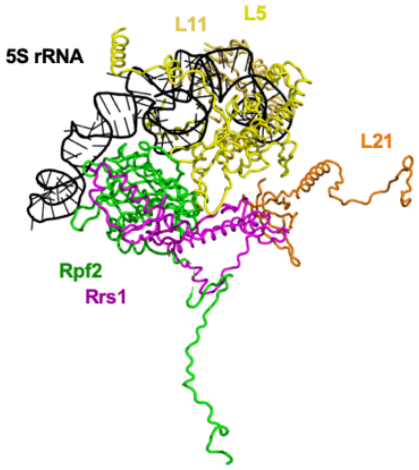

Nog2 State 1

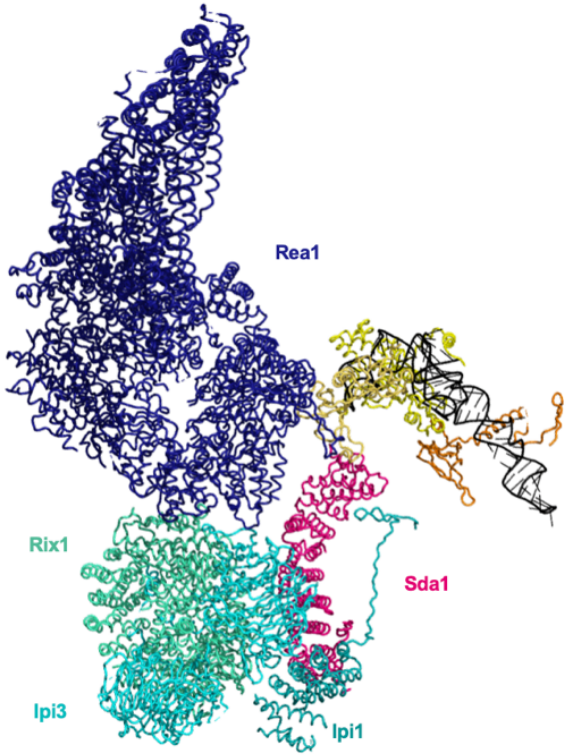

Rix1-Rea1 Particle

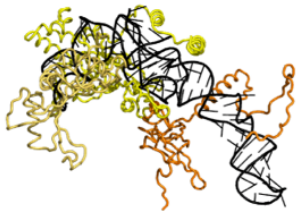

Nmd3 Particle/Mature

Figure 0.6. Maturation of the 5S RNP throughout assembly.

The 5S rRNA is shown in relation to relevant ribosomal proteins and assembly factors. The 180º rotation of the 5S RNP occurs between Nog2 state 1 and the Rix1-Rea1 particle.

How will the field of ribosome assembly move forward?

Just over the past five years, there has clearly been incredible progress in the field of ribosome assembly, thanks in large part to the cryo-EM structures of pre-ribosomal subunits. This progress has made it possible to ask and answer entirely new questions. However, a new challenge has arisen in this structural age. Cryo-EM offers snapshots of assembling ribosomal subunits and most structures have been of wild-type particles. While these wild-type structures are incredibly valuable, they leave wide open critical questions regarding the biological significance of apparently important interactions. For example, hundreds of protein-protein, protein-RNA, or RNA-RNA interactions are visible in each pre-60S whose structure is solved by cryo-EM, yet we have no way of knowing whether or not any particular interaction or combination of interactions play any significant roles in the assembly pathway without accompanying biological assays.

Therefore, the future of ribosome assembly will be a combination of old and new methods. A combination of biochemical, molecular genetic, and structural approaches is sorely needed to test the hypotheses inspired by cryo-EM structures and gain a true understanding of the mechanisms governing ribosome assembly. Using all of these methods to study ribosome assembly mutants will be the state of the art of the ribosome assembly field until the next technological advance shifts the field forward. This advance will likely take the form of a cryo-EM method that enables videos, rather than snapshots, to be obtained from purified pre-ribosomes in high resolution. Currently, such an achievement seems hard to imagine. However, high resolution cryo-EM of pre-ribosomal particles carried the same connotation just a decade ago. The next decade is sure to

bring many exciting discoveries and technologies that will continue to revolutionize ribosome biology and beyond.

Chapter 2: STRUCTURAL INSIGHTS INTO ASSEMBLY OF THE RIBOSOMAL NASCENT POLYPEPTIDE EXIT TUNNEL

The following publication includes some of the results discussed in this chapter.

Wilson, D. M., Y. Li, A. LaPeruta, M. Gamalinda, N. Gao, and J.L. Woolford. Structural insights into assembly of the ribosomal nascent polypeptide exit tunnel. *Nat. Commun.* **11**, 1–15 (2020).

With the exceptions listed below, I performed all biochemical, genetic, and fluorescence microscopy experiments described in this paper, including growth and purification of the *rpl4Δ63-87* protein samples for cryo-EM.

Yu Li performed all electron microscopy and grew and purified pre-ribosomes from the triple tail mutant for cryo-EM, after difficulties shipping samples to Beijing arose on our end.

Amber LaPeruta constructed the triple tail mutant.

Michael Gamalinda performed the northern blot experiments for the *rpl4Δ63-87* mutant.

Introduction

The nascent polypeptide exit tunnel (NPET) is a major functional center of the large ribosomal subunit (see Chapter 1). Work done by Daniel N. Wilson and Alexander Mankin has demonstrated that molecules (such as antibiotics) binding in the NPET can allosterically exert structural changes in the ribosomal RNA (rRNA) of the peptidyl transferase center (PTC), suggesting that the two functional centers can communicate with each other (Gupta et al., 2016; Khaitovich et al., 1999; Su et al., 2017; Vázquez-Laslop and Mankin, 2018; Wilson et al., 2011). These observations, decades ago, could have supported the idea that this communication between the NPET and the PTC could take place during assembly of the large ribosomal subunit. However, as far as I am aware, this idea was not spoken commonly about until 2016, when the C-terminal domain (CTD) of the GTPase assembly factor Nog1 was observed to occupy the NPET, stretching almost to the PTC and interacting with the tunnel domain (TD) of L4 (**Figure 1.3a**) (Wu et al., 2016).

At the time of this observation, very little was known about Nog1. Depletion of Nog1 was known to cause an accumulation of the 27SB pre-rRNA precursor, and *nog1* mutations were shown to exhibit genetic interactions with *rlp24* and *tif6* mutations (Talkish et al., 2012). Earlier experiments to truncate the C-terminus were also shown to have no effect on cell viability (Fuentes et al., 2007). However, this newer cryo-EM observation of the Nog1 C-terminus in the NPET called these results into question and opened up a whole new set of questions. Among these questions was one concerning the significance of the interaction of the Nog1 C-terminal extension with the NPET, especially the contacts made between the Nog1 CTD and the tunnel domain (TD) of L4.

Previously, L4 had received more attention than most ribosomal proteins. L4 has 3 main domains, a globular domain that rests on the outside of the large subunit, a remarkably long C-terminal tail that snakes around on the surface of the large subunit, and an internal loop that burrows into the large subunit to line the NPET (**Figure 1.3a**). Depletion of L4 revealed an accumulation of $27SA_2$ pre-rRNA, indicating an early block in 60S assembly (Gamalinda and Woolford, 2014b). Truncation of the long C-terminal domain of L4 phenocopied a depletion. It was later figured out that the chaperone Acl4 binds the C-terminal domain of L4 to help recruit and load L4 onto the pre-60S subunit (Pillet et al., 2015; Stelter et al., 2015). Interestingly, a second molecule of Acl4 also binds the internal loop of L4 (Pillet et al., 2015). Most importantly, deletion of the TD of L4 did not phenocopy a depletion phenotype and instead appeared to cause a later block in 60S assembly (Gamalinda and Woolford, 2014b; Stelter et al., 2015). However, this later block was never studied in detail.

In order to investigate how NPET assembly fits into the hierarchy of 60S ribosomal subunit assembly and to answer questions concerning the Nog1 CTD and L4 TD, I studied mutants of these two proteins, including the L4 TD deletion initially studied by Michael Gamalinda (Gamalinda and Woolford, 2014b). The data presented in this chapter demonstrate that the Nog1 CTD and L4 TD work together to build the NPET, highlight the importance of rRNA rearrangements in ribosome assembly, and add credence to the idea that functional centers communicate with each other during ribosome assembly.

Results

2.1.1 The L4 tunnel domain is necessary for late nucleoplasmic stages of 60S ribosomal subunit assembly

Previously, the tunnel domain (TD) of L4 was shown to be necessary for 60S subunit assembly (Gamalinda and Woolford, 2014b). However, its precise function during ribosome biogenesis remains unclear. Because the bi-lobal TD of L4 (amino acids 63–87) forms constriction sites in the NPET and more recently has been shown to interact with a number of tunnel-probing ribosome assembly factors (Greber et al., 2016; Kater et al., 2017; Ma et al., 2017; Sanghai et al., 2018; Wu et al., 2016), we wanted to investigate its specific role in 60S ribosomal subunit assembly in greater detail. To this end, I have characterized multiple strains expressing different mutations or full deletions of the L4 TD. I focused on the effects of the *rpl4Δ63–87* mutation because it removes both constriction sites from the NPET and, I reasoned, would give us the best chance at seeing significant results in larger-scale experiments (**Figures 2.1a** and **2.1b**). Initial experiments involving the shorter deletion, *rpl4Δ63-75*, showed behavior identical or similar to the *rpl4Δ63-87* mutant (**Figures 2.2a** and **2.2b**). Therefore, in hindsight, any lethal mutation of this region of L4 may have yielded identical results. To assay effects of the *rpl4Δ63–87* mutation, we expressed the mutant L4 protein from a plasmid in a strain conditional for expression of endogenous wild-type L4 (*GAL-RPL4*). This strain grows at wild-type rates on galactose-medium but fails to grow on glucose-medium where only the mutant protein is expressed.

In order to determine which stages of the 60S subunit assembly pathway are affected in the *rpl4Δ63–87* mutant, we assayed pre-rRNA processing using primer extension and northern blotting. Compared to the wild-type strain, the *rpl4Δ63–87* mutant accumulated both 27SB and 7S pre-rRNAs, which normally undergo processing during late nucleolar and nucleoplasmic stages of 60S assembly (**Figure 2.3a**). To confirm that these middle steps of 60S subunit assembly are affected in the *rpl4Δ63–87* mutant, we assayed localization of pre-60S subunits using L25-eGFP (uL23), a reporter of both mature and pre-60S subunits, and Nop1-mRFP, a nucleolar marker. Relative to the wild-type strain, we observed accumulation of pre-60S subunits in the nucleolus and nucleoplasm in the *rpl4Δ63–87* and *rpl4Δ63-75* mutants (**Figure 2.3b**). These results demonstrate that the L4 TD is necessary for late nucleolar and nucleoplasmic stages of 60S subunit assembly prior to pre-60S export from the nucleoplasm.

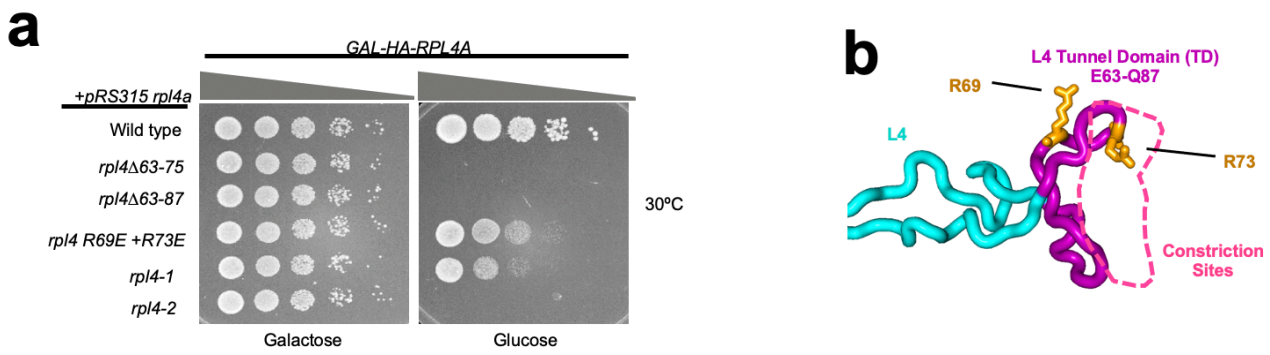

Figure 0.1. Mutations made to the tunnel domain of L4 are lethal in yeast. **(a)** Deletion of the L4 tunnel domain (aa 63–87) is lethal. Each strain contains *GAL-RPL4A* that can be turned off by shifting cells from galactose to glucose-medium, and a plasmid that is constitutively expressing an *rpl4* mutant allele. The *rpl4-1* and *rpl4-2* mutations are alanine scans of residues 63–68 and 69–74, respectively. Serial dilutions (1:10 to 1:10,000) of cultures were pipetted onto selective medium containing either galactose or glucose, incubated at 30°C, and imaged after 3 days. **(b)** Diagram of the internal loop of L4 (cyan), including the TD (purple) that extends into the NPET to help create the constriction sites (dotted pink line). Indicated arginine residues (orange) were mutated to glutamate. The TD forms the constriction sites in the NPET (pink dotted line).

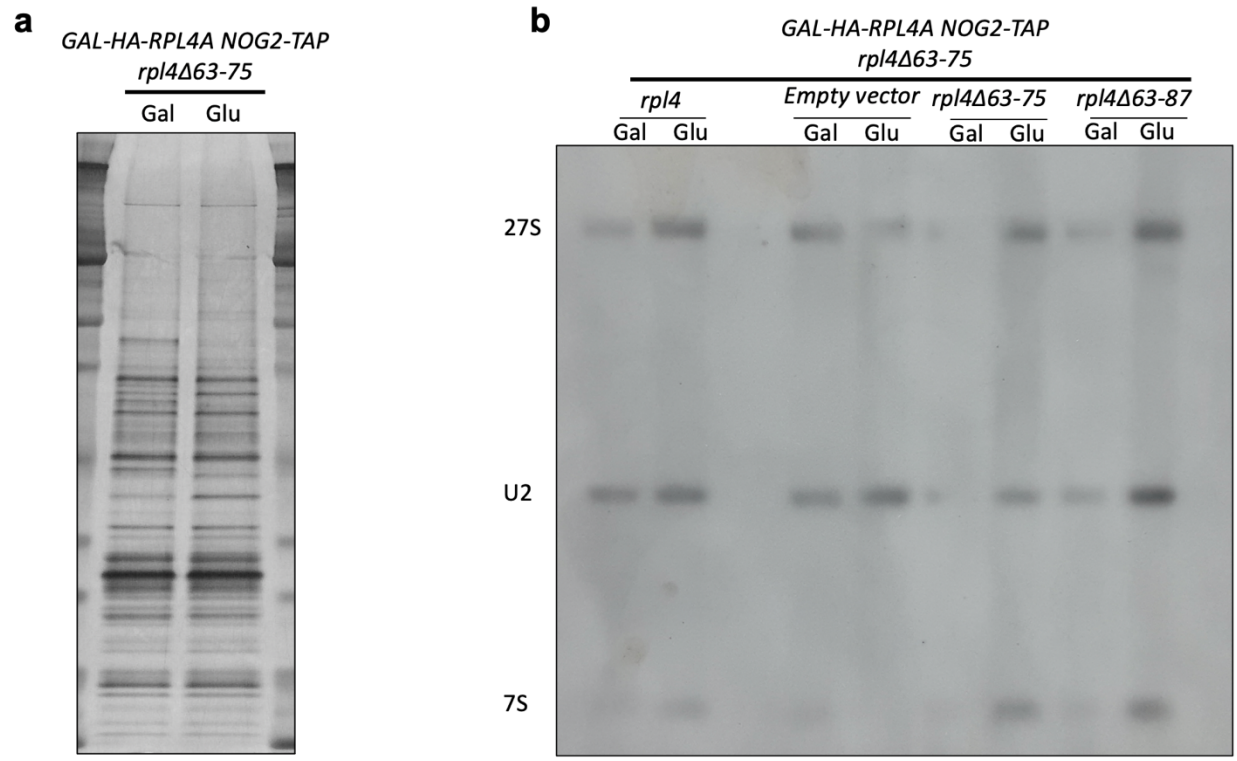

Figure 0.2. The *rpl4*Δ*63-75* mutant displays defects similar to those observed in the *rpl4*Δ*63-87* mutant.

(a) Nog2-TAP purification of pre-60S ribosomal subunit from the *rpl4*Δ*63-75* mutant. This profile shows changes in bands similar but not identical to those observed in the *rpl4*Δ*63-87* mutant. Notably, the Rea1 band (heaviest on the gel) does not seem to change as dramatically. **(b)** Northern blot of whole cell RNA extracted from various *rpl4* mutants. Probes are targeted towards 27S and 7S pre-rRNA intermediates with U2 acting as a loading control.

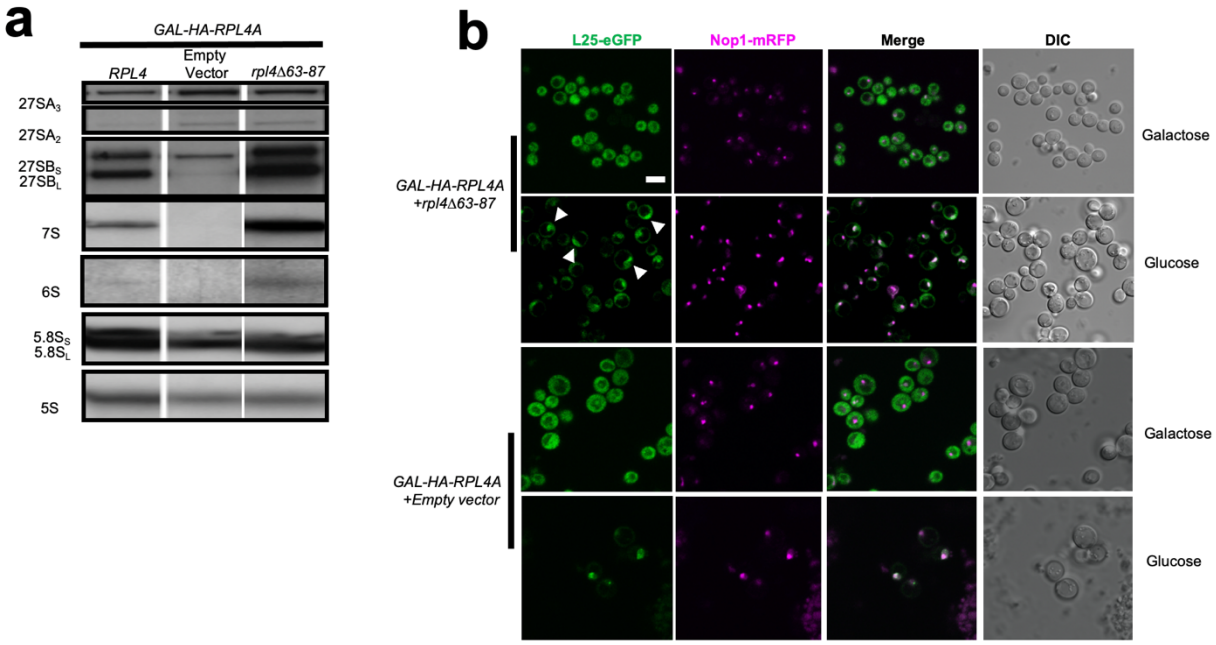

Figure 0.3. **Mutant *rpl4Δ63-87* pre-60S subunits fail nuclear export.**

(a) 27S and 7S pre-rRNAs accumulate in the *rpl4Δ63-87* mutant. Cells were shifted from galactose to glucose media for 17 h. before extracting whole cell RNA. Steady-state levels of pre-rRNAs from each strain were then assayed by primer extension and gel electrophoresis. **(b)** Pre-60S subunits accumulate in the nucleoplasm of the *rpl4Δ63-87* mutant, after being shifted from galactose to glucose media for 17 h. to deplete wild-\type L4. In contrast, in the absence of the entire L4 protein (empty vector), pre-ribosomes accumulate in the nucleolus. L25-eGFP (green) tracks pre-60S particles and Nop1-mRFP (magenta) marks the nucleolus. Scale bar: 5μm.

2.1.2 The tunnel domain of L4 is necessary to stabilize the 3-way rRNA junction of H75, H76, and H79

Because our assays thus far suggest a defect during late nucleolar/nucleoplasmic stages of 60S assembly, we used the late nucleolar/nucleoplasmic acting AF Nog2 as bait to affinity-purify particles from this stage of assembly. We performed cryo-EM on these Nog2-associated pre-60S particles, which enabled observation of both small and dramatic changes in rRNA and protein conformation that would otherwise be undetectable by other methods. Previously, cryo-EM structures of wild-type Nog2-associated particles revealed three distinct consecutive assembly intermediates during middle stages of 60S subunit assembly: Nog2 states 1, 2, and 3. Nog2 state 1 particles contain a pre-rotated 5S RNP, Nog2 state 2 contains a rotated 5S RNP along with AFs Sda1, the Rix1 complex, and Rea1 (Barrio-Garcia et al., 2015), while Nog2 state 3 contains a rotated, near mature 5S RNP and has released Sda1, the Rix1 subcomplex, Rea1, and Rsa4. Therefore, using Nog2 as bait enabled us to assess the progress of 60S subunit assembly during late nucleolar and nucleoplasmic stages.

Through cryo-EM 3D classification, we obtained seven states for the *rpl4Δ63–87* mutant particles, which we refer to as classes R1-R7 (**Figure 2.4**). As expected, density for the deleted TD of L4 could not be observed in any of these classes. Classes R3 and R4 comprise a small fraction of the particles (10%), and represent intermediates inhibited during early steps of 60S subunit maturation (**Figure 2.5a** and **2.5b**). The R1 and R2 particles (27% and 12%, respectively) closely resemble Nog2 state 1 particles,

containing a pre-rotated 5S RNP, and thus have progressed beyond the stages represented by the R3 and R4 particles. The R7 class (10%) is R1-like but lacks densities for nearly the entire domains III and IV of 25S rRNA and appears to represent R1 particles undergoing turnover (**Figure 2.5e**). Class R6 particles contain a rotated 5S RNP and resemble Nog2 state 3 (Arx1 particles) (**Figure 2.5d**), but also lack densities for several rRNA helices underneath the L1 stalk. Thus, R6 particles appear to be blocked later than class R1, after rotation of the 5S RNP. Finally, class R5 resembles R6 but, lacks densities for nearly the entire domains III, IV, and V of 25S rRNA and therefore may represent R6 particles undergoing turnover (**Figure 2.5c**). We first focused on the pre-ribosomes in classes R1 and R2 because they are the most abundant and stable mutant particles. The structures of these R1 and R2 particles were solved at a resolution of 3.2 and 3.3 Å (**Figure 2.4b**). In classes R1 and R2, no density could be observed for the NPET-occupying RP L39, the Nog1 CTD, or AF Arx1 that binds to the NPET exit platform (**Figure 2.6**). This indicates that lack of the L4 TD causes significant disruption in the composition of the immature NPET.

Several other protein components were also found to be missing or flexible in both classes R1 and R2 (**Figure 2.6b**). We could not observe densities for Bud20, Nug1, and Cgr1. While Cgr1 is known to be necessary for 5S RNP rotation (Thoms et al., 2018), it is not always detected in relevant pre-60S particles, even in wild-type Nog2 particles17. This suggests that Cgr1 may be loosely bound to pre-60S subunits and may explain why it cannot be observed in *rpl4Δ63–87.* Alternatively, this could be a real defect, possibly due to a slight expansion of the rRNA in the area surrounding the Cgr1 binding site (Sebastian Klinge, personal communication). However, if this were true, it

would cast doubt on previous findings that Cgr1 is necessary for 5S RNP rotation (Thoms et al., 2018).

We next looked at effects of the *rpl4Δ63–87* mutation on the structure of pre-rRNA in Nog2 particles. Although class R2 exhibits wild-type rRNA conformations, significant shifts in rRNA helices 68–69 and 74–79 could be seen in class R1 (**Figure 2.7**). Further analysis of the atomic model of class R1 revealed how a misassembled NPET could cause these rRNA conformational changes (**Figure 2.8a**). These aberrant shifts begin with a loss of the interaction between the TD of L4, the Nog1 CTD, and the linker between rRNA helices 73 and 74 (**Figure 2.8b-d**).

Recent cryo-EM structures further suggest the importance of this interaction (Kater et al., 2020). H74 is displaced ~4 Å relative to the wild-type conformation, indicating that this portion the NPET is improperly assembled (**Figure 2.8c**). The conformational change of H74 affects the adjacent H75, which can be seen shifted up to ~33 Å from its native position in Nog2 state 1 (**Figure 2.8c**). In this aberrant position, H75 clashes with H68 and displaces it up to ~62 Å toward the 5S rRNA (**Figure 2.8d**). H68 is the binding site for AF Sda1, which is important for rotation of the 5S RNP in Nog2 particles, and importantly, also acts as an intersubunit bridge in mature wild-type ribosomes. Once structured in Nog2 state 1, this helix remains stably docked throughout middle and later stages of 60S subunit assembly (Greber et al., 2016; Jenner et al., 2012; Ma et al., 2017; Wu et al., 2016; Zhou et al., 2018). Therefore, deviations from this stable position of H68, as seen in class R1, likely have negative consequences as a result of improper NPET construction during the assembly of 60S subunits.

Consistent with the displaced H74-75, the 3-way junction of rRNA helices 75, 76, and 79 is affected in class R1. Specifically, the L1 stalk (H76 and L1) adopts an unusual,

deflected conformation not observed in any previously characterized wild-type particles (**Figure 2.9**) and H79 is unstructured. As a result, the internal loop of L15 (uL15), which interacts with H75 in Nog2 state 1, cannot be visualized. Likewise, the N- terminus of L8 (eL8), which interacts with the 3-way junction of H75, H76, and H79 and was previously shown to be necessary for middle stages of 60S subunit assembly (Tutuncuoglu et al., 2016), is also flexible (**Figure 2.10**). These observations further characterize the perturbance of this 3-way junction as a result of improper NPET construction.

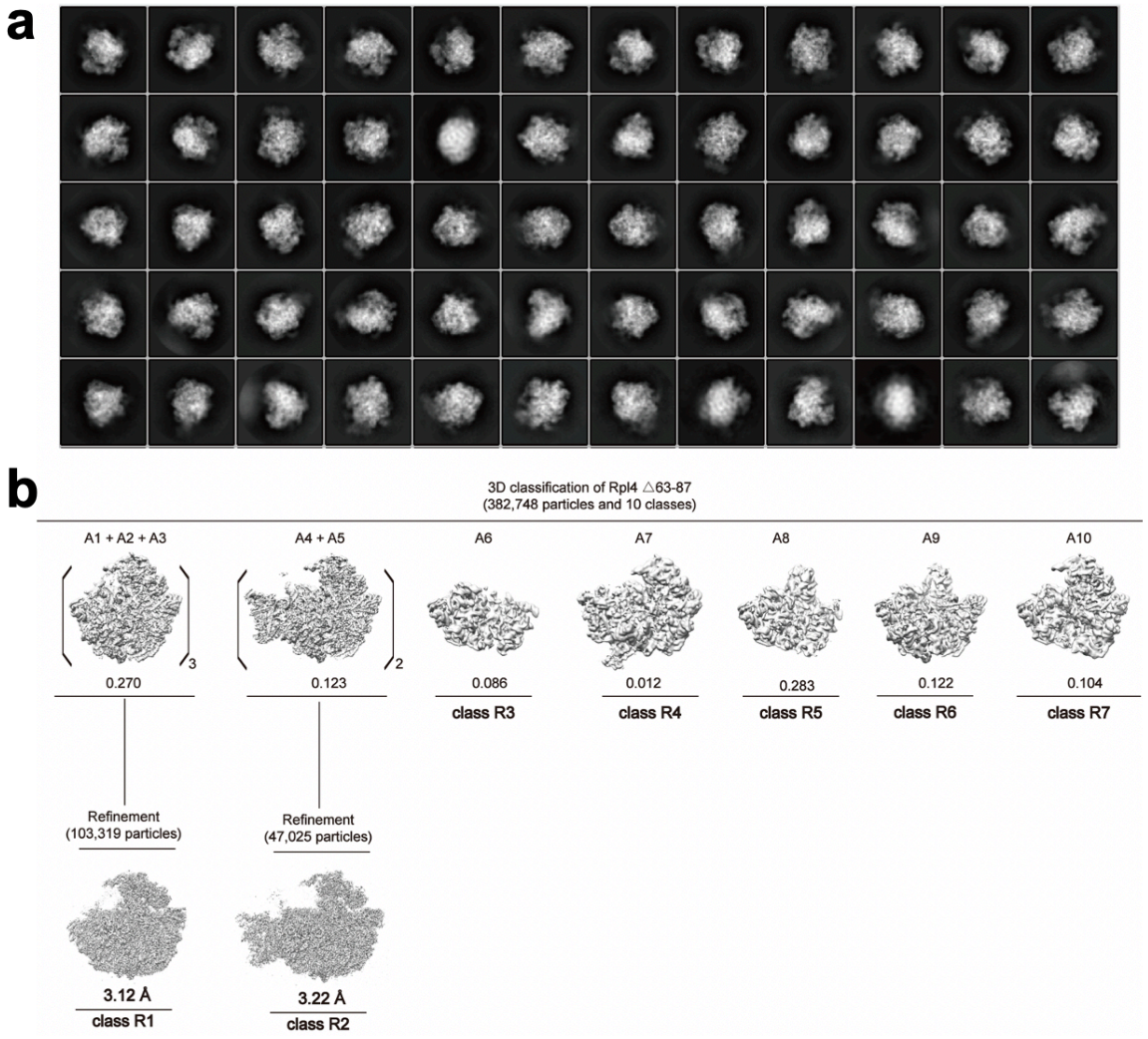

Figure 0.4. Cryo-EM data processing of *rpl4△63-87* Nog2 particles.

(a) Representative 2D class averages of *rpl4△63-87* mutant Nog2 particles. **(b)** Flow chart for 3D classification.

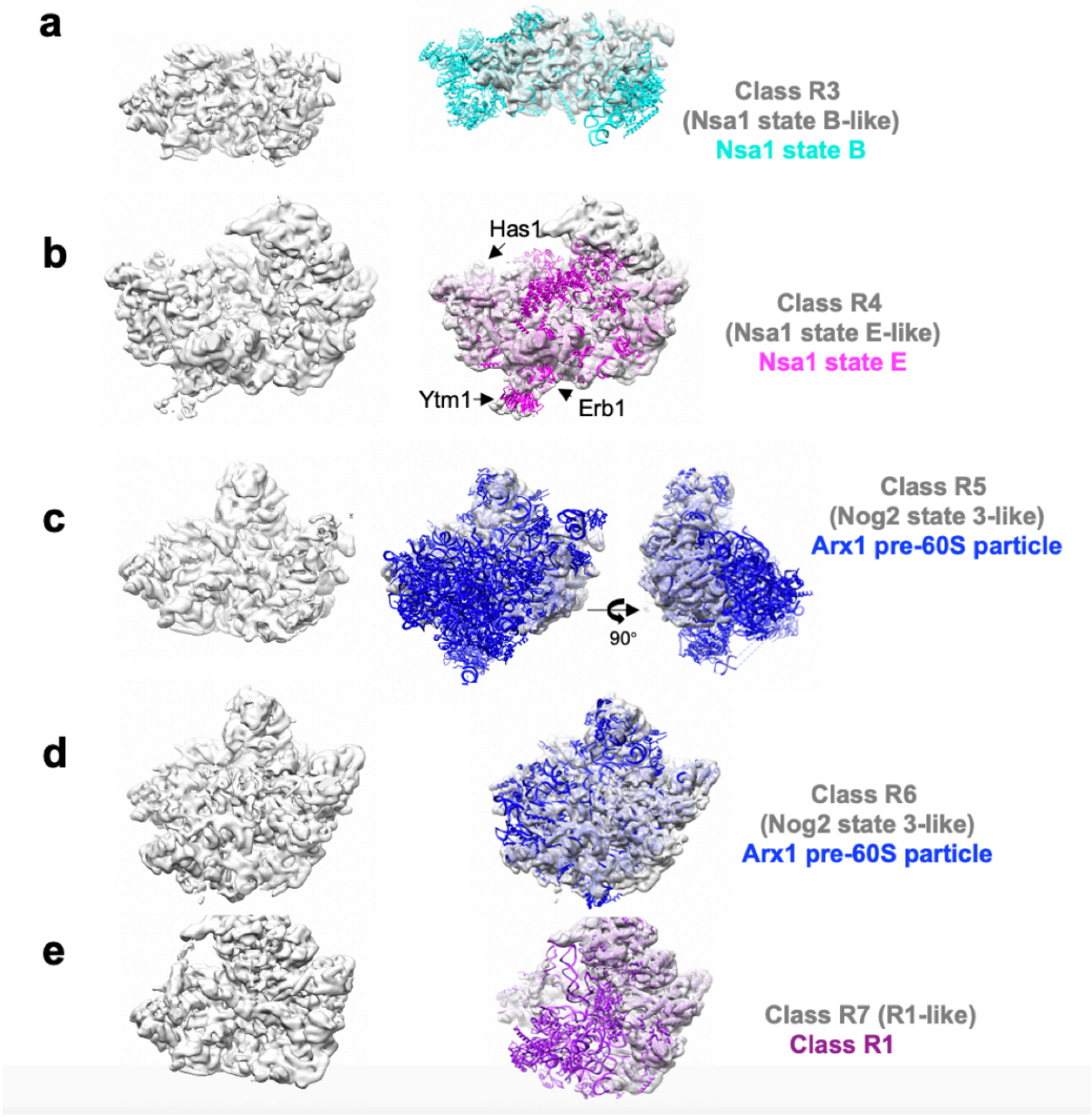

Figure 0.5. **Nog2 particles purified from the *rpl4Δ63-87* mutant**.

(a) Cryo-EM densities of class R3 (gray) fitted with the atomic model of the Nsa1 state B particle (cyan) (PDB: 6EM4). **(b)** Densities of class R4 (gray) fitted with the atomic model

of Nsa1 state E (purple) (PDB: 6ELZ). **(c and d)** Densities of classes R5 and R6 (gray) fitted with the atomic model of the Arx1 particle (blue) (PDB: 4V7F). **(e)** Densities of class R7 (gray) fitted with the atomic model of class R1 state (purple).

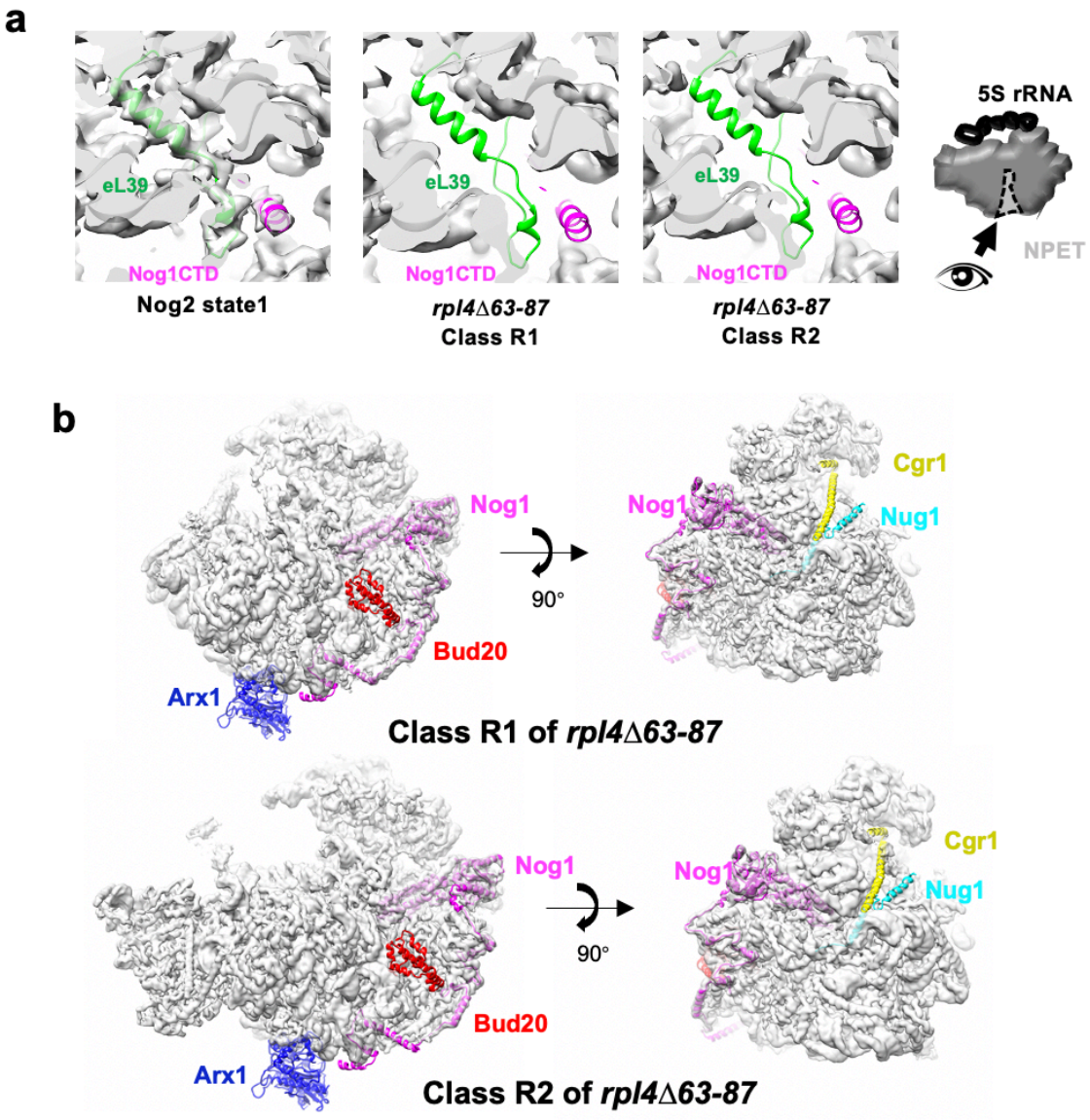

Figure 0.6. Cryo-EM of *rpl4Δ63-87* mutant particles reveals a misassembled NPET.

(a) Close up view of the exit of the NPET in wild-type Nog2 state 1 and *rpl4Δ63–87* classes R1 and R2. Gray densities are not present in classes R1 and R2 in the spaces where eL39 and the Nog1 CTD should be. Thus, the exposed cartoon model indicates missing components. **(b)** View of rpl4Δ63–87 classes R1 and R2 from the subunit

interface (left) and solvent side (right). Densities are fitted to the atomic model of wild-type Nog2 state 1 (PDB: 3jct). Exposed cartoon models of Arx1 (blue), the Nog1 CTD (magenta), Bud20 (red), Cgr1 (yellow), and Nug1 (cyan) represent missing densities for each respective protein.

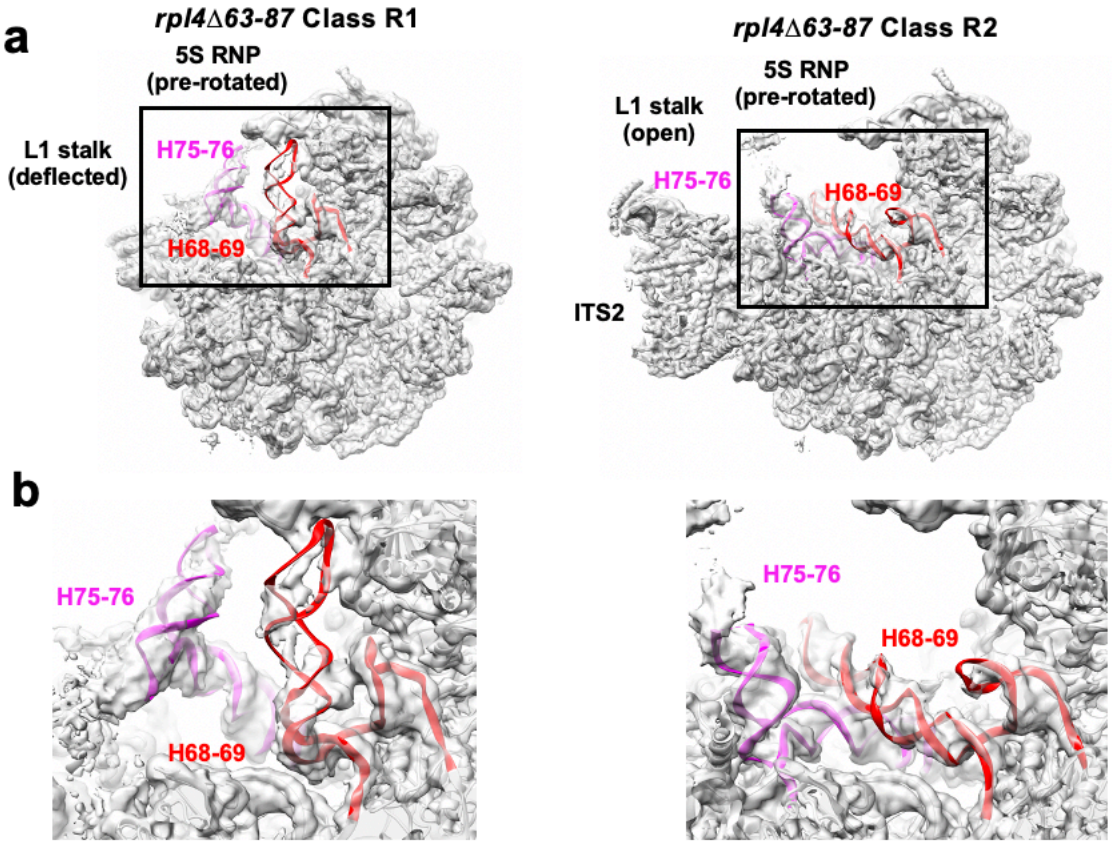

Figure 0.7. Pre-rRNA conformational changes observed in *rpl4Δ63-87* mutant class R1.

(a) Two major density maps (R1 and R2 particles, shown in light gray) obtained from Nog2-associated *rpl4Δ63–87* particles are overlaid with their respective atomic models. **(b)** Enlarged view of the conformational changes in of rRNA helices from the two major classes of the *rpl4Δ63–87* mutant. Compared with wild-type Nog2-particles (state 1), H75-76 (magenta) and H68-69 (red) have undergone dramatic conformational changes in class R1 but not in class R2.

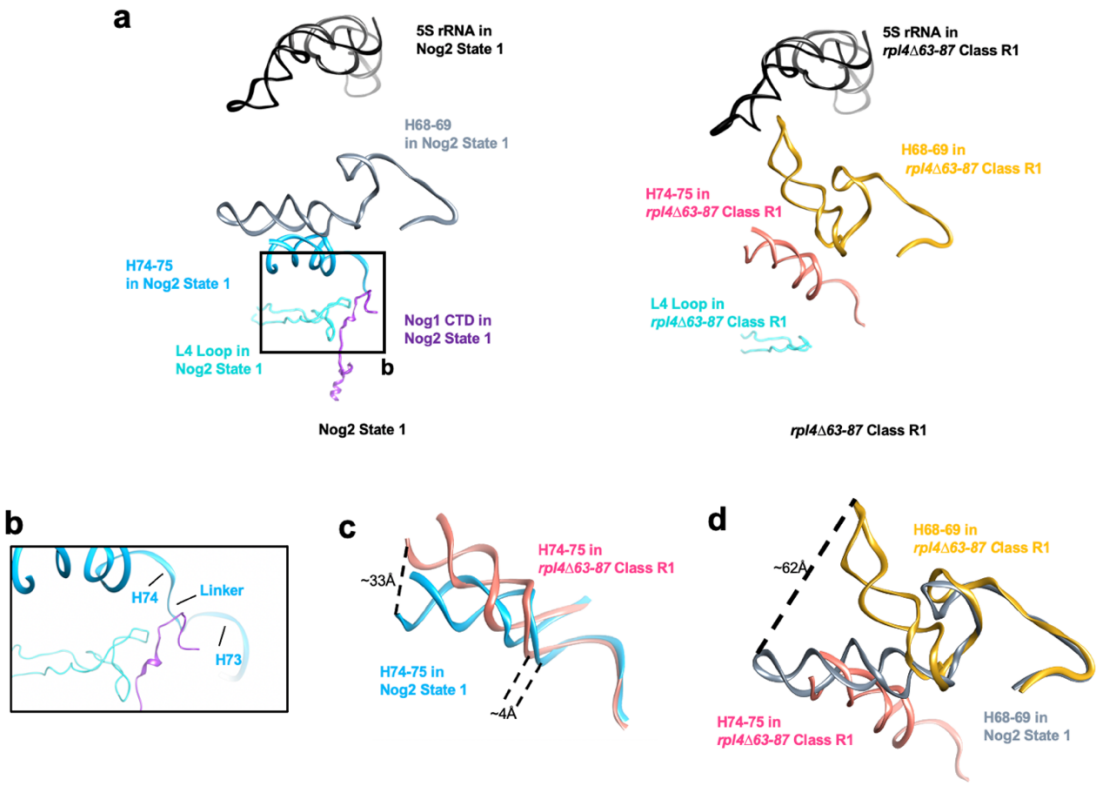

Figure 0.8. rRNA helix 74 functions to stabilize helices 68 and 75.

(a) rRNA helices from the atomic model of wild-type Nog2 state 1 particles are compared with those in the atomic model of the *rpl4Δ63–87* mutant class R1. Positions of relevant rRNA helices in relation to L4 and Nog1 in the NPET in RPL4 wild-type (left) and *rpl4Δ63–87* mutant (right) Nog2 particles. Helices 74–75 (light blue for wild-type and hot pink for mutant) extend into the NPET. H74 is located in close proximity to the L4 TD (cyan) and the CTD of Nog1 (dark purple). Helices 74-75 are located below H68-69 (gray for wild-type and gold for mutant). The 5S rRNA (black) is shown to provide a frame of reference. **(b)** Inset showing the interaction of the TD of L4, the Nog1 CTD, and the rRNA linker between H73 and H74. **(c)** H74-75 from *rpl4Δ63–87* mutant particles (hot pink) are shifted relative to those in wild-type Nog2 state 1 particles (light blue). H74 is displaced up to ~4 Å while H75 is shifted up to ~33 Å. **(d)** H75 in *rpl4Δ63–87* mutant

particles is shifted to an aberrant position (hot pink) that clashes with the native position of H68 (gray). This displaces H68 in *rpl4Δ63–87* mutant particles (gold), causing it to shift up to ~62 Å.

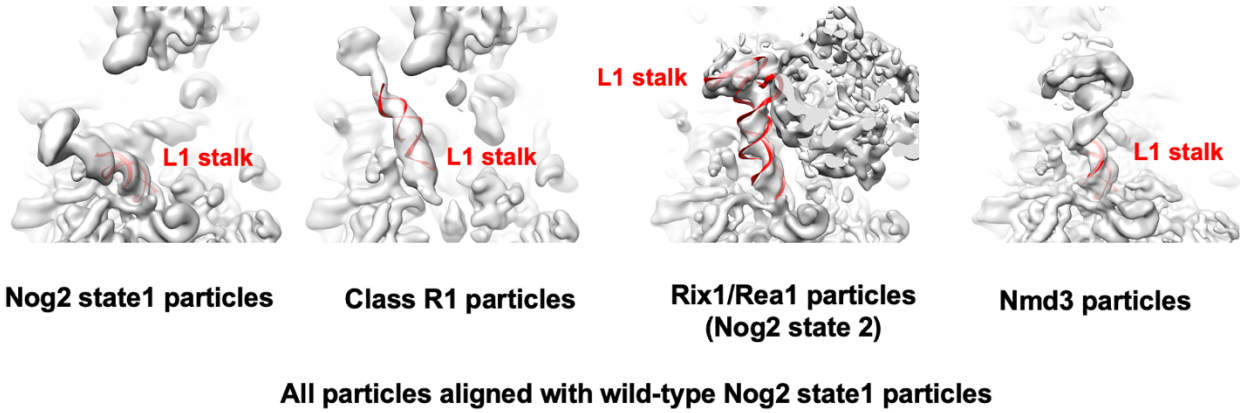

Figure 0.9. Class R1 exhibits a deflected L1 stalk.

Cryo-EM density maps of four assembly intermediates, wild-type Nog2 state1, mutant class R1, wild-type Rix1/Rea1 state (Nog2 state 2), and the wild-type Nmd3 state are displayed in transparent surface representation, superimposed with their own atomic model. rRNA for the L1 stalk is shown in red.

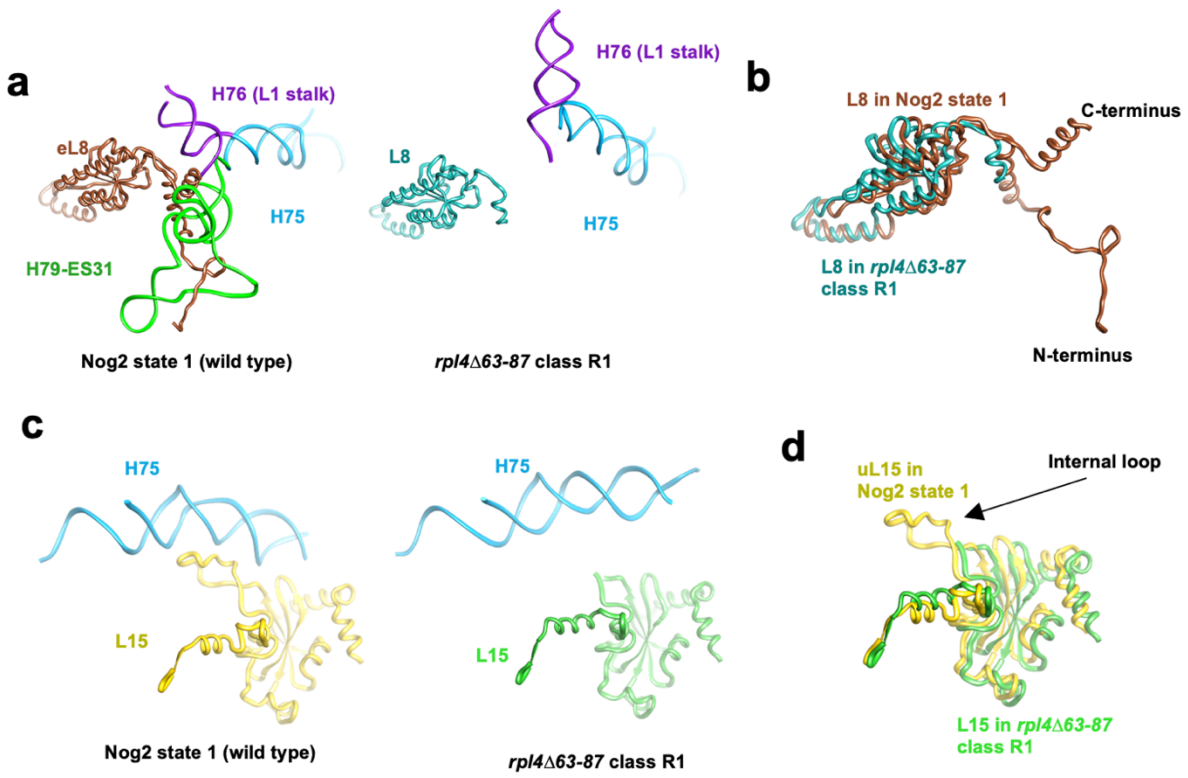

Figure 0.10. Defects in H75 are communicated to L8 and L15.

(a) RP L8 in wild-type Nog2 state 1 particles (left) shown in relation to the 3-way junction of H75 (blue), H76 (light purple), and H79 (green). On the right, the same components are shown in class R1 of the *rpl4Δ63-87* mutant particles. **(b)** L8 from wild-type Nog2 state 1 particles (brown) overlaid with L8 from class R1 (dark teal). In class R1, both the N- and C- termini are flexible. **(c)** RP L15 (yellow) in wild-type Nog2 state 1 particles (left) shown in relation to H75 (blue). On the right, the same components are shown in class R1 of the *rpl4Δ63-87* mutant particles. **(d)** L15 from wild-type state 1 particles (yellow) overlaid with L15 from *rpl4Δ63-87* class R1 particles (light green). In class R1, the internal loop of L15 is flexible.

2.1.3 A misassembled NPET can block Sda1 binding to pre-60S ribosomal subunits and subsequent 5S RNP rotation

To help clarify the consequences of the aberrant rRNA conformations observed in *rpl4Δ63–87* mutant pre-60S subunits, we utilized SDS-PAGE, western blotting, and a semi-quantitative form of label mass spectrometry called iTRAQ to analyze the protein composition of these particles. Importantly, levels of L4 do not change in the *rpl4Δ63–87* mutant pre-ribosomes compared to wild-type, indicating that the mutant L4 protein is stable and able to efficiently assemble into pre-60S subunits. However, we did observe a number of changes in amounts of other proteins in the mutant pre-ribosomes. Most striking was that levels of Sda1 decreased and levels of Rpf2 and Rrs1 increased (**Figure 2.11a** and **b**). In wild-type cells, the AFs Rpf2 and Rrs1, which are bound to the 5S RNP, are thought to exit from Nog2 particles before Sda1 binds to pre-60S subunits (Klinge and Woolford, 2019). Thus, Sda1 fails to associate with a significant fraction of pre-60S subunits in this mutant, and Rpf2 and Rrs1 fail to exit from pre- ribosomes. Furthermore, amounts of downstream AFs Rea1, and the Rix1 complex (Rix1, Ipi1, and Ipi3), which depend on Sda1 for recruitment onto pre-60S subunits and are required to stabilize 5S RNP in its rotated state, also are decreased relative to wild-type (**Figure 2.11b**). Consistent with a failure of Rea1 to enter assembling pre-60S subunits, levels of Rsa4, which is removed by Rea1, are increased.

All of these data strongly suggest that the NPET not only communicates with the PTC, but also with the 5S RNP. Hints of this were evident in the literature for decades (Khaitovich et al., 1999), but this is the first sign that this communication may happen during ribosome assembly. Furthermore, this particle likely represents the primary block

in ribosome assembly present in the *rpl4Δ63-87*. Despite the presence of particles exhibiting a rotated 5S RNP in this dataset (**Figure 2.11c**), class R1 is the most abundant stable particle. Combined with our bulk biochemical assays pointing to a block in 60S ribosomal subunit assembly *before* nuclear export, these facts, in my view, make a strong case for NPET assembly and 5S RNP rotation being coupled.

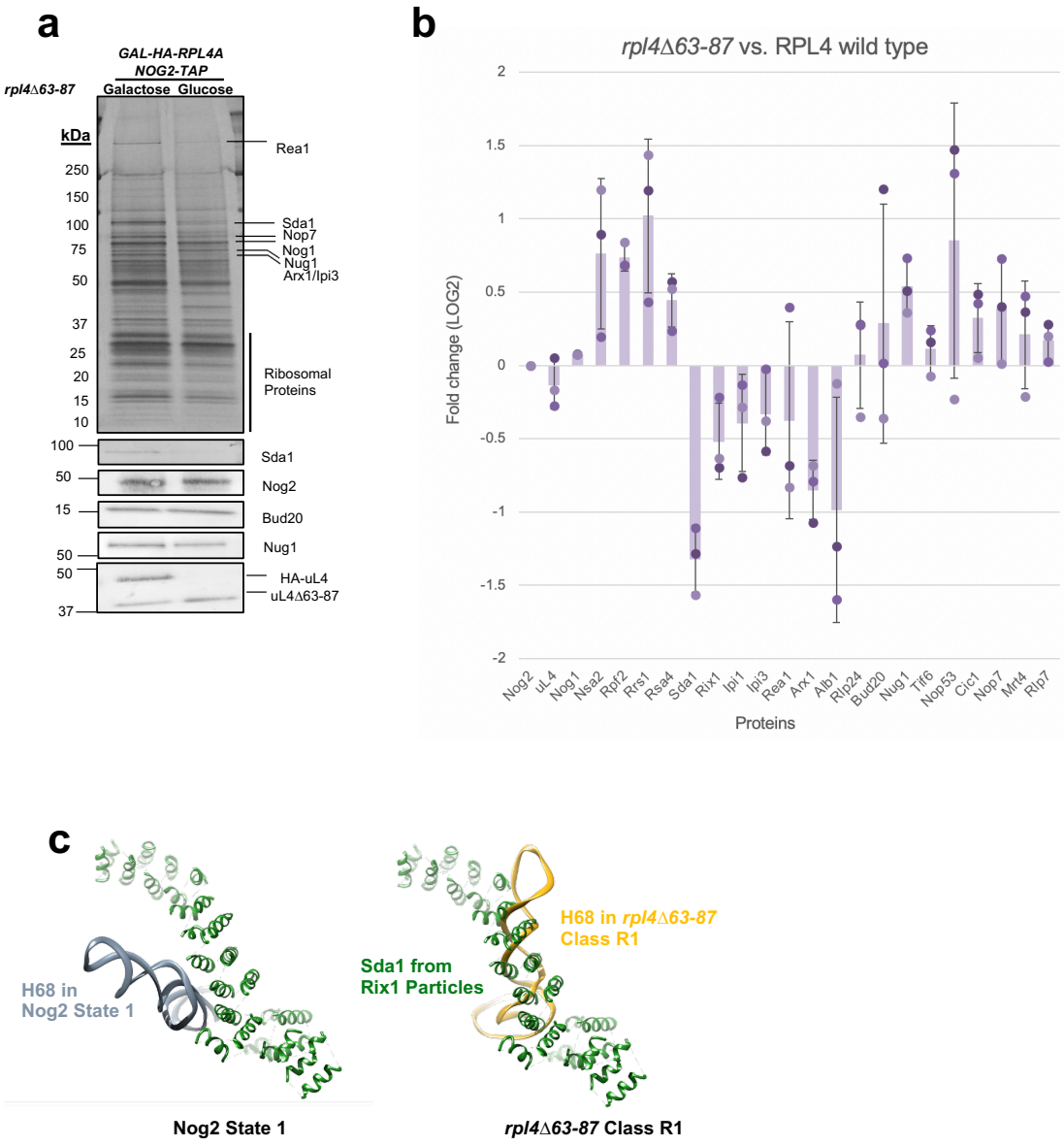

Figure 0.11. Deviations in rRNA structure in *rpl4Δ63–87* mutant particles result in H68 clashing with the binding site of Sda1.

(a) SDS-PAGE gels followed by silver staining or western blotting show proteins in Nog2-associated particles purified from mutant *rpl4Δ63–87* cells. Labeled bands were

identified using mass spectrometry. **(b)** Samples prepared as in panel a were scaled up and subjected to semi-quantitative iTRAQ mass spectrometry to assay changes in relative amounts of pre-60S subunit proteins. Proteins were labeled with iTRAQ reagents and compared to wild-type counterparts. Each bar represents a biological replicate. All protein levels are normalized to the bait protein, Nog2. Ratios are represented on a log2 scale. Error bars represent standard deviation (n = 3). **(c)** The AF Sda1 (dark green) from Rix1 particles superimposed over wild-type Nog2 state 1 particles (left) and *rpl4Δ63–87* mutant particles (right). H68 (gray for wild-type and gold for mutant) in *rpl4Δ63–87* mutant particles clashes with almost the full length of observable Sda1.

2.1.4 The C-terminal tail of Nog1 is necessary for efficient assembly of 60S ribosomal subunits

Since the Nog1 CTD is in close contact with the TD of L4 in wild-type cells and fails to enter the NPET in *rpl4Δ63–87* mutant particles, we wanted to investigate whether deleting the Nog1 CTD results in similar or different 60S subunit assembly defects compared to those observed in the *rpl4Δ63–87* mutant. Furthermore, the presence of the Nog1 CTD in the NPET suggests many possible functions. Initially, we made a series of truncations of the Nog1 C-terminus on a *NOG1*-containing *pRS315* plasmid and transformed them into a *GAL-NOG1* strain, as was done for the *rpl4* mutants described before. Surprisingly, upon growing these strains on glucose where only the *nog1* mutant allele is present, no significant growth defect was detected at any growth temperature (**Figure 2.12**). This was surprising, but not completely unexpected given the previous experiments done long before the structure of Nog1 was known (Fuentes et al., 2007).

As an orthogonal approach to deleting Nog1 sequences inserted into the tunnel, we constructed a strain expressing Nog1 fused to GFP at its C-terminus (NOG1-GFP). Because an immature NPET is already formed before the Nog1 CTD enters the tunnel (**Figure 1.3a**), this bulky GFP tag must prevent insertion of the Nog1 CTD into the tunnel. Grown on rich media, this GFP-tagged strain exhibited an extreme cold-sensitive growth defect (**Figure 2.13**). Intrigued by this, we decided to grow our plasmid-borne *nog1* strains on rich media and observed a cold-sensitive growth defect similar to the Nog1-GFP tagged strain (**Figure 2.14**). This is an example of a mutation that does not readily manifest when the cells are grown on minimal media, and it almost mislead us

completely. Usually, this kind of discrepancy reflects a tendency for mutant alleles expressed on a plasmid to recombine with the wild-type allele in the genome and undergo a reversion. However, because growth defects of these plasmid-borne mutants were readily apparent when grown on rich media (**Figure 2.14**), there are two likely explanations for this discrepancy: **1)** Minimal media may slow down the usually rapid growth of wild-type cells in a way that makes the growth of the mutants seem normal relative to the wild-type cells **2)** There could be multiple plasmids in a mutant cell, which could change the copy number of the mutant gene and compensate for the mild defect it may cause. No matter the case, we realized that we needed a better way to study these *nog1* mutations. Future graduate students should be aware that non-lethal mutants may not be easy to study in a system that requires minimal media.

In light of these results, we generated a series of genomic mutations to sequentially truncate the CTD of Nog1 so that these mutations could be studied with fewer confounding factors (**Figure 2.13**). We also constructed the triple mutant *nog1Δ595–647 rei1Δ341-393 reh1Δ 380-432* (*nog1ΔC rei1ΔC reh1ΔC*) (also referred to as triple tail mutant) lacking the NPET-occupying sequences of Nog1, Rei1, and Reh1. This triple tail mutant was made in order to address the concern that the CTDs of Rei1 or Reh1 may dampen or rescue a defect caused by a Nog1 truncation. These strains exhibited the severe cold-sensitive growth defect observed before with plasmid-borne *nog1* strains grown on rich media (**Figure 2.14**). In contrast to these mutants, an analogous C-terminal truncation of Rei1 has been shown to have minimal effects on cell growth at all temperatures, while the complete absence of Reh1 has no obvious growth defect (see Discussion and Future Directions) (Greber et al., 2016; Parnell and Bass, 2009).

To examine whether this cold sensitivity reflects a defect in 60S subunit assembly, we used sucrose gradient fractionation to assay amounts of free ribosomal subunits, 80S monosomes, and polyribosomes in extracts prepared from each strain. In each case, levels of free 60S ribosomal subunits are decreased relative to 40S subunits, polyribosomes are decreased, and halfmer polyribosomes are present, indicating a defect in production of 60S subunits (**Figure 2.15**).

To determine which interval of 60S subunit assembly is perturbed in each mutant, we examined pre-rRNA processing. When cells were shifted to 16°C for 5 h, 27SB pre-rRNA accumulates in all mutant strains relative to the wild-type *NOG1* yeast strain (**Figure 2.16**). Attempts to assay levels of 7S pre-rRNA in these mutants yielded inconsistent results, likely indicating that there is no significant change (**Figure 2.16**). Together, these results indicate that the presence of the CTD of Nog1 in the NPET is important during late nucleolar and nucleoplasmic stages of 60S subunit assembly.

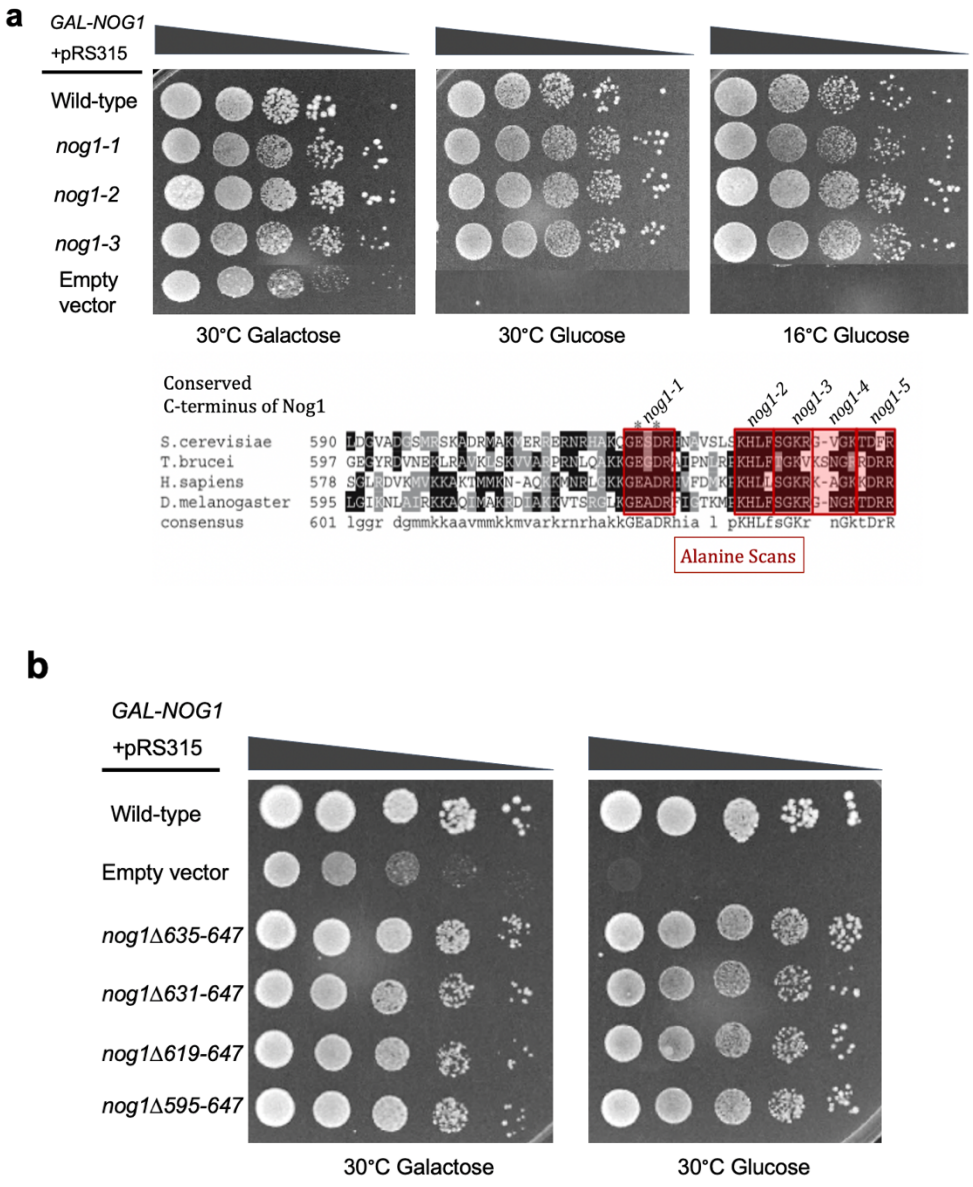

Figure 0.12. Plasmid-borne mutations of *nog1*.

(a) Growth assay of alanine scanning mutations of conserved motifs in the Nog1 C terminus. The *nog1-4* and *nog1-5* mutations were later shown to be incorrect mutations, so those spotting results are not shown. **(b)** Growth assay of truncations made to the Nog1 C-terminus. Each alanine scan or truncation mutation was expressed from a pRS315 plasmid.

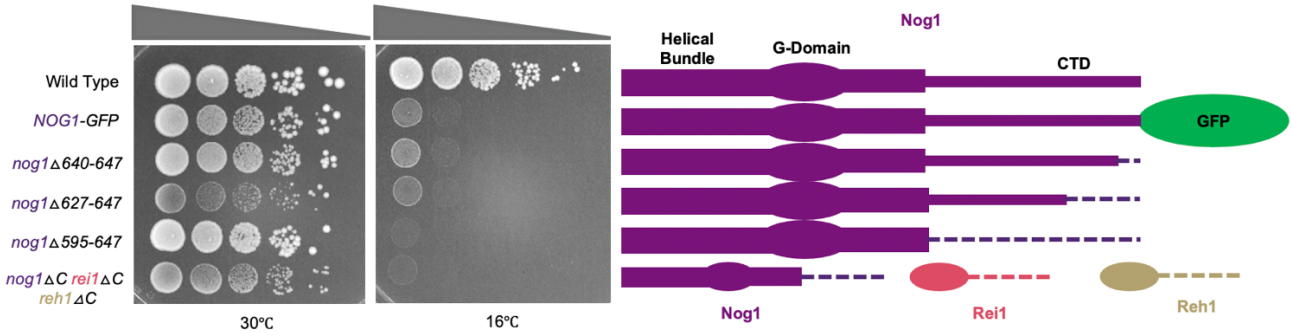

Figure 0.13. **Growth assay of genomic *nog1* truncation mutants**.

Serial dilutions (1:10 to 1:10,000) of NOG1 wild-type and nog1 mutant cultures were spotted onto solid medium containing glucose, and incubated at 30 °C or 16 °C, for 8 days. Each construct is depicted in cartoon form (right).

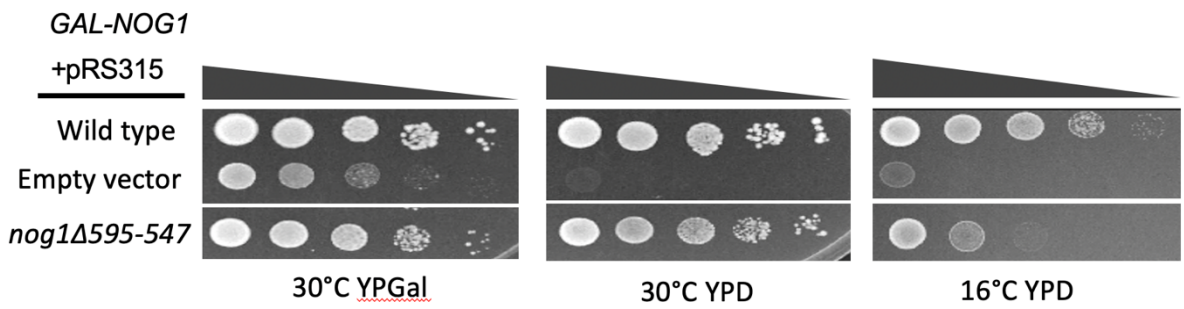

Figure 0.14. Growth assay of a plasmid-borne *nog1* truncation grown on rich media.

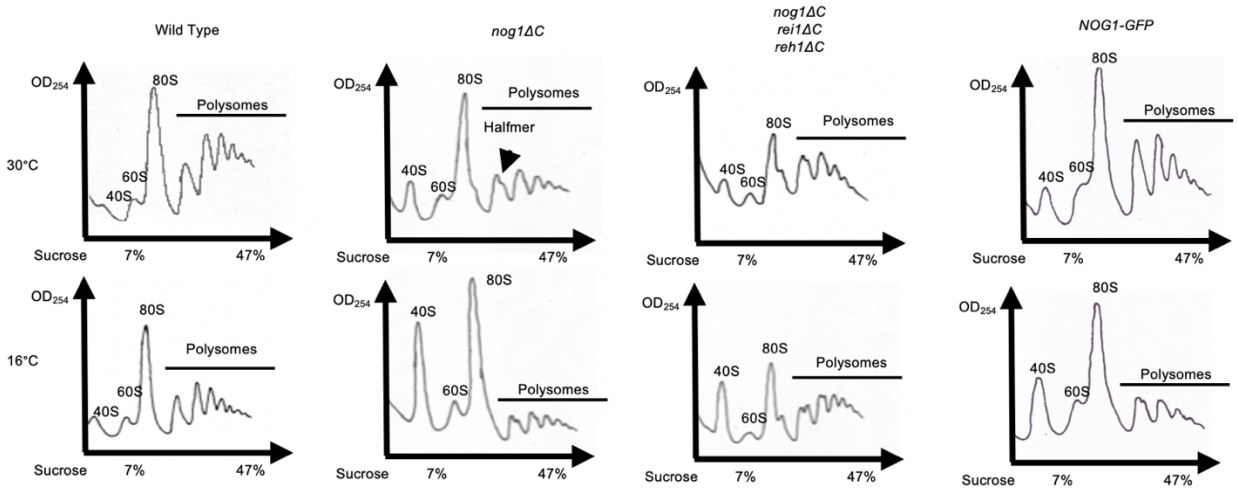

Figure 0.15. Sucrose gradient fractionation of *nog1* mutants.

Sucrose gradient fractionation of whole-cell lysate collected from *nog1* mutants grown at 30ºC or shifted to 16ºC for five hours.

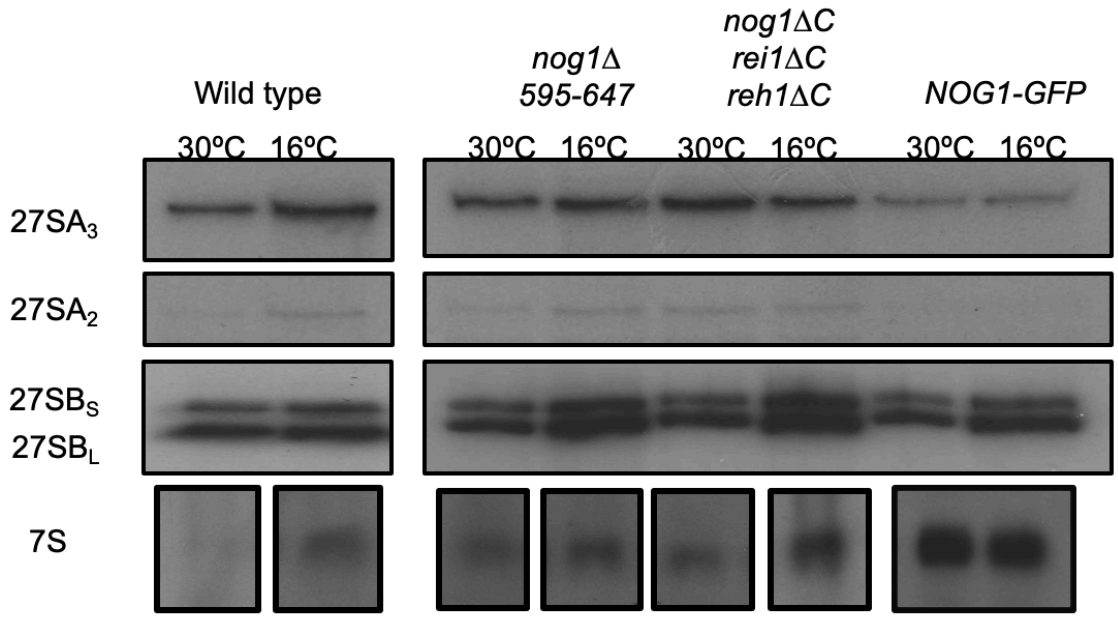

Figure 0.16. Pre-rRNA analysis in *nog1* mutants.

Primer extension and northern blot analysis of whole-cell RNA extracted from *nog1* mutants grown at 30ºC or shifted to 16ºC for five hours.

2.1.5 The C-terminal domain of Nog1 acts as a scaffold for the tunnel domain of L4

We performed cryo-EM of Nog2-containing particles affinity-purified from the *nog1ΔC rei1ΔC reh1ΔC* mutant, shifted to 16°C for 5 h. We focused on this triple mutant because it exhibited the most severe growth defect and, as mentioned before, we expected that the CTD's of Rei1 and Reh1 might partially rescue defects of a *nog1Δ595–647* mutant. We obtained structures of four stable intermediates at resolutions ranging from 3.0 to 4.3 Å, which we refer to as classes N1–N4 (**Figure 2.17**). The most striking observation from these structures is that the interior of the NPET in all four *nog1ΔC rei1ΔC reh1ΔC* particle classes lacks density for the TD of L4 (**Figure 2.18a**). In this case, the TD is present but is flexible enough for its conformation to be too heterogeneous and thus appears to be invisible in the cryo-EM reconstructions. This result indicates that the presence of the Nog1 CTD in the NPET is required to stabilize the TD of L4. In contrast to the *rpl4Δ63–87* mutant particles, L39 was present in classes N1–N4 (**Figure 2.18a**). This indicates that the CTD on Nog1 is not required to recruit L39 to pre-ribosomes.

Classes N1 and N2 closely resemble class R2 from the *rpl4Δ63–87* mutant, except that the ITS2 structure is absent in class N2 (**Figure 2.18b**). This latter observation is consistent with previous findings that removal of ITS2 can occur independently from other remodeling events such as 5S RNP rotation (Biedka et al., 2018; Sarkar et al., 2017). Therefore, in the triple tail mutant, removal of ITS2 occurs a fraction of the time.

Class N3 particles resemble class R1 from the *rpl4Δ63–87* mutant, including the aberrant rRNA rearrangements, deflected L1 stalk, and absence of Sda1 (**Figure 2.19**). However, while class R1 makes up about 27% of total particles obtained from the *rpl4Δ63–87* mutant, class N3 only comprises about 7% of total particles recovered from the *nog1ΔC rei1ΔC reh1ΔC* mutant. This difference likely reflects how these mutant strains are grown. For the *rpl4Δ63-87* mutant, shifting to glucose for ~17 h likely allows more opportunity to accumulate aberrant particles. In contrast, shifting the triple tail mutant to 16ºC for 5 h is not only a much shorter shift, but it also dramatically lengthens the doubling time of the cells. Both of these things mean that fewer new ribosomes will be produced during the shift and far fewer aberrant pre-ribosomes will accumulate in the cells before purification. This difference may also reflect the severity of the phenotype corresponding to each mutant (see Discussion).

Most notable is class N4. Unlike any classes observed in the *rpl4Δ63–87* mutant, class N4 represents improperly assembled Nog2 state 2 particles; it displays weak density for the Rix1 complex and lacks density for Rea1. Consistent with inefficient recruitment of the Rix1 complex and Rea1, the Rea1-dependent removal of Rsa4 has not yet occurred in class N4 (**Figure 2.20**).

Together, these results indicate that the *nog1ΔC rei1ΔC reh1ΔC* mutant is distinct from the *rpl4Δ63–87* mutant. In this mutant, a smaller fraction of intermediates appears to be blocked at the stage of Nog2 state 1, and the second block appears to be at the state 2 stage, rather than the state 3 stage, of Nog2 particles. These differences between the *rpl4Δ63–87* mutant and the *nog1ΔC rei1ΔC reh1ΔC* mutant may in part result from the absence of the TD of L4 in the former, versus its being present but in a flexible conformation in the latter.

To further characterize the differences between *rpl4Δ63–87* and *nog1ΔC rei1ΔC reh1ΔC* mutant particles, we assessed the protein composition of Nog2-associated pre-60S subunits using SDS-PAGE, western blotting, and iTRAQ mass spectrometry. Purifications were done using wild-type or mutant cells grown at 30°C and then shifted to 16°C for five hours. SDS-PAGE followed by silver staining or western blotting indicated that deletion of the Nog1 CTD does not affect the stability or recruitment of Nog1 into pre-60S subunits (**Figure 2.20a**). In contrast to the *rpl4Δ63–87* mutant, levels of Sda1, Rpf2, and Rrs1 do not change in *nog1ΔC rei1ΔC reh1ΔC* mutant particles relative to wild-type cells (**Figure 2.20b**). Despite the observation that both the exit of Rpf2 and Rrs1 and the entry of Sda1 are unaffected in the *nog1ΔC rei1ΔC reh1ΔC* mutant, levels of the Rix1 complex and Rea1, which are required for stabilization of the 5S RNP in its rotated state, are consistently decreased relative to wild-type (**Figure 2.20b**). These results indicate that, for reasons that are still not entirely clear, *nog1ΔC rei1ΔC reh1ΔC* mutant pre-60S subunits are able to recruit Sda1 but cannot recruit the other machinery necessary for 5S RNP rotation as efficiently as wild-type particles. This unusual protein composition most closely reflects what was observed by cryo-EM of class N4 of the *nog1ΔC re1ΔC reh1ΔC* mutant particles (**Figure 2.20c**).

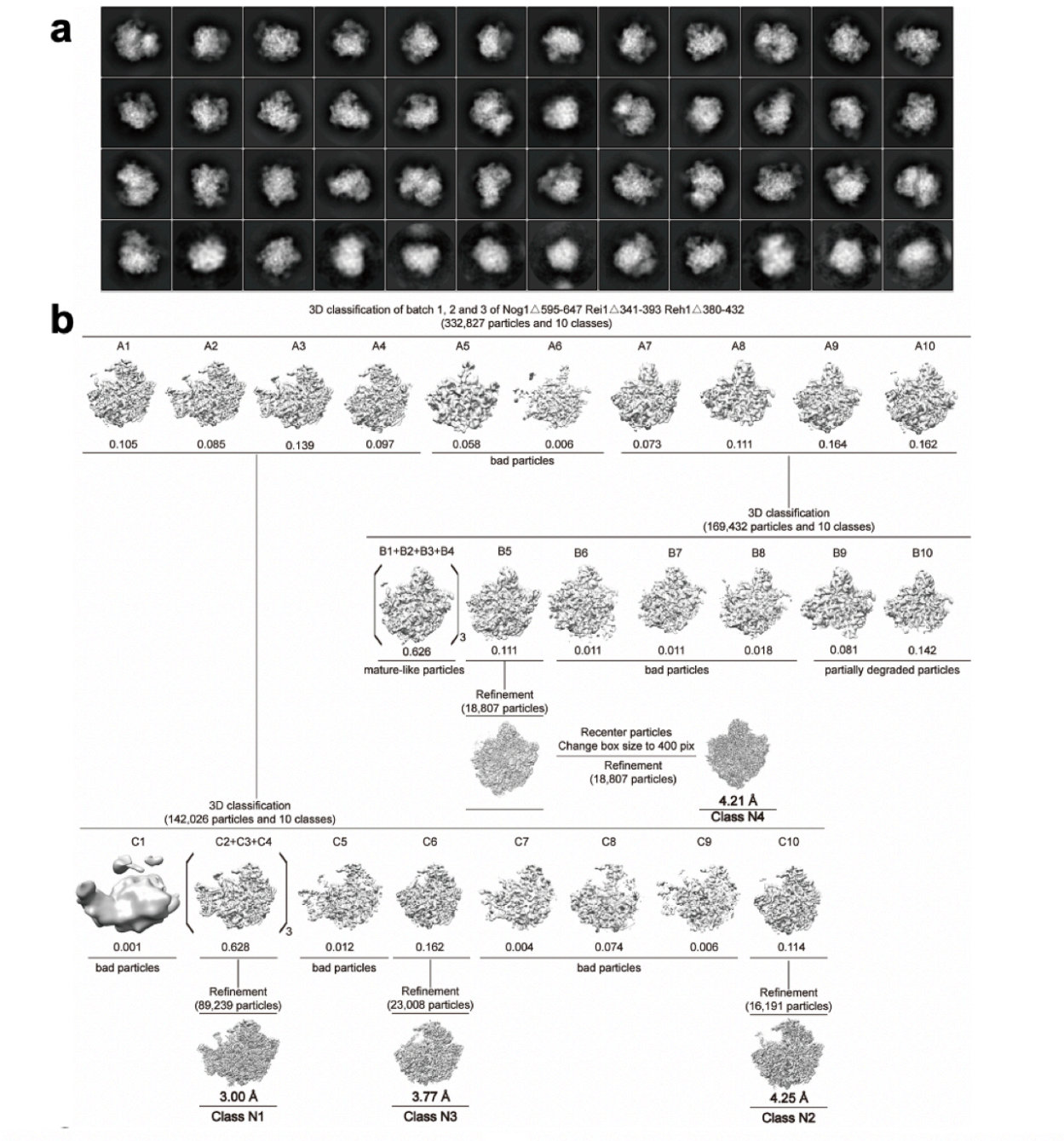

Figure 0.17. Cryo-EM data processing of *nog1ΔC rei1ΔC reh1ΔC* particles.

(a) Representative 2D class averages of *nog1ΔC rei1ΔC reh1ΔC* mutant Nog2 particles.

(b) Flow chart for 3D classification.

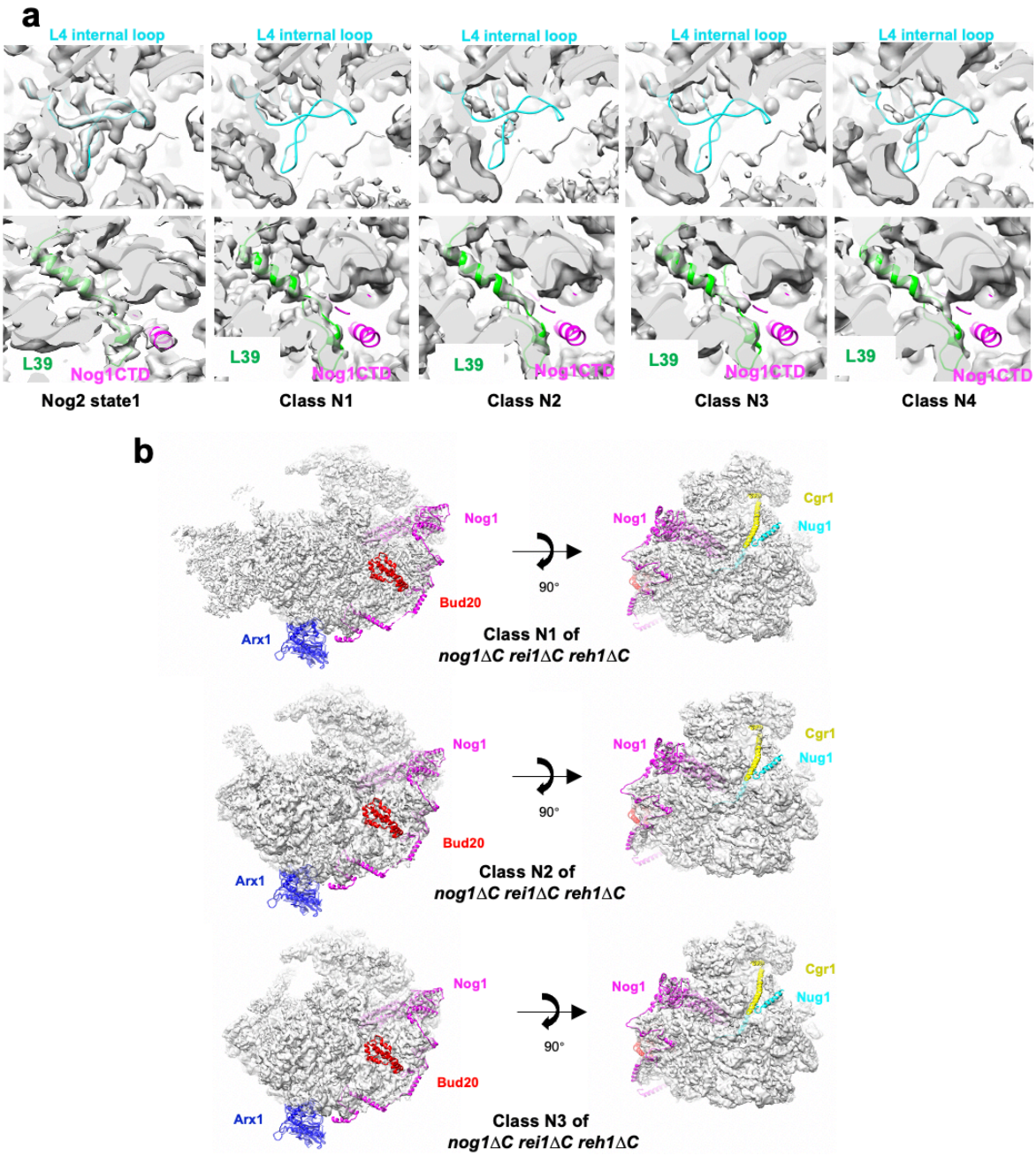

Figure 0.18. The Nog1 CTD stabilizes the tunnel domain of L4.

(a) Density maps of the wild-type Nog2 state 1 and N1–N4 mutant particles are aligned with the atomic model of wild-type Nog2 state 1 particles, displaying the interior of the NPET. Densities (gray) for the L4 TD (cyan) are missing in the NPET in all four mutant

classes (top). Densities for L39 (green) can be visualized in classes N1–N4 but no densities for the Nog1 CTD (magenta) are visible (bottom). **(b)** View of *nog1ΔC rei1ΔC reh1ΔC* classes N1–N3 from the subunit interface. Densities are fitted to the atomic model of wild-type Nog2 state 1 (PDB: 3jct). Exposed cartoon models of Arx1 (blue), the Nog1 CTD (magenta), Bud20 (red), Cgr1 (yellow), and Nug1 (cyan) represent missing densities for each respective protein.

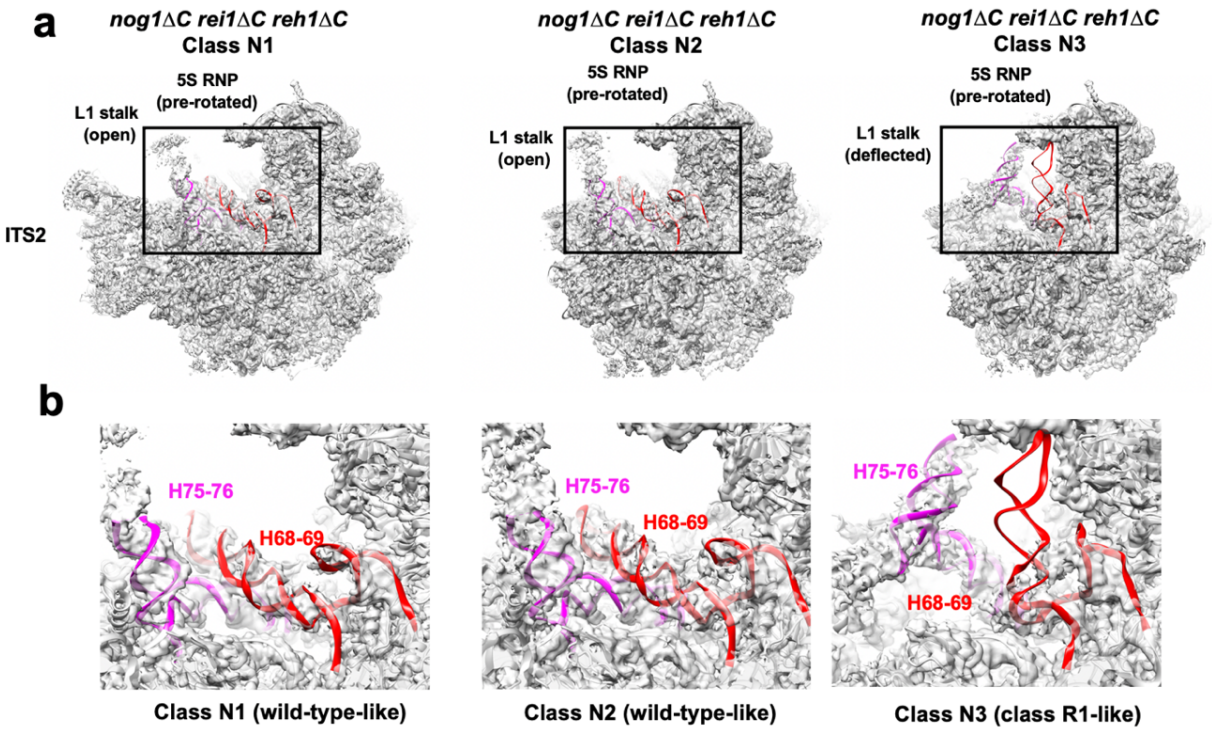

Figure 0.19. A minority of *nog1ΔC rei1ΔC reh1ΔC* mutant pre-60S particles display aberrant rRNA conformations.

(a) Densities of classes N1–N3 of *nog1ΔC rei1ΔC reh1ΔC* mutant particles solved at a resolution of 3.0–6.0 Å. Classes N1 and N2 are aligned with the atomic model of class R2, while class N3 is aligned with the atomic model of class R1. **(b)** View of H68-69 (red) and H75-76 (magenta).

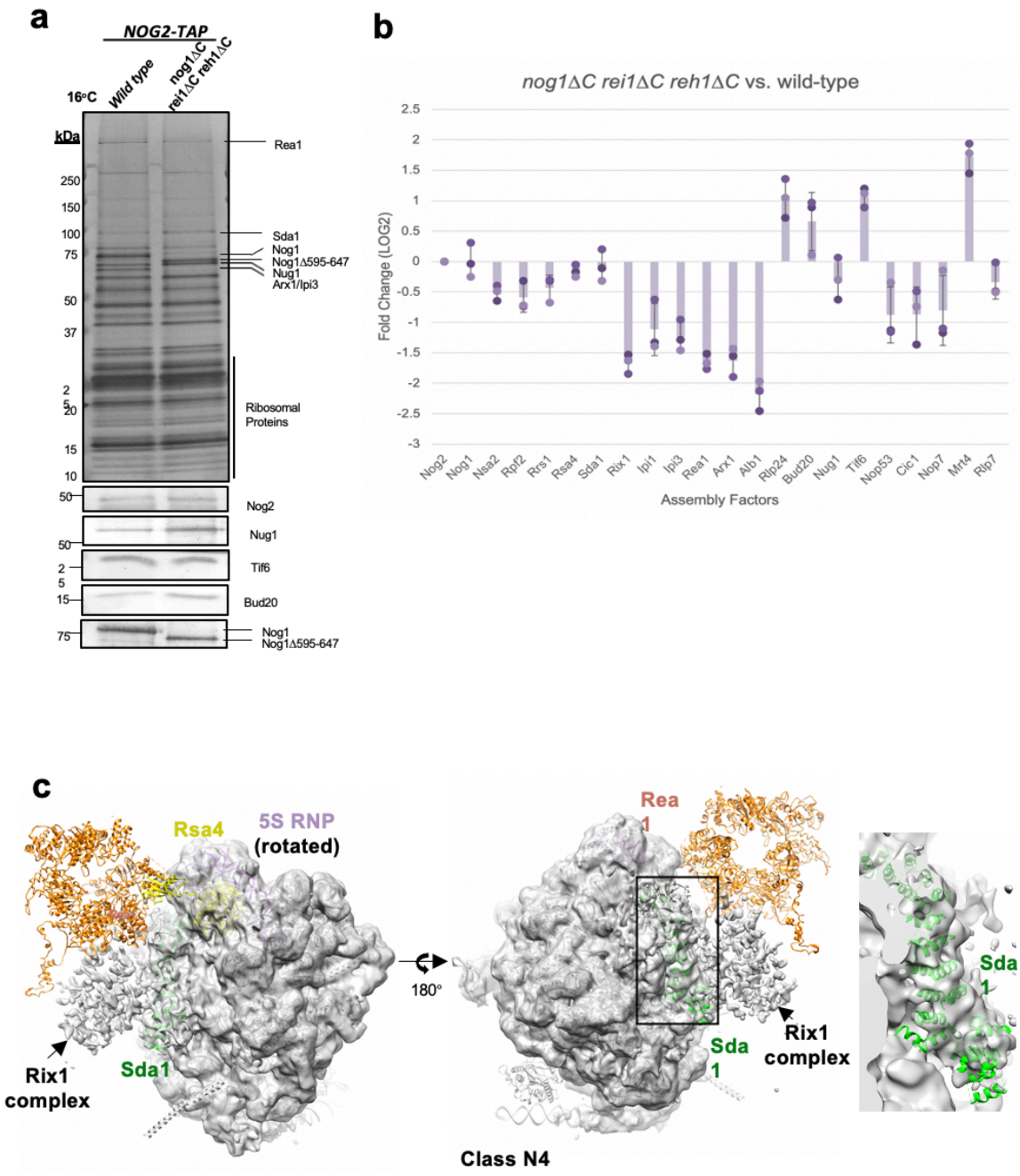

Figure 0.20. Truncation of the Nog1 CTD may affect closing of the L1 stalk.

(a) SDS-PAGE of proteins in Nog2-associated pre-ribosomes affinity purified from wild-type and *nog1ΔC rei1ΔC reh1ΔC* mutants shifted to 16°C for 5 h. Proteins in labeled

bands were identified by mass spectrometry. **(b)** Semi-quantitative iTRAQ mass spectrometry reveals differences in relative amounts of proteins labeled with iTRAQ reagents in Nog2-particles affinity purified from the *nog1ΔC rei1ΔC reh1ΔC* mutant compared to those in wild-type particles. Each bar represents a biological replicate. All protein levels are normalized to the bait protein, Nog2. Ratios are represented on a log2 scale. Error bars represent standard deviation (n = 3). c Densities for class N4 are fitted to the atomic model of the Rix1 particle (PDB: 5fl8). Density for Sda1 (green) can be seen in the particles. The 5S RNP (purple) is in the rotated state in class N4. Weak density can be seen for the Rix1 complex, and Rea1 (orange) is almost completely missing. Rsa4 (yellow) is visible in the particles.

Discussion

The year that I entered the Woolford lab was the same year that the lab had revealed the structure of Nog1 bound to Nog2-associated particles (Wu et al., 2016). In the following years, several more cryo-EM structures of wild-type particles would reveal C-terminal domains of AFs Rei1 and Reh1 occupying the NPET (Greber et al., 2016; Kater et al., 2017; Ma et al., 2017). Even after these revelations, very little of these structural observations had been followed up with biological assays. Thus, we knew next to nothing about how any functional center, including the NPET, was actually constructed in the eukaryotic ribosome.

My studies with Nog1 and L4 are the most in-depth studies done to date concerning construction of any functional center in the yeast ribosome. The results discussed in this chapter demonstrate that stabilization of rRNA helix 74 is absolutely critical to proper construction of the NPET and assembly of the large ribosomal subunit. We were able to identify for the first time a defined role for the C-terminal domain of Nog1 in the NPET and clarify the function of the L4 TD. Prior to this work, there were only two cryo-EM structures of mutant yeast pre-60S ribosomal subunits, and both datasets were of quite low resolution (Barrio-Garcia et al., 2015; Thoms et al., 2018). Therefore, this study, along with the Rpf2 study from our lab (Micic et al., 2020), were the first in-depth analyses of high-resolution cryo-EM structures of pre-60S ribosomal subunits from yeast. The following discussion includes sections from the Wilson et al., 2020 discussion with further elaboration and speculation that could not make it into the published document.

2.1.6 Cryo-EM classification of *rpl4*Δ*63-87* mutant pre-60S ribosomal particles reveals rewiring of the assembly pathway

Previous work purifying Nog2-associated pre-60S particles from wild-type cells yielded three major stable assembly intermediates (Nog2 states 1–3) (Wu et al., 2016), with 5S RNP rotation occurring in Nog2 state 2. Our cryo-EM analysis of Nog2-associated pre-60S particles from the *rpl4Δ63–87* mutant revealed seven different particle states. It is important to note that the cryo-EM dataset for the *rpf2*Δ*C* mutant, which appears to block large subunit assembly during the same interval as the *rpl4*Δ*63-87* mutant, does not include rotated particles or those resembling Nsa1 particles, which we do observe in the *rpl4*Δ*63-87* mutant (Micic et al., 2020). However, cryo-EM analysis of the *rpf2*Δ*C* mutant took place over a year prior to the *nog1* and *rpl4* mutant analyses and it is reasonable to suspect that such particles could have been missed during classification. Regardless, based on our data as well as others' data, I propose a model to explain the chronological progression and fate of each individual *rpl4*Δ*63-87* and *nog1*Δ*C rei1*Δ*C reh1*Δ*C* particle class through the 60S subunit assembly pathway (**Figure 2.21**).

Using the atomic model of class R1 from the *rpl4Δ63–87* mutant, we were able to visualize several rRNA conformational changes that are apparently initiated by the instability of the rRNA linker between H73 and H74, which results in increased flexibility of H74 (**Figure 2.8**). In wild-type particles, H74 is one of the last rRNA helices in the NPET to undergo maturation (**Figure 1.3b**). The absence of the L4 TD results in a flexible H74, which appears to be sufficient to cause H75 to adopt an aberrant conformation. Consequently, H68 cannot remain stably docked on pre-60S subunits,

and the 3-way junction of H75, H76, and H79 becomes destabilized, causing the L1 stalk to adopt a deflected position. Notably, densities for a shifted H75 could also be observed in classes R4 and R6 (**Figure 2.22**). Consistent with this observation, densities for H68 are not visible in either class (**Figure 2.22**), and the L1 stalk is deflected in class R4, the same as R1, indicating that L1 stalk maturation may be affected in early stages of 60S assembly in the *rpl4*Δ*63-87* mutant. In summary, we suggest that a flexible H74, which occurs as a consequence of an improperly formed NPET, can shift rRNA helices 75, 76, and 68 toward aberrant conformations that can affect several stages of 60S subunit assembly when the TD of L4 is absent.

Classes R3 and R4 resemble the early nucleolar intermediates Nsa1 state B and E, respectively, which do not usually co-purify with Nog2 particles (Kater et al., 2017; Wu et al., 2016). However, class R4 contains density for the bait protein Nog2 and is therefore unlikely to be a contaminant. Nog2 may be entering pre-60S particles earlier than in wild-type particles due to stalling of assembly, as we observed previously upon depletion of AF Drs1 (Talkish et al., 2016). This defect in early particles resulting from the absence of the TD of L4 is consistent with the observation that the TD of L4 is first visible (and therefore present in a stable form) in the NPET at this stage of wild-type 60S subunit maturation (**Figure 1.3a**). Class R4 lacks densities for several AFs typically found in State E particles, including Noc3, Spb1, Brx1, and Ebp2. Rather than these AFS failing to assemble into pre-ribosomes, we think that their absence reflects that they have associated and dissociated from pre-60S particles, while the AFs still remaining on particles (Erb1, Ytm1, and Has1) have not yet been released. Otherwise, failure of so many essential AFs to initially bind early assembly intermediates would result in their rapid turnover (Sahasranaman et al., 2011). It remains unclear what the biological

consequences of a deflected L1 stalk in class R4 may be. Therefore, classes R3 and R4 may represent on-pathway particles that are delayed in their progression to middle stages of assembly.

Classes R6 and R7 may result from the following: *rpl4Δ63–87* mutant particles that reach class R2 may subsequently become trapped in class R1, be unable to bind Sda1, and become destined for turnover (class R7). Alternatively, they might progress beyond the 5S RNP rotation checkpoint to class R6. Because densities for H68 are not visible in class R6, we suspect that this flexible intersubunit bridge results in particles destined for turnover (class R5). However, in the case of R6, this flexibility of H68 may not arise until after 5S RNP rotation occurs (**Figure 2.21**). Together, our data suggest that proper maturation of the NPET is necessary to maintain the stability of specific rRNA helices and keep pre-60S particles on-pathway. These mutant classes blocked at various stages may reflect the phenomenon of rerouting ribosome assembly to alternate pathways in response to stress (Mulder et al., 2011; Sanghai et al., 2018).

I wanted to follow up on classes R5 and R6 and to help reconcile previous findings apparently showing a cytoplasmic block in 60S ribosomal subunit assembly associated with a *rpl4Δ63-87* mutant (Stelter et al., 2015). These rotated particles may be able to progress beyond nuclear export and into cytoplasmic stages of ribosome assembly. To address this question, I TAP-tagged the late nucleoplasmic-entering AF Nmd3, which co-purifies primarily with cytoplasmic pre-60S ribosomal subunits, in the *rpl4Δ63-87* mutant. If *rpl4Δ63-87* mutant particles progress to the cytoplasm, purifying Nmd3-associated particles should allow us to study these cytoplasmic particles more closely. As a negative control, I purified Nmd3-associated particles form cells depleted of the AF Nog2, which should halt ribosome assembly prior to nuclear export. Both the *rpl4Δ63-87* and Nog2-

depleted strains yielded similar results in these Nmd3 purifications (**Figure 2.23**). These results suggest that an insignificant fraction of *rpl463-87* mutant particles recruit Nmd3 and undergo export from the nucleoplasm to the cytoplasm. However, it still does not rule out the fact that some fraction of *rpl4Δ63-87* mutant particles do progress to the cytoplasm. It may be that whenever ribosome assembly is blocked, the block is not absolute. All together, these results suggest that ribosome assembly mutants may block multiple stages of assembly, reducing the number of functional pre-ribosomes at each with each block reducing cell viability.

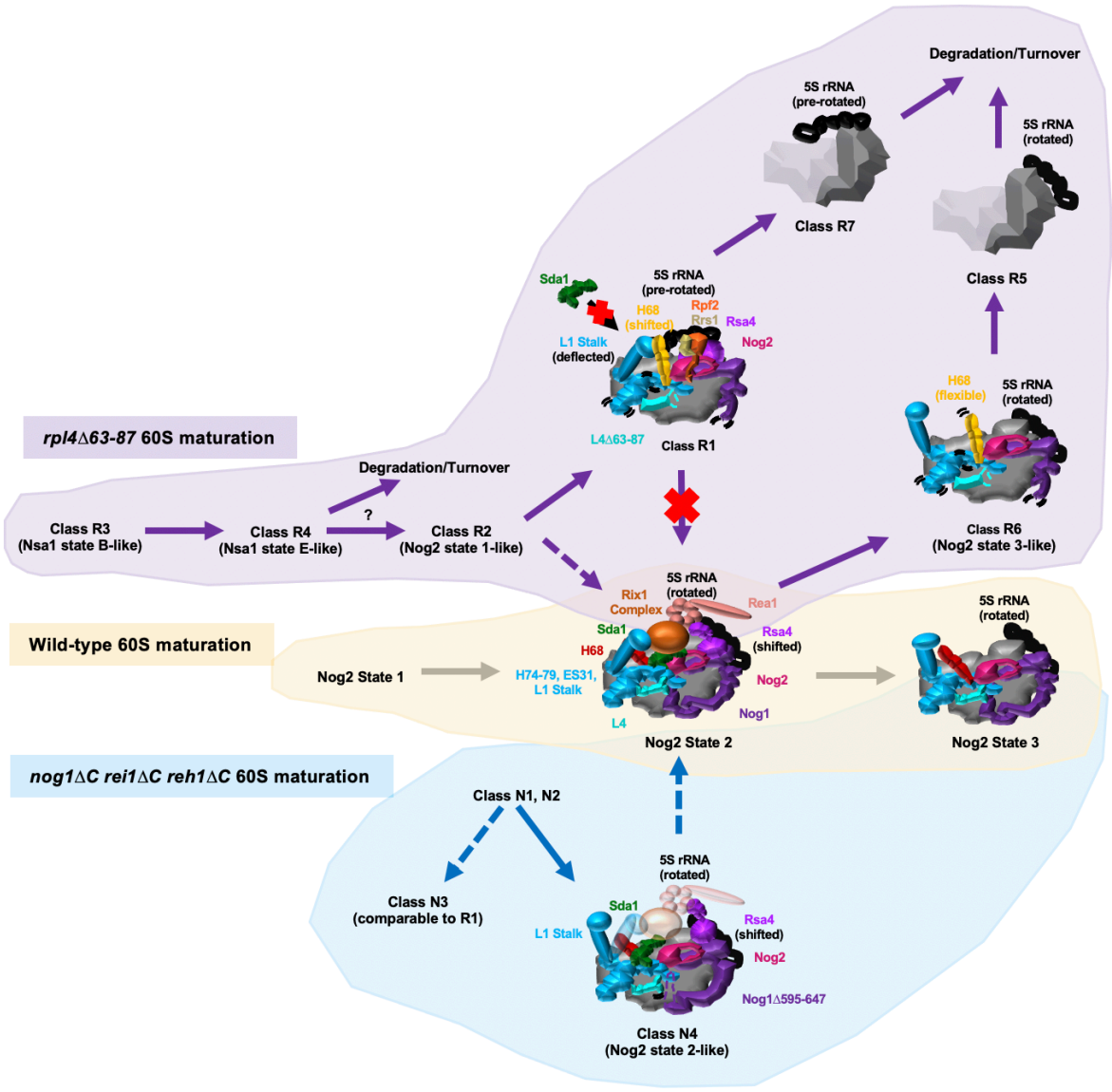

Figure 0.21. NPET maturation in the 60S subunit assembly hierarchy.

In the wild-type 60S subunit assembly pathway (middle, tan), Nog2 state 1 progresses to Nog2 state 2 particles, which have bound AFs Sda1 (dark green), the Rix1 complex (orange), and Rea1 (coral). The L1 stalk has closed, and the 5S rRNA has rotated ~180°. Rsa4 (light purple) has also shifted to face Rea1. These wild-type particles progress to Nog2 state three particles, which have released multiple AFs and are ready

to exchange Nog2 for Nmd3 and be exported from the nucleoplasm to the cytoplasm. In the *rpl4Δ63–87* mutant (top, purple) classes R3 and R4 are the earliest chronological particles to be observed. Some fraction presumably progresses to class R2. Class R2 particles are wild- type-like and likely progress to class R1 particles, which display a shifted rRNA helix H68 (gold) that prevents binding of Sda1 and progression to Nog2 state 2. These class R2 particles are likely precursors to class R7 on a pathway to turnover. Alternatively, some fraction of class R2 particles may progress past Nog2 state 2 to class R6, which displays aberrant conformations of multiple rRNA helices. Consequently, class R6 particles are likely precursors to class R5 on a pathway to turnover. In the *nog1ΔC rei1ΔC reh1ΔC* mutant, wild-type-like classes N1 and N2 (bottom, teal) progress to either N3, which resembles class R1, or class N4. Class N4 primarily displays density for the L1 stalk in an open position and Sda1 is bound, but weak densities (transparent colors) can be seen for the Rix1 complex, Rea1, and the L1 stalk in a closed position. Some fraction of class N4 particles likely progresses to Nog2 state 3. Two curved black lines represent flexibility in protein or rRNA structure. Solid vs. dotted arrows represent major and minor pathways, respectively.

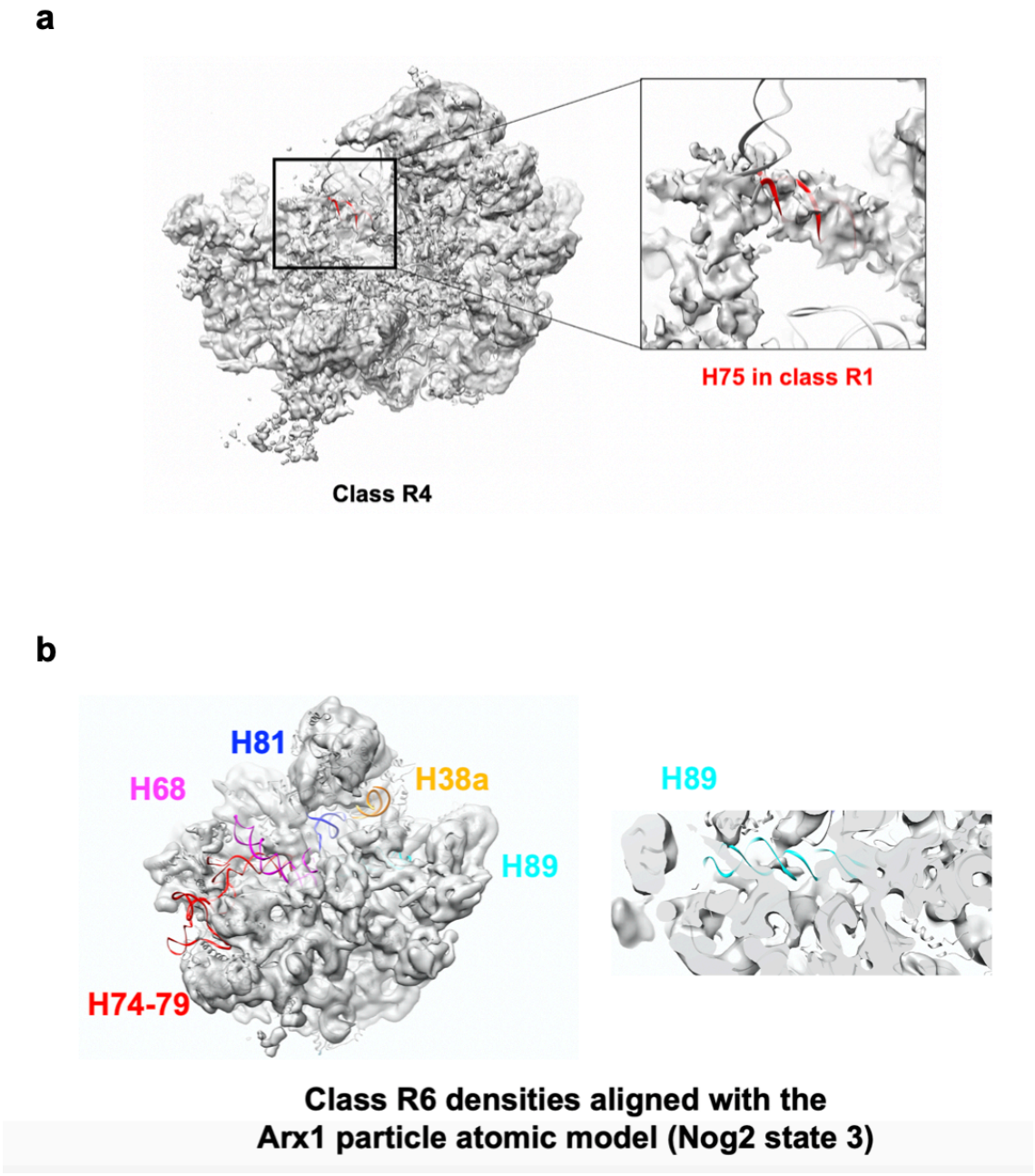

Figure 0.22. Classes R4 and R6 display aberrant rRNA conformations.

(a) Class R4 of the *rpl4Δ63-87* mutant is aligned with the atomic model of class R1. H75 exhibits an aberrant conformation similar to the H75 observed in class R1 (red). **(b)**

Densities for class R6 from the *rpl4*Δ*63-87* mutant are aligned with the atomic model of the Arx1 particle (PDB: 5APO), which resembles Nog2 state 3 particles. Exposed atomic models for rRNA helices 38a (orange), 68 (magenta), 74-79 (red), 81 (blue), and 89 (cyan) represent flexible helices.

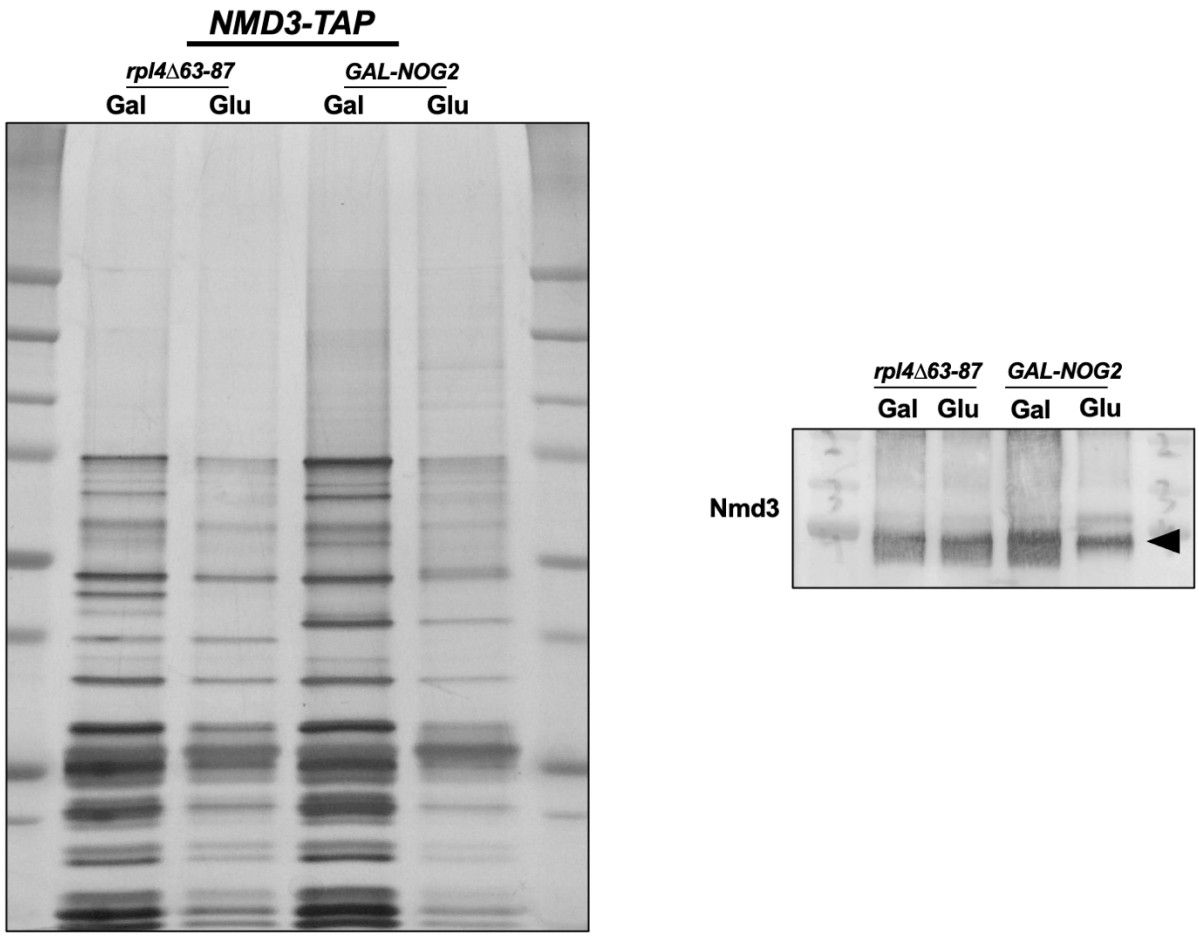

Figure 0.23. Purification of Nmd3-associated particles from the *rpl4Δ63-87* and *GAL-NOG2* mutants.

2.1.7 Explaining the distinct phenotypes of different NPET mutants

Deletion of the TD of L4 consistently resulted in more extreme phenotypes than those observed in *nog1* CTD mutants (including the triple tail mutant). For example, the *rpl4Δ63–87* mutant is lethal at all temperatures, whereas the *nog1* CTD mutants exhibited severely reduced growth only at 16°C (**Figure 2.13**). The different extent to which maturation of pre-60S subunits is blocked in *rpl4* compared to *nog1* mutants may reflect the difference between the absence of the L4 TD (*rpl4Δ63–87*) vs. the TD being present but in a flexible state (*nog1ΔC rei1ΔC reh1ΔC*). This milder effect in the triple tail mutant is also consistent with the observation that class N3, which contains the same aberrant rRNA conformations as class R1 of *rpl4Δ63-87* mutant particles, makes up only 7% of the total particles obtained from the *nog1ΔC rei1ΔC reh1ΔC* while class R1 makes up 27% of *rpl4Δ63–87* mutant particles (**Figure 2.4b**). When flexible, the TD of L4 might still stabilize H74 enough to maintain growth at 30°C in rich media. However, the potential for this rRNA to become trapped in unproductive rRNA conformations might increase at lower temperatures and result in cold sensitivity (Chursov et al., 2013). Alternatively, or in addition, the lack of L39 in the NPET of *rpl4Δ63–87* mutant particles could help explain the difference between the *rpl4* and *nog1* mutants. While L39 is not essential for growth, *rpl39Δ* mutants do exhibit growth defects (Steffen et al., 2012). Although it is unclear how L39 is loaded into pre-60S subunits and why exactly deletion of the L4 TD prevents this, L39 may fine-tune NPET assembly.

My results also suggest that Nog1 plays the most important role of the three tunnel-occupying AFs Nog1, Rei1, and Reh1 during ribosome assembly. Analogous C-

terminal truncation of Rei1 has minimal effects on cell growth at all temperatures, while *reh1Δ* cells have no obvious growth defect (Greber et al., 2016; Parnell and Bass, 2009). Nevertheless, our triple truncation mutant, *nog1ΔC rei1ΔC reh1ΔC*, displayed a slightly slower growth rate at 30°C than the *nog1Δ595–647* single mutant. Previous studies also revealed that pre-60S ribosomal subunits from *rei1*Δ*reh1*Δ mutant cells were sensitive to high salt concentrations (Parnell and Bass, 2009). While I could not replicate these results with *nog1*Δ*595-647 rei1*Δ mutant cells (this was using a plasmid-borne *nog1* mutant) (**Figure 2.24**), these experiments were not repeated with the genomic *nog1* or *nog1*Δ*C rei1*Δ*C reh1*Δ*C* mutants. All of this together leaves the possibility that the NPET-occupying amino acids in the CTDs of either Rei1 or Reh1 perform a still unknown function.

Another and perhaps more interesting hypothesis to explain the growth defects of the *nog1*Δ*C rei1*Δ*C reh1*Δ*C* mutant suggests a defect in the function of the NPET in mature ribosomes that made it through the assembly pathway, due to mistakes made during ribosome assembly. These mistakes could manifest as a failure of the mature large ribosomal subunit to sense pausing peptides and enter a stalled state during translation (Wilson et al., 2016). Alternatively, translation fidelity may suffer in these mutants, resulting in translational frameshifting. Tools exist to study both of these phenomena and could be used to address this question (Gaba et al., 2005; Harger and Dinman, 2003). Ultimately, these questions would best be answered by ribosome profiling experiments (Brar and Weissman, 2015).

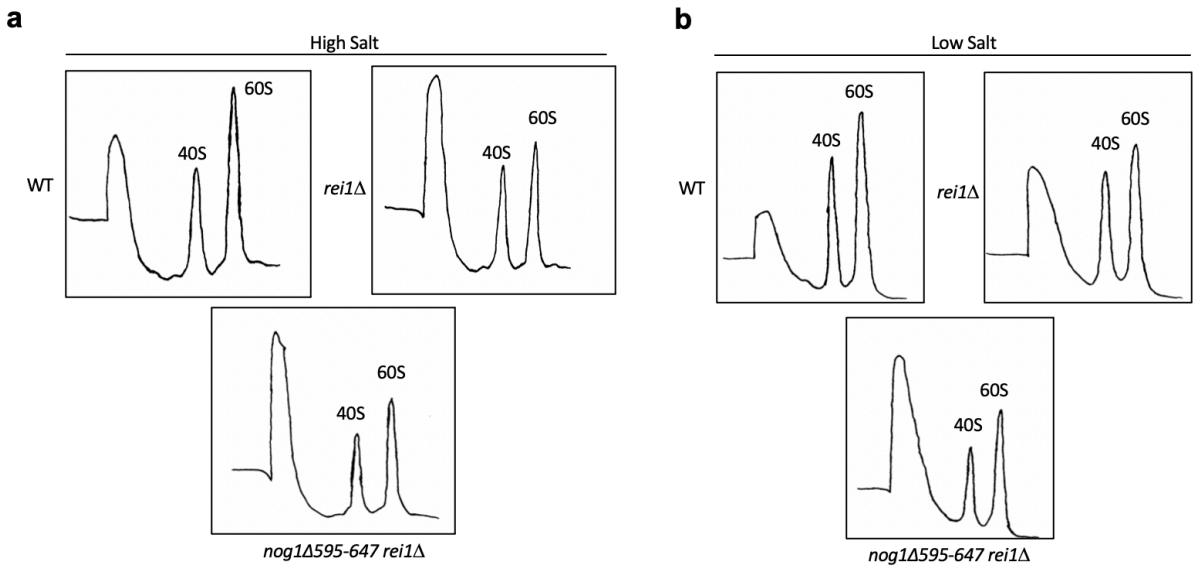

Figure 0.24. Measurement of ribosomal subunit levels in *nog1* mutations under high salt conditions.

2.8 Proper dynamics of the L1 stalk may be necessary for completion of 5S RNP rotation and depend on construction of the NPET

Class N4 particles from the *nog1ΔC rei1ΔC reh1ΔC* mutant resemble Nog2 state 2 particles but lack density for Rea1 and display weak density for the Rix1 complex (**Figure 2.20**). The only other deviation from wild-type Nog2 state 2 in class N4 is that the L1 stalk adopts a predominantly open conformation as opposed to a closed one. This interpretation is based on the weak density of the L1 stalk, which suggests that a fraction of class N4 particles contain a closed L1 stalk while some fraction contain an open L1 stalk. Meanwhile, Sda1 does not exhibit weak density, suggesting that all of the particles in this class contain Sda1 and a rotated 5S RNP. While this particle makes up a minor fraction of total particles (5.6%), it is possible that failure to close the L1 stalk may explain why the Rix1 complex and Rea1 are not stably associated with pre-60S subunits even though Sda1 is present.

Curiously, overexpression of *SDA1* in the triple tail mutant appeared to worsen growth relative to wild-type and overexpression of other genes (**Figure 2.25**). This could be attributed to aberrant binding of Sda1 to mutant *nog1ΔC rei1ΔC reh1ΔC* particles by mass action. In other words, rRNA helices in these mutant pre-60S ribosomal particles may fall into kinetic folding traps when grown at 16ºC. These kinetic folding traps may correct themselves through random thermal movement some fraction of the time (Duss et al., 2019). Perhaps overexpression of Sda1 locks these kinetic traps and prevents them from re-folding.

This is perhaps the most speculative model I suggest in this chapter. It may be that, in wild-type cells, some unclear mechanism involving Cgr1 releases Rpf2 and Rrs1 from the pre-60S ribosomal subunit, allowing Sda1 to bind. Then, or at the same time, the L1 stalk closes and helps create the binding platform for the Rix1 complex. Experiments assaying the depletion of L1 or truncation of the rRNA that makes up the L1 stalk do not disagree with this interpretation but also do not specifically support it (Musalgaonkar et al., 2019). The flexible L4 TD in the *nog1ΔC rei1ΔC reh1ΔC* mutant may subtly perturb the conformation of H74, which could be propagated to H75 and then to H76 in the L1 stalk. These perturbations might affect the closing of the L1 stalk in ways that we do not yet fully understand.

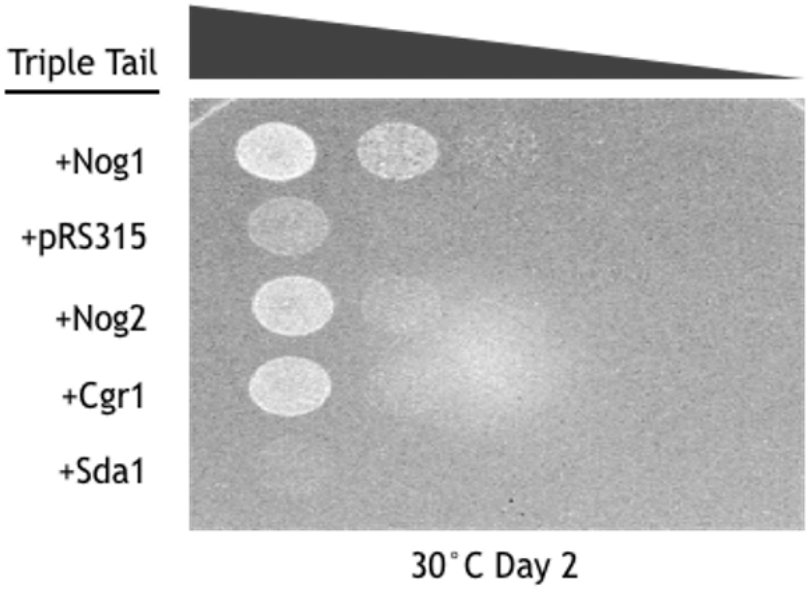

Figure 0.25. Overexpression of assembly factors in the *nog1ΔC rei1ΔC reh1ΔC* (triple tail) background.

2.1.9 Anchoring of the Nog1 C-terminal domain in the NPET is required for recruitment of Arx1 to the pre-60S ribosomal subunit

A consistent defect observed across all cryo-EM classes from both mutants was the lack of the nonessential AF and export adaptor, Arx1. Early on in this project, I found that knocking out Arx1 rescued the cold-sensitive growth defects of a Nog1-TAP mutant (**Figure 2.26**). This essentially replicated the results of Hung and Johnson, 2006, which details the following story. Normally, Rei1 is necessary for the removal of Arx1 from pre-60S subunits. When this fails to occur, Arx1 remains bound to pre-ribosomes as they are exported to the cytoplasm, resulting in an extreme cold-sensitive growth defect and slow growth at 30ºC. However, when Arx1 cannot assemble into pre-ribosomes, these growth defects are rescued and monomeric, unassembled Arx1-GFP can be found in the nucleoplasm (Hung and Johnson, 2006). Hung and Johnson also found that TAP-tagging a ribosomal protein such as L25 could also rescue the *rei1*Δ growth defects by sterically blocking Arx1 from binding to pre-60S ribosomal subunits. Since portions of the Nog1 CTD that lie just outside the NPET interact with Arx1 (Wu et al., 2016), we reasoned that the flexibility or absence of the Nog1 CTD in our mutants may prevent stable assembly of Arx1. Consistent with the assembly defect of Arx1, we observed that upon truncation or tagging of the Nog1 CTD in an *rei1Δ* strain, Arx1-GFP was located in the nucleoplasm (**Figure 2.27**). These results indicate that the Nog1 CTD recruits Arx1 to pre-60S subunits, contributing to the export competency of pre-60S subunits and indirectly serving as a quality control function for the NPET.

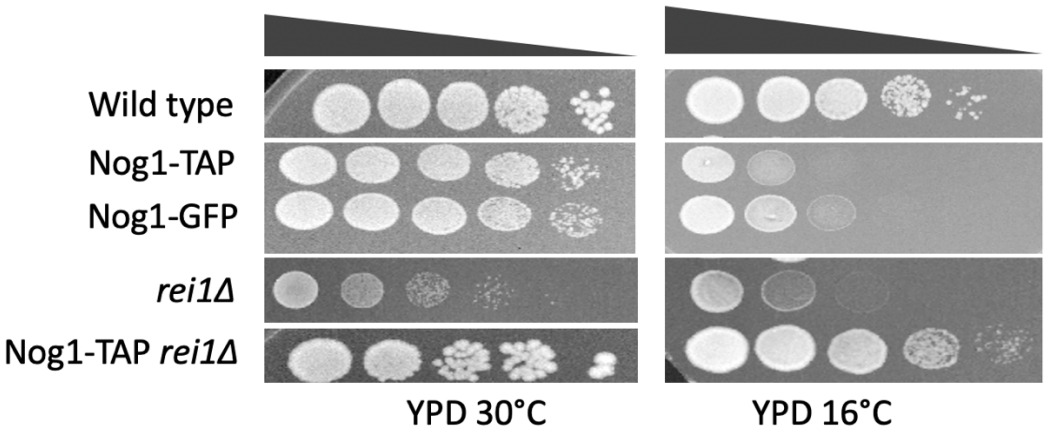

Figure 0.26. **Nog1-TAP rescues the growth defects observed in an *rei1*Δ strain**.

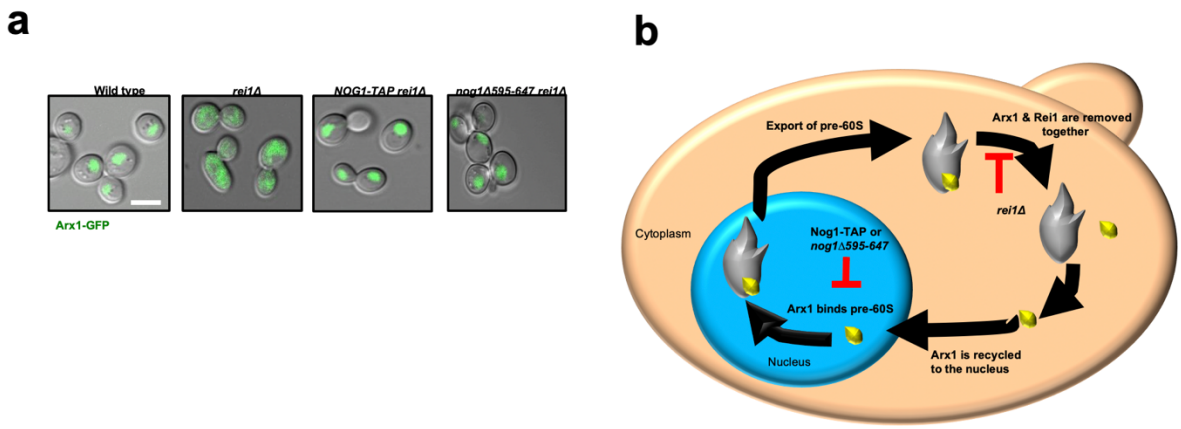

Figure 0.27. The Nog1 CTD is required to recruit Arx1.

(a) Confocal microscopy of Arx1-GFP cells in different genetic backgrounds. Scale bar: 5μm. (b) Model representing the effect that different AF mutations have on the cycle of Arx1 (yellow) binding and release from pre-60S subunits.

2.1.10 Conclusion

It is vital to the cell's survival that the constriction sites in the NPET are assembled properly, since these sites impact protein synthesis. In bacteria, deletion of the internal loop of L4 results in a cold-sensitive growth defect and a failure to respond to the cmlACrb pausing peptide during protein synthesis (Lawrence et al., 2016). Mutations in the NPET have also been shown to confer resistance to the macrolide antibiotic, erythromycin (Halfon et al., 2019; Wekselman et al., 2017).

Several previous results offered early clues that mechanisms may operate to couple NPET construction with other remodeling events during 60S subunit assembly (Gagnon et al., 2016; Wilson et al., 2016; Wu et al., 2012). For example, translating ribosomes that are stalled in response to small molecules, peptides, or antibiotics that bind to the NPET display a distorted PTC incapable of catalyzing peptide bond formation (Vázquez-Laslop and Mankin, 2018). Furthermore, defects in bacterial ribosomes lacking a 5S RNP can be partially rescued by the binding of a macrolide antibiotic, which binds to the NPET (Khaitovich et al., 1999). Our data and proposed model suggest that this communication between the NPET and other ribosomal domains can indeed occur during ribosome assembly, and that failure to do so can halt at least three stages of maturation.

In this study, we set out to gain a deeper understanding of how construction of a functional center such as the NPET could fit into the known hierarchy of 60S subunit assembly. Since crucial features of the NPET lie deep within the core of the pre-60S subunit, cells need to be able to detect such subtle but impactful defects in NPET assembly. By coupling NPET construction with the stability of critical rRNA helices, cells

might easily identify and terminate assembly of particles harboring a defective NPET. This study opens up the possibility that construction of other functional centers in the eukaryotic ribosome may be regulated in a similar fashion and lays the foundation for future study of mutant 60S subunits using cryo-EM.

Materials and Methods

Construction of mutant plasmids

Plasmids containing each AF gene were obtained from the Yeast Genomic Tiling Collection (Open Biosystems), and used as templates in a multi-step PCR protocol for inserting unique restriction sites upstream and downstream of the gene (Gamalinda et al., 2014). PCR products were digested using restriction enzymes and ligated into pRS315 containing the *LEU2* gene. Mutagenesis of ORFs was performed using the Quickchange Site-directed Mutagenesis Kit (Agilent Technologies). Correct mutations were confirmed by sequencing (Genewiz).

Generation of yeast strains

All genomic epitope tags, GAL-promoter fusions, knockouts, or C-terminal truncations were constructed according to standard methods (Longtine et al., 1998). The *nog1ΔC rei1ΔC reh1ΔC* triple truncation strain was made by truncating one assembly factor gene at a time. A strain conditional for expression of only *rpl4Δ63–87* was constructed as follows. First the endogenous promoter of *RPL4A* was replaced with the conditional GAL promoter, plus the HA-epitope in-frame with the *RPL4A* ORF. Then, *RPL4B* was knocked out by replacement of the ORF with KanMX. This *GAL-HA-RPL4A rpl4bΔ* strain was transformed with a *LEU2* plasmid pRS315 containing *rpl4aΔ63–87*. Arx1-GFP strains were a generous gift from Arlen Johnson (University of Texas at Austin).

Growth assays

Yeast strains were grown to an OD_{600} of ~0.5 in permissive conditions and then serially diluted out to 10−5-fold before pipetting 10–15 µL of each dilution onto appropriate galactose- or glucose-containing solid media. Plates were checked daily after being incubated at 30 or 16°C.

Sucrose density gradient analysis

Pre-ribosomes, ribosomes, and polyribosomes were fractionated from 40 OD_{254} units of yeast whole-cell extracts on 7–47% (w/v) sucrose gradients (Biedka et al., 2018; Deshmukh et al., 1993). Five milligrams of cycloheximide (Sigma) was added to 150 ml of culture 20 min before harvesting the cells. Extracts were made using lysis buffer (10 mM Tris-HCl pH 7.5, 0.1 M NaCl, 30mM MgCl2,50 µg/ml cycloheximide, 200 µg/ml heparin, and 0.2% diethyl pyrocarbonate). Cells were vortexed eight times for 30 s with glass beads (0.5 mm diameter, Biospec Products), kept on ice in between vortexing, and clarified by two consecutive centrifugations. Forty OD_{254} units of whole-cell extracts were layered on 7–47% (w/v) sucrose gradients, and pre-ribosomes, ribosomes, and polyribosomes were fractionated according to the manufacturer's protocol (Teledyne ISCO). The sucrose gradients were spun in an ultracentrifuge for 4 h. A Foxy R1 density gradient fractionator was used to fractionate and analyze gradients with continuous monitoring at OD_{254}. High salt gradients used to separate monosomes and polysomes into 40S and 60S subunits were done according to previously described methods (Parnell and Bass, 2009). Gradients were composed of sucrose as described above in addition to 50 mM Tris-HCl, pH 7.5, 50 mM KCl (low salt) or 800 mM KCl (high salt), 10 mM $MgCl_2$, and 1 mM DTT.

Fluorescence microscopy

The intracellular location of pre-ribosomes or AFs was determined as follows: 35 mm glass bottom microwell dishes (MaTek) were coated with concanavalin A (Sigma) and allowed to dry for 40 min. Cells expressing GFP-tagged L25 or Arx1-GFP were grown to an OD_{600} of 0.3–0.5 before plating 10 µL onto the glass bottom of the MaTek dish and incubating at room temperature for 20 min. Plates were then washed once with 1 mL of appropriate media before being overlaid with 2 mL of media and then imaged using a Ziess LSM 880 confocal microscope. Images were processed using Fiji (Schindelin et al., 2012).

Analysis of pre-rRNA processing

Steady-state levels of pre-rRNAs were assayed using northern blot and primer extension analysis (Jakovljevic et al., 2012). Ten milliliter of cells were harvested, frozen, and RNA was extracted using phenol. Five microgram of RNA was used for primer extension reactions or loaded onto a formaldehyde/MOPS agarose gel for northern blotting. 32Pγ -ATP radiolabeled oligonucleotide probes for specific pre-rRNAs were used in primer extension reactions and for hybridization in northern blots. For northern hybridization of small molecular weight RNAs (7, 6, 5.8, and 5S), RNA samples were mixed with an equal volume of sample buffer (0.1× TBE buffer, 10M urea, 0.1% xylene cyanol, 0.1% bromophenol blue) and subjected to electrophoresis on a 5% acrylamide/7M urea gel for 4 h at 120 mA. Following electrophoresis, gels were electroblotted to a Nytran N membrane (GE Healthcare Life Sciences) using a Trans-

Blot Plus Cell (Biorad), hybridized with an end-labeled oligonucleotide, washed, and exposed to X-ray film.

Affinity purification and analysis of pre-ribosomes by silver staining, western blotting, and iTRAQ mass spectrometry

The protein composition profiles of affinity-purified pre-ribosomes was analyzed by SDS-PAGE (4–20% Tris-glycine and 4–12% Bis-Tris, Thermo Fisher Scientific) followed by silver staining (Sahasranaman et al., 2011). Western blotting tested incorporation of specific proteins into pre-ribosomes (Biedka et al., 2018). Pre-ribosomes were purified by lysing frozen cells using acid-washed glass beads and TNM150 buffer consisting of 50mM Tris HCl pH 7.5, 150 mM NaCl, 1.5 mM MgCl2, 0.1% NP-40 (Sigma–Aldrich), and 5 mM βME. Following lysis, lysates were incubated with IgG-conjugated Dynabeads while rocking for 1 h at 4 °C. Dynabeads were washed with TNM150 buffer (for iTRAQ, this step excluded NP-40). Samples were eluted using TEV protease while rocking for 1 h at room temperature, then precipitated with 10% TCA and washed with 100% cold acetone. Purified samples were sent to the Penn State Hershey Core Research Facilities for trypsin digestion and 4-plex labeling with iTRAQ reagents 114, 115, 116, 117 (Applied Biosystems).

Purification of pre-ribosomes for cryo-EM

Preparation of Nog2-associated particles described here required 20 L of cells grown to an OD_{600} of 0.8–1.0 in appropriate media. Frozen cell pellets were lysed using TAP lysis buffer consisting of 50mM Tris-HCl pH 7.5, 100 mM NaCl, 10mM MgCl2, and 0.075% NP-40 (Sigma–Aldrich). Lysates were incubated with IgG-conjugated

Dynabeads while rocking for 1 h at 4°C. Dynadeads were washed using TAP lysis buffer three times and then washed twice using TEV cleavage/resuspension buffer (TAP lysis buffer with NP-40 excluded). Samples were eluted using TEV protease while rocking for 1 h at room temperature. The eluate was then added to a 100 K centrifugal filter (Millipore), prewashed with TEV cleavage-resuspension buffer, and spun at 14,000 × g for 5 min at 4°C. The flow through was discarded and the sample was recovered by inverting the filters and spinning again at 1000 × g for 2 min before being stored at −80°C until preparation for cryo-EM.

Cryo-EM data acquisition

Vitrified specimens were prepared by adding 4 µl samples of *nog1ΔC rei1ΔC reh1ΔC* or *rpl4Δ63–87* particles at a concentration of ~150 nM to a glow-discharged holey carbon grid (Quantifoil R1.2/1.3) covered with a freshly made thin carbon film. Grids were blotted for 0.5 s and plunge- frozen into liquid ethane using an FEI Vitrobot Mark IV (4°C and 100% humidity). The cryo-grids were initially screened at a nominal magnification of 92,000× in an FEI Talos Arctica microscope, operated with an acceleration voltage of 200 kV. Good-quality grids were transferred to an FEI Titan Krios electron microscope that was operating at 300 kV. Images were recorded using a K2 Summit direct electron detector (Gatan) in counting mode at a nominal magnification of ×105,000 (for the rpl4Δ63–87 sample) and ×130,000 (for the nog1ΔC rei1ΔC reh1ΔC sample), respectively (pixel sizes on the object scale are 1.373 and 1.052 Å, respectively), with the defocus ranging from −1.0 to −2.0 µm. Coma-free alignment was manually optimized and parallel illumination was verified before data collection. All micrographs with the K2 camera were collected semi-automatically by SerialEM

(Mastronarde, 2005) under low-dose conditions. Each micrograph was dose-fractionated to 32 frames with a dose rate of ~10.0 counts per physical pixel per second for a total exposure time of 6.4 s.

Cryo-EM data processing

Original image stacks were summed and corrected for drift and beam-induced motion at the micrograph level using the MotionCor2 program (Zheng et al., 2017). The SPIDER (Shaikh et al., 2008) software was used for micrograph screening. The contrast transfer function parameters of each micrograph were estimated by Gctf (Zhang, 2016). All 2D and 3D classification and refinement were performed with RELION3.0 (Scheres, 2012). The local resolution map was estimated using ResMap (Kucukelbir et al., 2014). For the *rpl4Δ63–87* mutant sample, a total of 5003 micrographs were collected and 883,649 particles were picked for a cascade 2D and 3D classification with a binning factor of two. About 57% of particles were removed during several rounds of 2D and 3D classification, and 382,748 particles were split into ten classes during the final round of 3D classification. After the final round of 3D classification, a total of 103,319 particles were applied for high-resolution refinement (without binning), resulting in a 3.12 Å map (gold-standard FSC 0.143 criteria). A total of 47,025 particles were applied for high-resolution refinement (without binning), resulting in a 3.22 Å map. In addition to these two states, class R3 is similar to the state B of Nsa1- particles (Kater et al., 2017) and class R4 is similar to the state E of Nsa1-particles but with already assembled 5S RNP (in the premature rotated state). Classes R5-R7 also have well resolved structural features; but they lack densities for major domains of rRNA, suggesting that they are

likely turnover products. For the *nog1ΔC rei1ΔC reh1ΔC* mutant sample, a total of 9115 micrographs

were collected and 1,009,266 particles were picked for cascade 2D and 3D classification with a binning factor of four. About 67% of particles were removed during three rounds of 2D classification, and 332,827 particles were split into ten classes during the first round of 3D classification, with a map of the premature 60S ribosomal subunit (EMD-6615) (low-pass filtered to 60 Å) as the initial model. Based on the map features (the presence of ITS2 and rotation of the 5S RNP), classes were combined into two groups and were subjected to a second round of 3D classification. The first group, with the 5S RNP in premature state, was classified into ten classes. A majority of them (62.8% particles, class N1) represent a state very similar to the state 1 of wild-type Nog2-particles17. A total of 89,239 particles were applied for high-resolution refinement (without binning), resulting in a 3.00 Å map. The second group, with the 5S RNP in mature-like position, containing 169,432 particles, was also subjected to a second round of 3D classification into ten classes. Around 62.6% of these particles are mature or mature-like 60S subunits.

Model building and refinement

An atomic model of wild-type Nog2-TAP state 1 (PDB: 3jct) (Wu et al., 2016) was used as the initial template for modelling. The models of the rRNAs (25S, 5.8S, 5S, ITS2 RNA) were docked into the density map manually using UCSF Chimera (Pettersen et al., 2004). For RP and AF modelling, structures of individual proteins were separately fitted into their density by rigid-body docking. After the initial fitting, the entire chains of rRNAs and proteins were manually checked and adjusted with COOT (Emsley and Lohkamp,

2010). The atomic model of classes R1 and R2 of the *rpl4Δ63–87* mutant particles were further refined against the density map first by real-space refinement (phenix.real_space_refine) (Afonine et al., 2012) in PHENIX (Adams et al., 2010), with secondary structure restraints, geometry restraints and RNA-specific restraints applied. After refinement, alternating rounds of manual model adjustment using COOT and model refinement using PHENIX were applied. The atomic models were cross-validated according to standard procedures (Amunts et al., 2014; Zhao et al., 2015). Specifically, the coordinates of the final model were randomly displaced by 0.2 Å using the PDB tools of Phenix. The displaced model was refined against the Half1 map (produced from a half set of all particles during refinement by RELION). The refined model from Half1 map was compared with the maps of Half1, Half2 in Fourier space to produce two FSC curves, FSC_{work} (model versus Half1 map) and FSC_{free} (model versus Half2 map), respectively. Another FSC curve between the refined model from Half1 and the final density map (model versus full) from all particles was also produced. As indicated by these curves, the agreement between FSC_{work} and FSC_{free} (no large separation) indicated that the model was not overfitted. MolProbity (Chen et al., 2010) (http://molprobity.biochem.duke.edu/) was used to evaluate the final model.

Chapter 3: APPENDIX

Part 1: The role of the tunnel domain of L17 in NPET assembly

When I started working on the tunnel domain (TD) of L4 and the Nog1 CTD, Amber LaPeruta and I were also interested in studying the role of RP L17 in tunnel construction. Depletion of L17 was shown to cause accumulation of 27SB pre-rRNA, block nuclear export, and results in a failure to assemble the AF Nsa2 (Gamalinda et al., 2013). However, the TDs of both L4 and L17 help form the constriction sites of the NPET (Dao Duc et al., 2019; Mankin, 2006) and, at the time, only mutations of the L4 TD had been shown to cause ribosome assembly defects (Gamalinda and Woolford, 2014b; Stelter et al., 2015) while the TD of L17 had remained uninvestigated in a similar context. Similar to L4, mutations of the internal loop of L17 in *E. coli* was shown to confer resistance to macrolide and ketolide antibiotics (Chittum and Champney, 1994; Zaman et al., 2007). Given this information available to us in 2016, we decided to make deletions in the L17 TD and assay the effects of such mutations on ribosome assembly with a tangential goal of comparing and contrasting any effect we uncover with the similar L4 mutations.

3.1.1 L17 tunnel domain mutants cause unclear defects in ribosome assembly

Together, Amber LaPeruta and I constructed and assayed two L17 internal loop mutants for ribosome assembly defects, one in which the entire internal loop was

deleted (*rpl17*Δ*loop*) and one in which five amino acids from the TD were deleted and fused with two glycine residues (*rpl17*Δ*tip*) (**Figure 3.1**). These mutants were made on pRS315 plasmids containing the *RPL17A* gene and transformed into *GAL-HA-L17A rpl17b*Δ cells. Growth of these mutants on selective media at 30ºC yielded confusing results. Not only did the *rpl17*Δ*loop* mutant display a dominant growth defect when the cells were grown on galactose, but the *rpl17*Δ*tip* mutant seemed to display a more severe growth defect than the *rpl17*Δ*loop* mutant when grown on glucose (**Figure 3.1**).

Nop7 is an AF that we commonly use in the Woolford lab as the first AF to use as bait in affinity-purifications of pre-ribosomes from new mutants that we know little about (Harnpicharnchai et al., 2001). The reason for this is that Nop7 enters assembling ribosomes during early nucleolar stages of assembly and appears to dissociate during late nucleoplasmic stages of assembly (Biedka et al., 2018). This means that Nop7-TAP pull-downs enable us to assay large windows of the ribosome assembly pathway all at once and immediately offer insight into which stage of ribosome assembly is affected in any given mutant.

Therefore, we used Nop7-TAP as bait to purify pre-ribosomes from these L17 mutants in order to help explain these growth defects. These results revealed multiple changes in protein levels. We were able to identify known bands on the silver stained SDS-PAGE gel and perform western blotting for proteins that we had antibodies available for (**Figure 3.2**). Ultimately, these results were inconclusive. These experiments revealed changes consistent with a classic “B-phenotype,” where mutants that accumulate 27SB pre-rRNA display a common set of protein deficiencies (Talkish et al., 2012). However, the notable exception to this B-phenotype is that we could not observe a decrease in the AF Nog2, which is a hallmark of the B-phenotype. This

observation, combined with the confusing growth results, led us to the decision to not pursue these mutants further and instead pursue the much more promising L4 mutants. Currently, Fiona Fitzgerald in our lab is revisiting L17 by making new mutations to the internal loop.

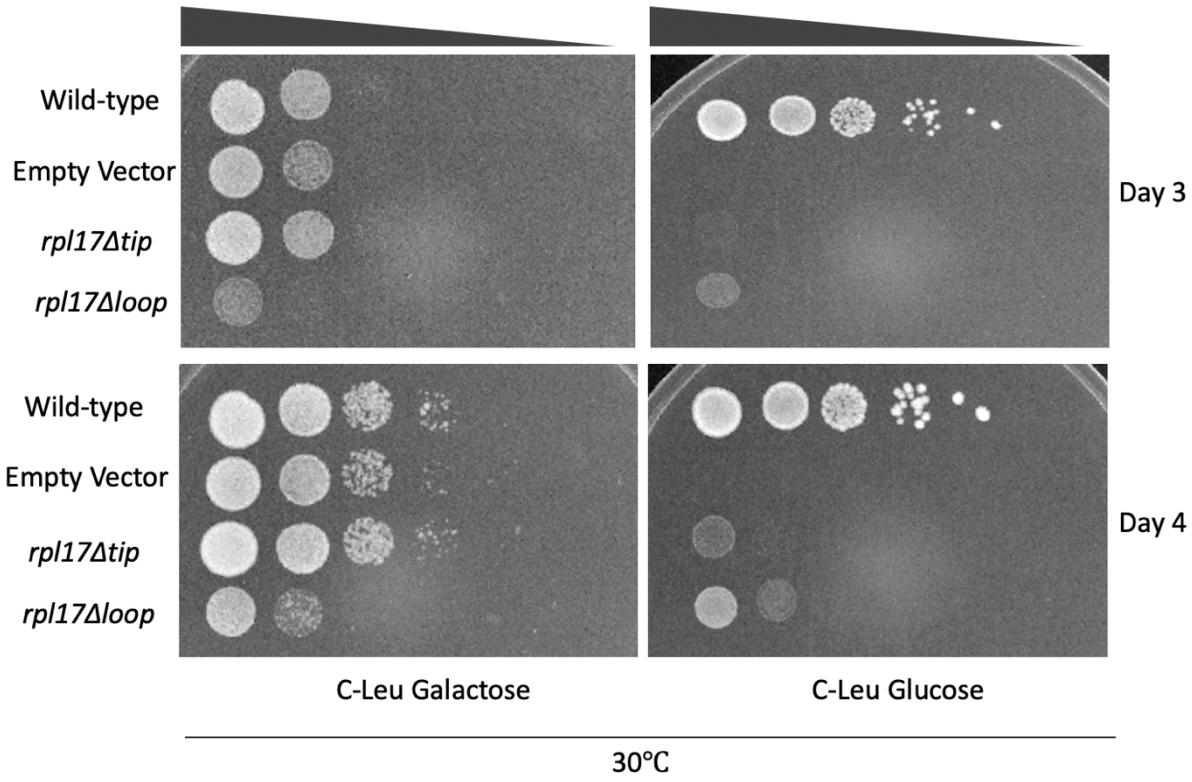

Figure 0.1. Growth assay of rpl17 internal loop mutations.

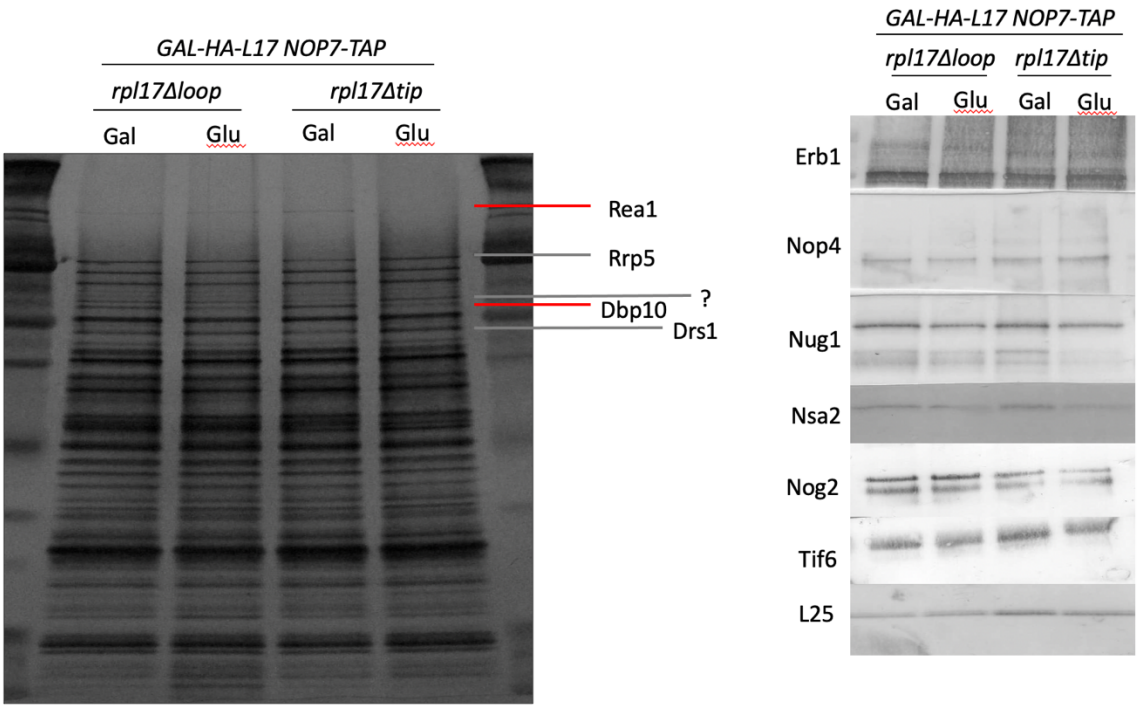

Figure 0.2. Purification of Nop7-associated pre-ribosomal particles from rpl17 loop mutants.

SDS-PAGE silver stained gel displaying purifications of Nop7 particles from respective *rpl17* loop mutants. Bands corresponding to assembly factors that appear to change relative to wild-type are labeled (left). Western blot assays (right) measuring levels of specific assembly factors or ribosomal proteins present in the same samples displayed in the SDS-PAGE gel.

Part 2: L39 may be facilitate insertion of the Nog1 CTD into the NPET

Toward the end of my work with the L4 TD and the Nog1 CTD, Jesus De La Cruz sent us his *rpl39*Δ *NOG2-TAP* strain that his lab had been working on for a few years. It had already been revealed that L39 was not essential for cell growth and that knockout mutants exhibited a cold-sensitive growth defect (Li et al., 2014; Steffen et al., 2012). Jesus De La Cruz's lab was able to demonstrate that this cold-sensitive growth defect was associated with ribosome assembly defects, including an accumulation of 27SB and 7S pre-rRNA and halfmer polyribosomes. I was able to replicate these halfmer polyribosome findings and the cold-sensitive growth defect (**Figure 3.3**). Our role in this collaboration was to use this strain to assay the Nog2-associated particles from this mutant using and add silver staining, western blotting, and iTRAQ mass-spectrometry data to an eventual publication.

3.1.2 Silver staining of *rpl39*Δ *NOG2-TAP* mutants reveals a pattern nearly identical to that observed in the triple tail mutant

It was immediately apparent that the *rpl39*Δ mutant displayed a defect similar to the triple tail and *nog1*Δ*C* mutant strains. In addition to the cold-sensitive growth phenotype, the pattern observed on silver stained SDS-PAGE gels following purification of Nog2-associated particles from the *rpl39*Δ mutant resembled that of the tripe tail mutant (**Figure 3.4**). Specifically, we see a decrease in bands corresponding to Rea1,

Arx1, and possibly Ipi1 and Ipi3. Even the slight increase in Nug1 observed in the triple tail mutant is replicated in this gel. Although this set of data is not exhaustive, its implications enabled me to make an interesting hypothesis. In Chapter 2, I explained how the Nog1 CTD is necessary for recruitment of the AF Arx1 to the exit tunnel platform. The similarities between the *rpl39*Δ and triple tail mutant, especially the absence of Arx1, suggests that the Nog1 CTD fails to enter the NPET without L39. Further verification of these silver stained SDS-PAGE results was pursued further with iTRAQ mass-spectrometry experiments but have been unsuccessful as the time of writing this thesis.

Initially, these observations, combined with the fact that L39 and the Nog1 CTD appeared to become visible in the NPET at the same time in Nog2 state 1, led me to suggest that L39 helps chaperone the Nog1 CTD into the NPET. I know that it cannot be the other way around (Nog1 helping L39 enter the NPET), because density for L39 can clearly be seen in classes N1-N4 of the triple tail mutant, in which the Nog1 CTD has been truncated (Wilson et al., 2020). Therefore, measuring the defects of an *rpl39*Δ mutant could have been just another measurement of what happens in the absence of the Nog1 CTD. However, as briefly discussed in Chapter 1, thanks to conversations between our lab and Sebastian Klinge, we now know that densities for L39 are in fact visible in the cryo-EM dataset for states NE1 and NE2, while density for the Nog1 CTD remains invisible until Nog2 state 1. This means that L39 does not load the Nog1 CTD into the NPET as it assembles into the pre-60S ribosomal subunit, but it does not rule out the possibility that L39 is helps stabilize the Nog1 CTD in the NPET. Based on the data described above, this still seems to be the case even though the situation may be more complicated than originally thought.

Remaining questions for the *rpl39*Δ mutant include: **1)** Is L39 necessary for the stabilization of the Nog1 CTD in the NPET? **2)** Can we understand the mechanism of this relationship? **3)** Are there other effects that distinguish the defects of an *rpl39*Δ mutant from those of the triple tail mutant? Due to difficulties in sending purified samples to the Gao lab Beijing for reasons pertaining to the COVID-19 pandemic, Jelena has sent the *rpl39*Δ *NOG2-TAP* mutant, among other strains, directly to the Gao lab so that they can grow the cells for the purpose of cryo-EM analysis. These experiments will be instrumental in providing answers to any remaining questions regarding the proteins involved in NPET assembly.

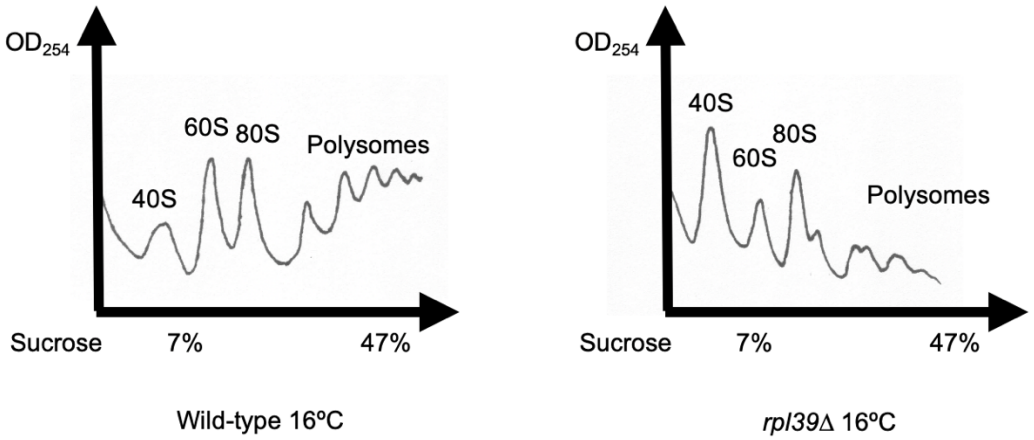

Figure 0.3*. rpl39*Δ exhibits 60S ribosomal subunit deficiencies.

Sucrose gradient fractionation of wild-type and *rpl39*Δ cells shifted to 16ºC for 5 h.

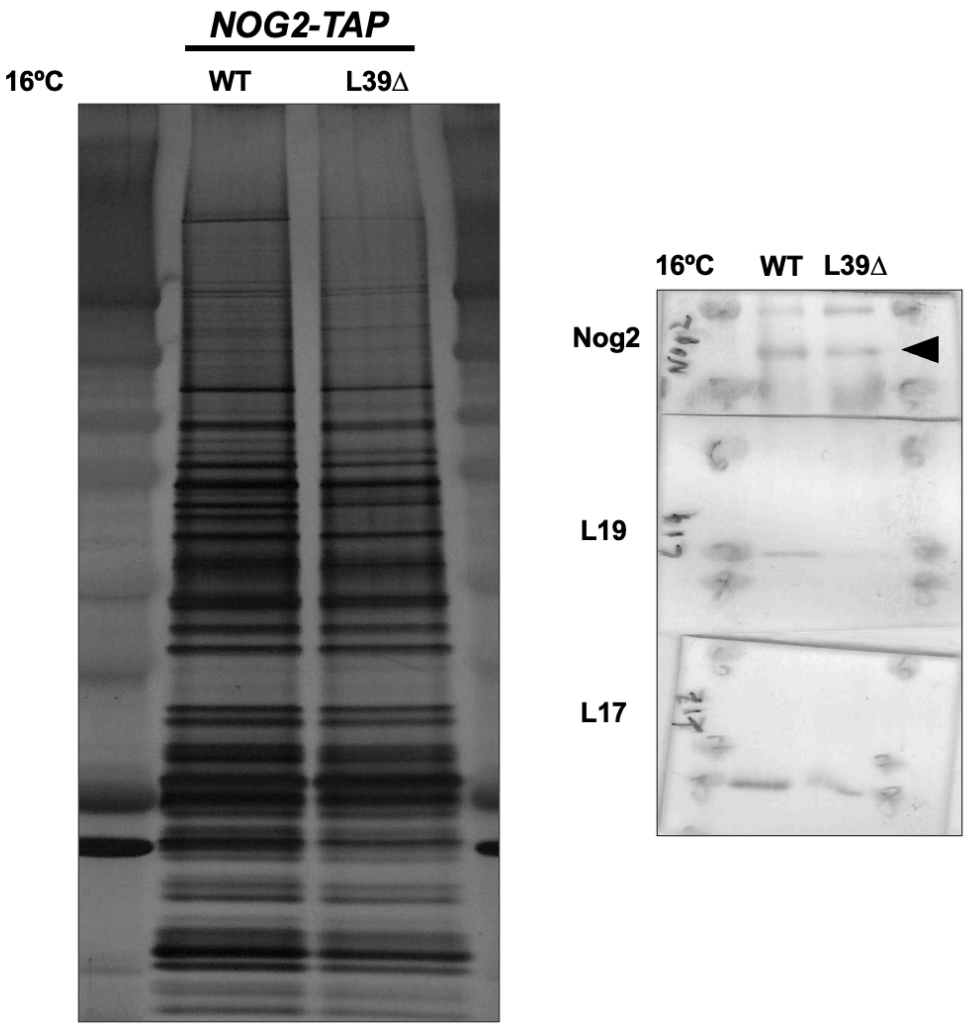

Figure 0.4. Defects caused by rpl39Δ resemble those observed in nog1 C-terminal truncations.

SDS-PAGE silver stain of purified Nog2-associated pre-ribosomal particles and western blot analysis of the same samples.

Part 3: L8 and the 3-way junction of rRNA helices 75, 76, and 79

After we had analyzed our cryo-EM datasets for the *rpl4Δ63-87* and triple tail mutants and built or model about how the L4 TD and Nog1 CTD ultimately function to help stabilize rRNA, we began to look back at the *rpl8Δ1-70* mutant that Beril Tutuncuoglu had previously worked with (Tutuncuoglu et al., 2016). Beril had discovered that the deletion of the N-terminal extension of the RP L8 resulted in a failure of pre-60S ribosomal particles to assemble Sda1, Rea1, and the Rix1 complex, accumulation of the AFs Rpf2, Rrs1, and Rsa4, accumulation of 27SB and 7S pre-rRNA, and, presumably, failure to export pre-60S ribosomal subunits from the nucleoplasm. This pattern of defects is strikingly similar to those observed with the *rpl4Δ63-87* and *rpf2ΔC* mutants (Micic et al., 2020; Wilson et al., 2020).

At first glance, this may not make much sense, as the mutated portions of each of these three proteins bind to very different regions of the pre-ribosome (Wu et al., 2016). However, while observing and analyzing my mutant cryo-EM structures, I came up with a model that includes an explanation for the defect observed with the *rpl8Δ1-70* mutant. It was first observed in Nog2 state 1 that the N-terminus of L8 snakes through rRNA expansion segment 31, which is part of rRNA helix 79 (Wu et al., 2016). In addition to the *rpl8Δ1-70* mutant, Beril also generated and assayed a *rpl8Δ1-52* mutant. Importantly, the *rpl8Δ1-70* mutant resulted in lethality while the *rpl8Δ1-52* mutant did not (Tutuncuoglu et al., 2016). This is a crucial distinction because the stretch of residues 52-70 come into close contact with the junction of the H75, H76, and H79 3-way junction. This suggest that the common defect between the *rpl4Δ63-87*, *rpl8Δ1-70*, and

*rpf2*Δ*C* mutants comes down to a failure to stabilize this 3-way junction, resulting in helices 75 and 68 adopting the aberrant conformations discussed in Chapter 2 that prevent assembly of Sda1 into pre-60S ribosomal subunits (*rpf2*Δ*C* more directly effects helices 68 and 69 rather than the 3-way junction but the junction is also observed to be misassembled in the *rpf2*Δ*C* mutant structures) (Micic et al., 2020).

One striking difference separating the *rpl8*Δ*1-70* mutant from the *rpl4*Δ*63-87* and *rpf2*Δ*C* mutants is the apparent accumulation of a band corresponding to the AFs Spb1 and/or Erb1 evident on silver stained SDS-PAGE gels (**Figure 3.5**). In states E and NE1, the C-terminal tail of Spb1 binds the pre-60S ribosomal subunit in close proximity to the N-terminus of L8 and is replaced by the 3-way junction of rRNA H75, H76, and H79 once Spb1 dissociates from the pre-60S subunit in state NE2 (**Figure 3.6**). These biochemical and structural observations suggest to me that the N-terminus of L8 might help stabilize position the 3-way junction of rRNA such that it competes with and displaces Spb1, thus assisting in its removal from the pre-60S subunit.

In order to test these hypotheses, I set out to obtain cryo-EM structures of *rpl8*Δ*1-70* mutant pre-ribosomes by purifying pre-60S ribosomal subunits, again using the AF Nog2 as bait. Just before the COVID-19 lockdowns occurred in March of 2020, I had grown the 20 liters of cells required for this experiment and successfully purified pre-ribosomes from each sample (**Figure 3.7**). The samples are currently being stored at -80ºC. However, it is uncertain whether it is possible to ship them to Beijing in a timely manner, so as to avoid thawing, given the restrictions and global situation with COVID-19. Out of an abundance of caution, we have decided that these samples will remain stored until they can be shipped or analyzed by another group. This work will offer definitive answers to remaining questions surrounding how three very different mutants

all cause such a similar defect when assayed by our conventional biochemical techniques. It may also fuel new hypotheses that warrant additional, more precise mutations to the N-terminus of L8. Finally, it may reproduce the finding made in class R1 of the *rpl4Δ63-87* mutant that the internal loop of L15 is flexible when H75 is flexible (**Figure 2.10**). Reproducing this result would add precedence to studying mutations of the internal loop of L15 in order to determine whether or not it could contribute to this step in 60S ribosomal subunit assembly or if the observed flexibility is just an insignificant side-effect of the displacement of H75. Overall, cryo-EM of the *rpl8Δ1-70* mutant could offer new insight into construction of the L1 stalk and form the basis for future thesis projects.

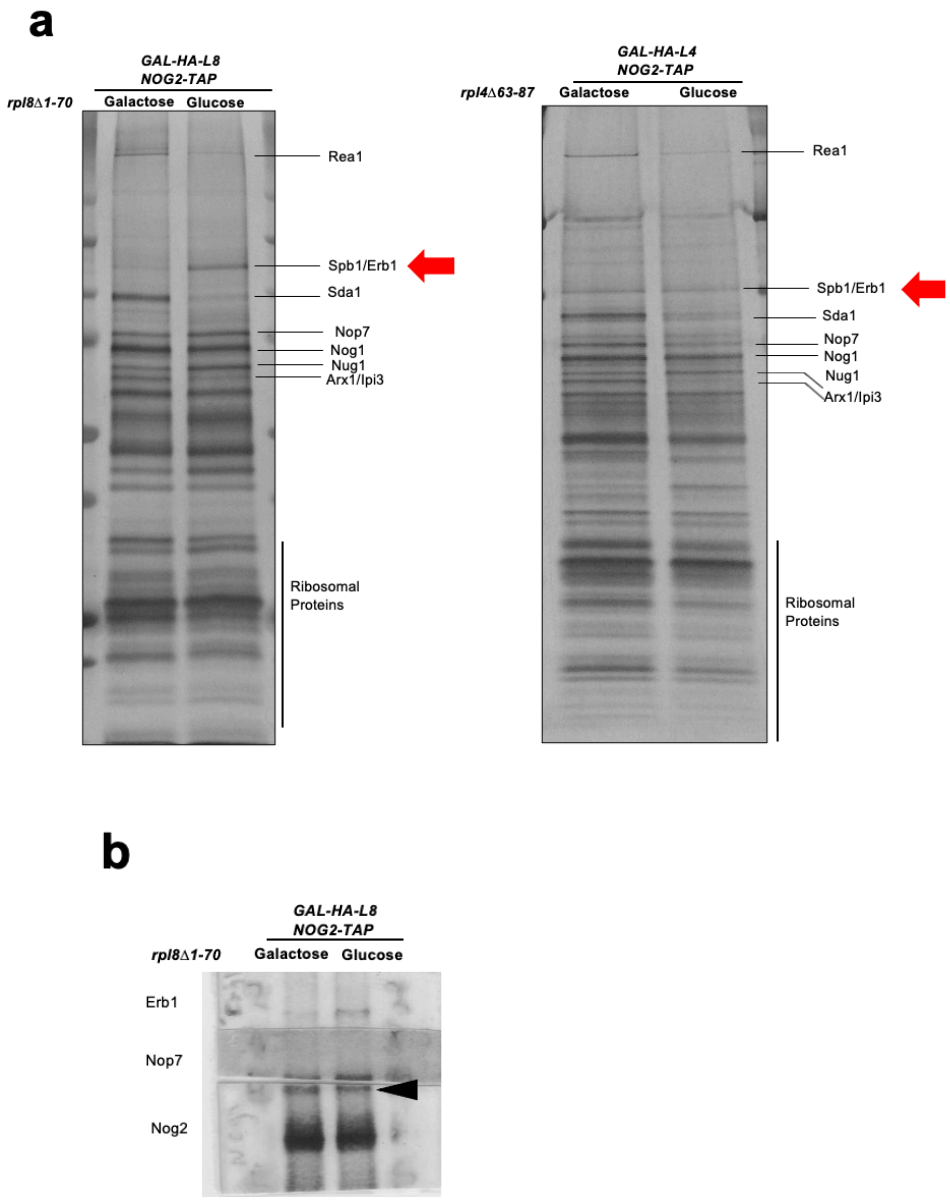

Figure 0.5. Nog2-associated particles purified from the *rpl8Δ1-70* closely resemble those observed purified from the *rpl4Δ63-87* mutant.

(a) Comparison of SDS-PAGE silver stain gels showing purified Nog2-associated particles form *rpl8Δ1-70* or *rpl4Δ63-87* mutants. **(b)** Western blot analysis of select proteins present in Nog2-associated particles purified from the *rpl8Δ1-70* mutant.

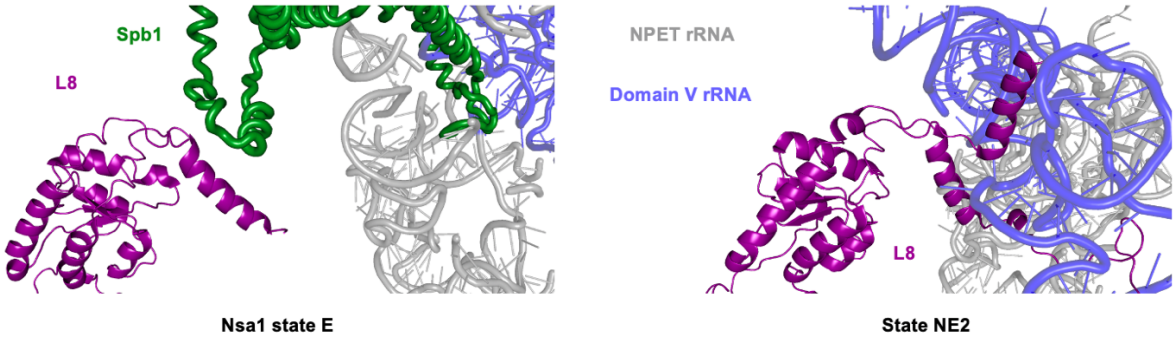

Figure 0.6. The 3-way junction of rRNA helices 75, 76, and 79 appear to displace Spb1.

PyMol structures showing cryo-EM reconstructions of Nsa1 state E (6ELZ) and state NE2 (6YLY). Most of the N-terminus of L8 (purple) remains invisible until the 3-way junction of rRNA helices 75, 76, and 79 (blue) anchor into their mature position, which appears to displace Spb1 (green).

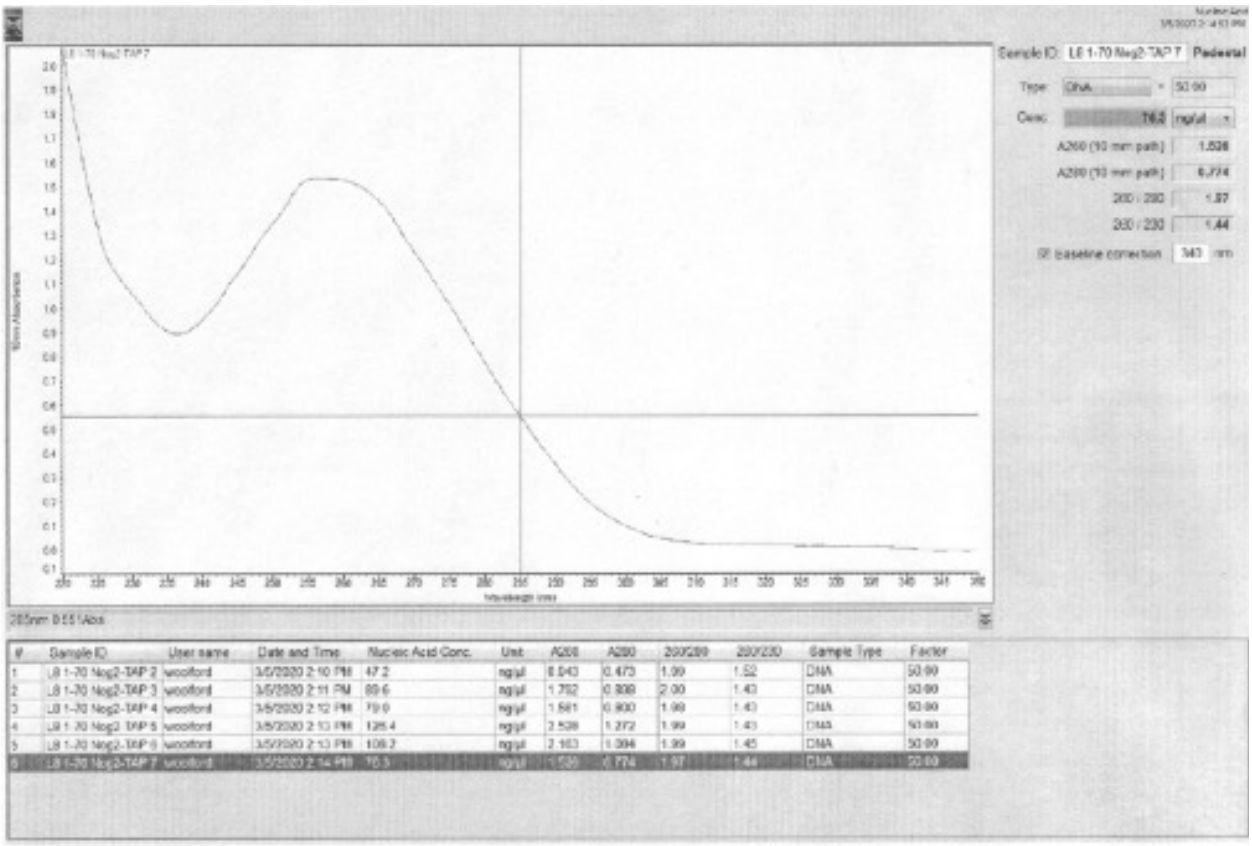

Figure 0.7. **Absorbance spectra of *rpl8*Δ*1-70* Nog2-TAP purifications for cryo-EM**.

These spectra are representative of what to expect when testing the quality of purified samples destined for cryo-EM.

Part 4: Exploring the effects of rapamycin on ribosome assembly

Ribosome assembly is the most energetically expensive pathway in the cell and is intertwined with several energy-sensing pathways (Baßler and Hurt, 2019; Kos-braun et al., 2017). Logically, this means that ribosome assembly is subject to many forms of regulation in response to the availability of nutrients. For example, inactivation of target of rapamycin (TOR) results in decreased transcription of ribosomal DNA (rDNA) genes and traps pre-60S ribosomal subunits in the nucleolus (Honma et al., 2006; Huber et al., 2009; Vanrobays et al., 2008). Jason Talkish in our lab was curious how different stressors, including exposure to the drug rapamycin, might affect ribosome assembly.

For his rapamycin experiments, Jason incubated yeast cells in the presence of rapamycin and assayed the composition of Nop7-associated pre-60S ribosomal subunits using SDS-PAGE silver staining and western blotting. He found that Nog2 failed to assemble into pre-ribosomes more often after 2 h in rapamycin-containing rich media (Talkish et al., 2012). These results are consistent with pre-60S subunits being trapped in the nucleolus under these conditions. However, the question of how these pre-ribosomes remain trapped in the nucleolus and what the particles look like remained unanswered.

4.1.1 *NSA2-TAP* as a tool to study how rapamycin traps pre-ribosomes in the nucleolus

In order to begin answering this question, I revisited Jason's data. As described in previous chapters, Nop7 is an extremely useful bait protein for initial studies of mutants or for studying B-mutants. Ideally, one would use a bait protein that represents a more discrete window of ribosome assembly when Nop7 fails to yield sufficient answers to questions. Among the proteins that did not decrease from Nop7-asociated particles following incubation with rapamycin was the AF Nsa2 (Talkish et al., 2012).

Nsa2 first becomes visible in cryo-EM structures in state C, whereas Nop7 assembles at an earlier, as of yet unspecified point in assembly (Kater et al., 2017). In the past, Nsa2 had not usually been used as a bait protein to purify pre-ribosomes. However, an *NSA2-TAP* strain existed in the yeast TAP library collection. My attempt to purify Nsa2-associated pre-60S ribosomal subunits were successful (**Figure 3.8**), meaning that I could pursue using it as a tool to follow up on Jason's experiments. The following work was done with the help of an undergraduate mentee, Yoonju Pak.

4.1.2 The composition of Nsa2-associated pre-60S ribosomal subunits changes following incubation with rapamycin

Since I was able to purify Nsa2-associated pre-ribosomes from cells under both wild-type and rapamycin conditions, the next step was to characterize the relevant bands that changed between each sample. In order to do this, I cut bands out from a silver stained SDS-PAGE gel and sent them off for mass-spectrometry. I was able to

unambiguously identify most bands of interest (**Figure 3.8**). Interestingly, a band that remains unidentified but corresponds to Dbp10 on an silver stained SDS-PAGE gel displaying Nop7-associated pre-ribosomes (Biedka et al., 2018) appears to accumulate upon repression of TOR (**Figure 3.8**).

These experiments fall short due to the fact that they are not quantifiable or comprehensive. The next experiment would have been to address these shortcomings using iTRAQ mass-spectrometry. However, COVID-19 lockdowns interrupted these plans. Using these Nsa2-associated particles to further investigate the effects of TOR repression on ribosome assembly could help clarify the signals required to restrict or release pre-ribosomes from the nucleolus. Examining the composition, or even the structure, of these particles in greater detail could also help test the model of pre-ribosome release from the nucleolus that Amber LaPeruta has been building in previous months.

4.1.3 Microscopy of GFP-tagged assembly factors in response to TOR repression

Microscopy was another approach that I took to study ribosome assembly in response to TOR repression via rapamycin. These experiments simply utilized strains from the GFP yeast collection library. I grew a selection of strains from this library expressing different GFP-tagged AFs or RPs whose subcellular localization might change upon repression of TOR. I reasoned that assembly factors such as Nog1, whose steady-state GFP signal corresponds to the nucleoplasm, may shift to primarily nucleolar when cells are incubated with rapamycin. Previous studies have observed this

phenomenon and an initial step would be to replicate these findings in my hands (Honma et al., 2006).

Unfortunately, none of the GFP signals appeared to obviously change in any strain observed following incubation with rapamycin, with the possible exception of Nop4 (**Figure 3.9**). Follow up experiments were planned to involve additional markers for the nucleoplasm or the nucleolus. This would add context to the GFP signal and enable me to observe whether or not the GFP signal changes in relation to a static, defined marker. The plans were interrupted by the COVID-19 lockdowns and this side project was not picked up upon returning to lab. However, this approach holds potential value for determining which nucleoplasmic-acting AFs might fail to assemble or become trapped on pre-60S ribosomal subunits upon TOR repression. These experiments repeated with other stressors known to affect ribosome assembly such as oxidative stress, cold/heat shock, and nutrient depravation could be useful first steps in uncovering mechanisms that tie ribosome assembly to major regulatory pathways in the cell and how pre-ribosomes leave the nucleolus.

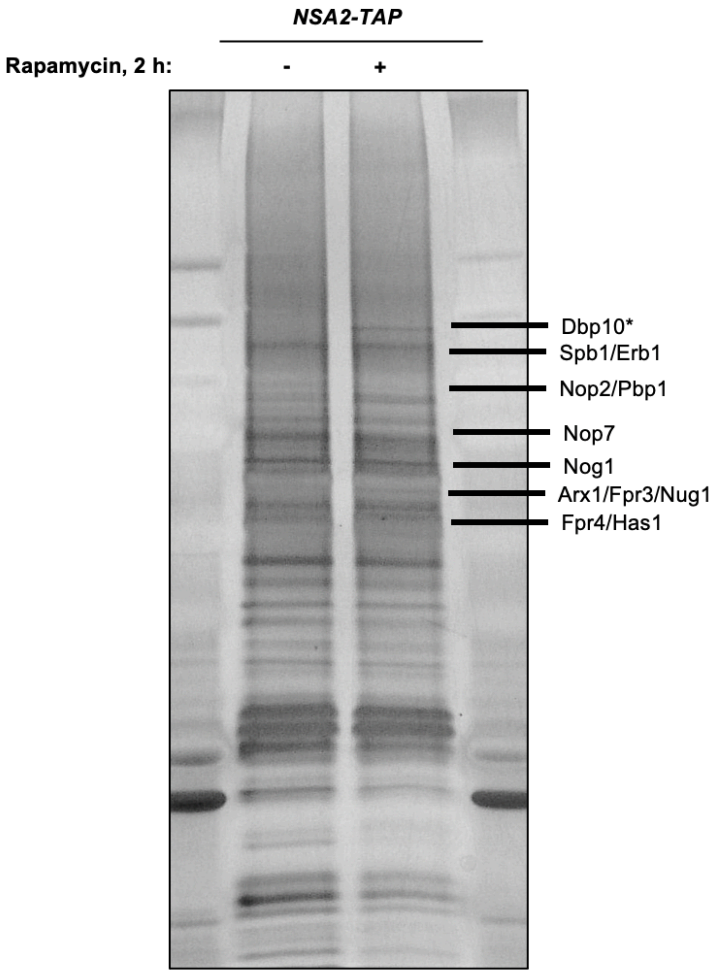

Figure 0.8. **Rapamycin changes the composition of Nsa2-associated pre-ribosomal particles**.

SDS-PAGE silver stained gel showing the changes in protein composition of Nsa2-associated pre-ribosomes upon incubation with rapamycin. Proteins identified with mass-spectrometry are labeled. Dbp10 was identified here based on previous mass-spectrometry experiments.

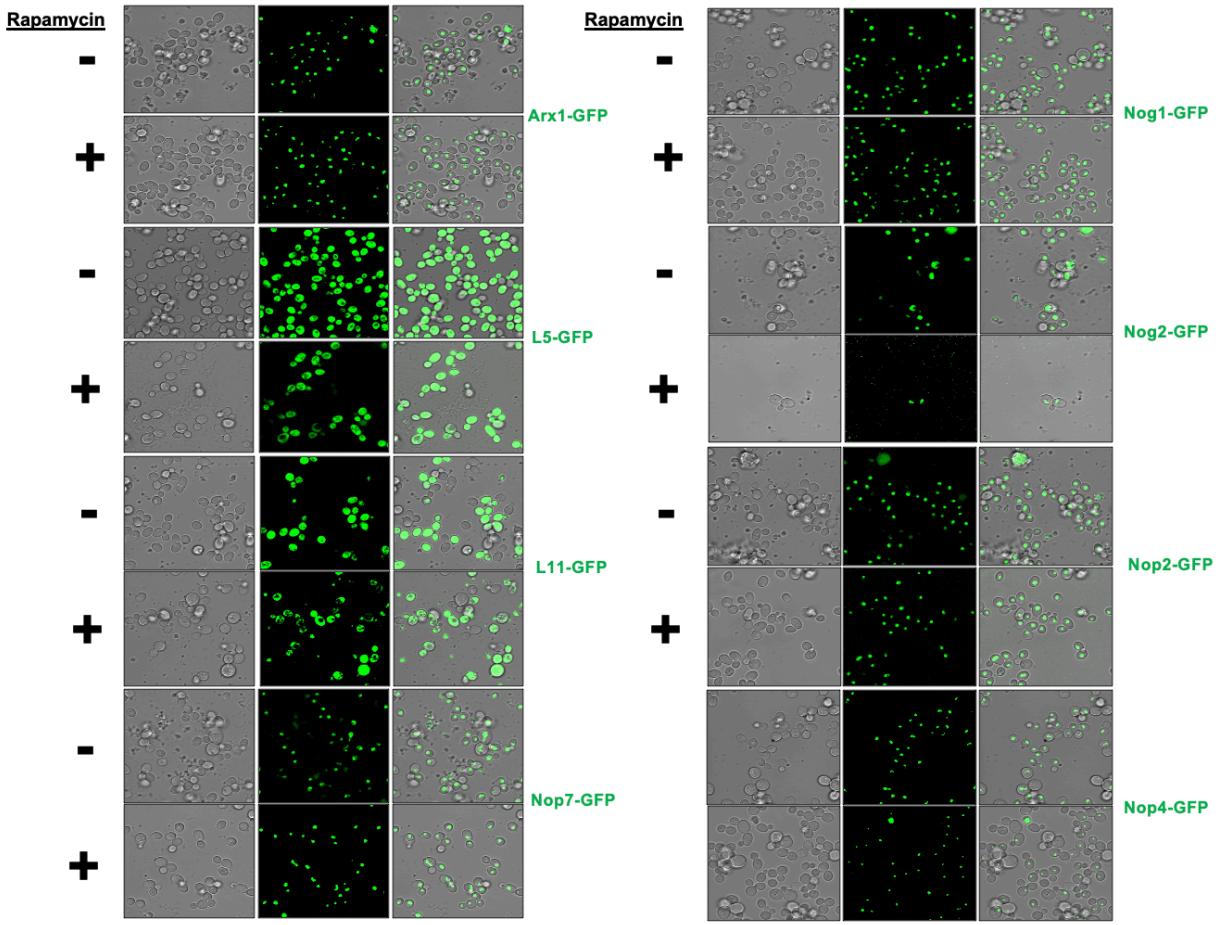

Figure 0.9. Effect of rapamycin on the localization of ribosomal proteins and assembly factors.

Confocal images of cells expressing GFP-tagged ribosomal proteins or assembly factors.

FUTURE DIRECTIONS

Lingering questions concerning tunnel construction

Although I was able to discern a function for the C-terminal domain extension of Nog1, no function has been ascribed to the tunnel-inclusive C-terminal extensions of Rei1 and Reh1. To be clear, the portion of the C-terminal domain of Rei1 outside of the tunnel, where Arx1 binds, is necessary for the removal of Arx1(Greber et al., 2016; Hung and Johnson, 2006). However, this does not offer a satisfactory explanation as to what function the amino acids that reach into the NPET might perform. One might suggest that the length occupying the NPET helps Rei1 anchor onto the pre-60S subunit and facilitate its function to remove Arx1. However, truncations of the Rei1 C-terminal mutations seem to cause ribosome assembly defects only when the Arx1 binding site is affected (Greber et al., 2016). Meanwhile, Reh1 is nonessential for yeast growth and ribosome assembly (Parnell and Bass, 2009). Therefore, it remains unclear whether or not the C-terminal extensions of Rei1 or Reh1 play a role in NPET assembly. Further investigation of the effects of Rei1 or Reh1 mutants on ribosome assembly pathway are, in my opinion, unlikely to yield answers to this question. The reason for this is that cryo-EM would likely be required in order to reach a final answer, which is a high-risk, high-cost approach to a question that may not yield exciting answers. Instead, a more attractive hypothesis is that mutations in the C-terminal extensions of Nog1, Rei1, or Reh1 may make ribosomes more prone to errors in translation. It would be possible to test this hypothesis using a low-cost ribosome stalling reporter system developed by the Sachs lab (Gaba et al., 2005) or a high-cost ribosome profiling experiment (Ingolia,

2014). Perhaps these experiments will one day offer more insight into why these C-terminal extensions occupy the NPET and warrant more investigation into any functions they may perform during assembly.

Aside from these C-terminal extensions, the function of multiple AFs in NPET construction remain incompletely investigated. Early acting AFs such as Rrp14, Rpf1, and Spb1 remain uninvestigated in the context of NPET construction. A classic mutagenesis followed by ribosome assembly assays approach could be an effective approach in answering these lingering questions concerning the early stages of NPET assembly.

Further investigation of the H75, 76, and 79 rRNA 3-way junction using ribosomal proteins L8 and L15

The revelation that the rRNA 3-way junction of helices 75, 76, and 79 play an important role in middle stages of ribosome assembly (including NPET construction, 5S RNP rotation, and proper positioning of the L1 stalk) motivated revisiting of ribosomal proteins that interact with these helices. As discussed in Chapters 2 and 3, the cryo-EM structure of class R1 from *rpl4Δ63-87* revealed that, in addition to the 3-way junction being disrupted, the N-terminal extension of L8 and internal loop of L15 were observed to be flexible. Additionally, Beril Tutuncuoglu showed that deletion of this N-terminal extension of L8 results in blocks in 60S subunit assembly that indicate a strong defect in 5S RNP rotation (Tutuncuoglu et al., 2016). I have purified enough Nog2-associated pre-60S subunits from Beril's *rpl8Δ1-70* mutant in order to do cryo-EM. These samples currently cannot be sent to the Gao lab in Beijing due to the COVID-19 pandemic. Either

new collaborators will need to be found who can examine these samples or the lab will have to wait to see what answers they may hold. In the meantime, mutations to the internal loop of L15 could be made and assayed for ribosome assembly defects. Although, a plasmid containing the gene for L15 has proven difficult to make in the past (Jelena Micic, personal communication). Despite this, newer approaches using gateway plasmids or enlisting the help of a company could make progress on this front. If successful, mutations of the internal loop of L15 could be assayed for ribosome assembly defects that may be consistent with those observed in the *rpl4*Δ*63-87*, *rpl8*Δ*1-70*, and *rpf2*Δ*C* mutants. These experiments could be published in a short-medium sized story and offer a more complete picture of construction of the L1 stalk.

Next steps in determining how TOR repression traps pre-ribosomes in the nucleolus

The molecular mechanisms of how ribosomes are retained in the nucleolus remain experimentally unverified. Amber LaPeruta in the lab has developed an in-depth model to describe how nucleolar retention and release occurs in ribosome assembly. Clearly, this process taken advantage of under conditions of stress or repression of TOR in order to halt the energetically expensive process of ribosomes assembly (Honma et al., 2006; Vanrobays et al., 2008). Rapamycin is a drug that quickly inactivates TOR and halts ribosome assembly, retaining pre-ribosomes in the nucleolus. Therefore, studying pre-ribosomes trapped in the nucleolus due to TOR repression could be a valuable tool in experimentally testing this model. I have been able to determine that Nsa2 is likely the best AF to use as bait in purifying and studying pre-60S particles in this context. The

best next step would be to study the composition of these stalled particles in detail using iTRAQ mass-spectrometry. We might expect to find pre-60S particles harboring many AFs enriched for intrinsically disordered domains (IDRs) or AFs that are expected to keep rRNA domains IV and V in an undocked conformation (see Amber LaPeruta's model). Such biochemical analysis combined with 2-color microscopy of AFs following TOR repression could be some of the first experimental evidence to directly test a model of nucleolar retention of pre-60S subunits.

CONCLUSION

The work discussed in this dissertation mostly describes my studies of RP's and AF's with a focus on how these proteins fold and position rRNA into functional centers, particularly the NPET. My findings and remaining hypotheses surrounding Nog1, L4, L8, and L39 all form a convergence around a common set of rRNA helices, H74-79 and H68-69. Specifically, these helices appear to form a central hub capable of allosteric communication with multiple functional centers. Therefore, defects in construction of a functional center such as the NPET can propagate changes in rRNA conformation to other domains, which ultimately inhibits downstream steps in ribosome assembly. This work highlights the importance of rRNA folding in assembly of ribosomal subunits and reveals new principles that can be explored further.

Studying rRNA folding in ribosome assembly has traditionally been difficult to study in great detail and thus has stood as sort of a black box in our knowledge of the mechanistic functions of RP's and AF's. The findings of my work were made possible only because we took advantage of the quickly growing field of cryo-EM, which enables us to visualize each stably incorporated nucleotide of the ribosome all at once, something no other experiment can currently offer. Our field is transitioning to one that relies equally on molecular and structural biology techniques (Klinge and Woolford, 2019).

As the number of wild-type and mutant cryo-EM particles continues to grow, so will our understanding of the ribosome assembly pathway. Currently, most cryo-EM studies of ribosome assembly do not include in-depth biological analyses of specific hypotheses. Our lab was the first to do this in studies of the yeast large ribosomal

subunit (Micic et al., 2020; Wilson et al., 2020) and the field will need to begin doing the same. Structural observations alone are not sufficient to make confident conclusions concerning mechanisms in ribosome assembly. For example, many have stated that the C-terminal tails of AFs such as Nog1, Rei1, and Reh1 perform quality control checks on the NPET during assembly of the large ribosomal subunit (Greber, 2016; Greber et al., 2016; Klingauf-Nerurkar et al., 2020; Peña et al., 2017). However, my work exploring the biological significance of these C-terminal tails offers a much more complete and modest interpretation of that otherwise would not be evident from structural observations alone. Meanwhile, nobody predicted that deletion of the L4 TD would have resulted in the much more interesting defects that I observed (Wilson et al., 2020).

Every project in our lab now includes a plan to obtain cryo-EM structures of pre-60S ribosomal subunits purified from at least one mutant. In an overflow of structural observations and possible hypotheses to test, the biggest limiting factor in achieving successful studies lies in choosing the “correct” mutant(s) to assay. Our lab has already seen that structural observations may be misleading and motivate generation of mutations that end up causing no significant or discernible defects. Persistence and diligent study of cryo-EM structures will be key to overcoming these challenges.

As my work shows, the field of ribosome assembly is now poised to answer questions in levels of detail that were hard to imagine less than a decade ago. Even more exciting, cryo-EM technology will continue to improve and staying up to date with these improvements will also be key to breaking new boundaries. If my last 4.5 years in the Woolford lab are any indication of how fast progress is being made in this field, the next 5 years will truly be fascinating to observe.

REFERENCES

Adams, P.D., Pavel, V., Chen, V.B., Ian, W., Echols, N., Moriarty, N.W., Read, R.J., Richardson, D.C., Jane, S., Thomas, C., 2010. PHENIX : a comprehensive Python-based system for macromolecular structure solution. Biol. Crystallogr. 213–221.

Afonine, P. V, Ralf, W., Headd, J.J., Thomas, C., 2012. Towards automated crystallographic structure refinement with phenix.refine. Biol. Crystallogr. 352–367.

Amunts, A., Brown, A., Bai, X., Llácer, J.L., Hussain, T., 2014. Structure of the Yeast Mitochondrial Large Ribosomal Subunit. Science (80-.). 343, 1485–1489.

Barrio-Garcia, C., Thoms, M., Flemming, D., Kater, L., Berninghausen, O., Baßler, J., Beckmann, R., Hurt, E., 2015. Architecture of the Rix1 – Rea1 checkpoint machinery during pre-60S-ribosome remodeling. Nat. Struct. Mol. Biol. 23, 37–44.

Baßler, J., Hurt, E., 2019. Eukaryotic Ribosome Assembly. Annu. Rev. Biochem. 88, 281–306.

Biedka, S., Micic, J., Wilson, D., Brown, H., Diorio-Toth, L., Woolford, J.L., 2018. Hierarchical recruitment of ribosomal proteins and assembly factors remodels nucleolar pre-60S ribosomes. J. Cell Biol. 217, 2503–2518.

Biedka, S., Wu, S., Laperuta, A.J., Gao, N., Woolford, J.L., 2017. Insights into remodeling events during eukaryotic large ribosomal subunit assembly provided by high resolution cryo-EM structures. RNA Biol. 6286.

Brar, G.A., Weissman, J.S., 2015. Ribosome profiling reveals the what, when, where and how of protein synthesis. Nat. Rev. Mol. Cell Biol. 16, 651–664.

Chen, V.B., Bryan, W., Iii, A., Headd, J.J., Keedy, D.A., Robert, M., Kapral, G.J., Murray, L.W., Jane, S., David, C., 2010. MolProbity: all-atom structure validation for

macromolecular crystallography. Acta Crystallogr. Sect. D 66, 12–21.

Chittum, H.S., Champney, W.S., 1994. Ribosomal protein gene sequence changes in erythromycin-resistant mutants of Escherichia coli. J. Bacteriol. 176, 6192–6198.

Chursov, A., Kopetzky, S.J., Bocharov, G., Frishman, D., Shneider, A., 2013. RNAtips : analysis of temperature-induced changes of RNA secondary structure. Nucleic Acids Res. 41, 486–491.

Dao Duc, K., Batra, S.S., Bhattacharya, N., Cate, J.H.D., Song, Y.S., 2019. Differences in the path to exit the ribosome across the three domains of life. Nucleic Acids Res. 47, 4198–4210.

Davis, A.R., Gohara, D.W., Yap, M.N.F., 2014. Sequence selectivity of macrolide-induced translational attenuation. Proc. Natl. Acad. Sci. U. S. A. 111, 15379–15384.

Deshmukh, M., Tsay, Y., Paulovich, A.G., Woolford, J.L., 1993. Yeast Ribosomal Protein Li Is Required for the Stability of Newly Synthesized 5S rRNA and the Assembly of 60S Ribosomal Subunits. Mol. Cell. Biol. 13, 2835–2845.

Dontsova, O.A., Dinman, J.D., 2005. 5S rRNA : Structure and Function from Head to Toe. Int. J. Biomed. Sci. 1, 1–7.

Duss, O., Stepanyuk, G.A., Puglisi, J.D., Williamson, J.R., Duss, O., Stepanyuk, G.A., Puglisi, J.D., Williamson, J.R., 2019. Transient Protein-RNA Interactions Guide Nascent Ribosomal RNA Folding. Cell 179, 1357–1369.

Emsley, P., Lohkamp, B., 2010. Features and development of Coot. Biol. Crystallogr. 486–501.

Feng, B., Mandava, C.S., Guo, Q., Wang, J., Cao, W., Li, N., Zhang, Yixiao, Zhang, Yanqing, Wang, Z., Wu, J., Sanyal, S., Lei, J., Gao, N., 2014. Structural and Functional Insights into the Mode of Action of a Universally Conserved Obg

GTPase. PLoS Biol. 12, 1–14.

Frottin, F., Schueder, F., Tiwary, S., Gupta, R., Korner, R., Schlichthaerle, T., Cox, J., Jungmann, R., Hartl, F., Hipp, M., 2019. The nucleolus functions as a phase-separated protein quality control compartment. Science (80-.). 365, 1–6.

Fuentes, J.L., Datta, K., Sullivan, S.M., Walker, A., Maddock, J.R., 2007. In vivo functional characterization of the Saccharomyces cerevisiae 60S biogenesis GTPase Nog1. Mol. Genet. Genomics 278, 105–123.

Gaba, A., Jacobson, A., Sachs, M.S., 2005. Ribosome occupancy of the yeast CPA1 upstream open reading frame termination codon modulates nonsense-mediated mRNA decay. Mol. Cell 20, 449–460.

Gagnon, M.G., Roy, R.N., Lomakin, I.B., Florin, T., Mankin, S., Steitz, T.A., 2016. Structures of proline-rich peptides bound to the ribosome reveal a common mechanism of protein synthesis inhibition. Nucleic Acids Res. 44, 2439–2450.

Gamalinda, M., Jakovljevic, J., Babiano, R., Talkish, J., De La Cruz, J., Woolford, J.L., 2013. Yeast polypeptide exit tunnel ribosomal proteins L17, L35 and L37 are necessary to recruit late-assembling factors required for 27SB pre-rRNA processing. Nucleic Acids Res. 41, 1965–1983.

Gamalinda, M., Ohmayer, U., Jakovljevic, J., Kumcuoglu, B., Woolford, J., Mbom, B., Lin, L., Woolford, J.L., 2014. A hierarchical model for assembly of eukaryotic 60S ribosomal subunit domains. Genes Dev. 28, 198–210.

Gamalinda, M., Woolford, J.L., 2014a. Paradigms of ribosome synthesis: Lessons learned from ribosomal proteins. Translation 3, e975018.

Gamalinda, M., Woolford, J.L., 2014b. Deletion of L4 domains reveals insights into the importance of ribosomal protein extensions in eukaryotic ribosome assembly. RNA

20, 1725–31.

Greber, B.J., 2016. Mechanistic insight into eukaryotic 60S ribosomal subunit biogenesis by cryo-electron microscopy. RNA 22, 1643–1662.

Greber, B.J., Boehringer, D., Montellese, C., Ban, N., 2012. Cryo-EM structures of Arx1 and maturation factors Rei1 and Jjj1 bound to the 60S ribosomal subunit. Nat. Struct. Mol. Biol. 19, 1228–33.

Greber, B.J., Gerhardy, S., Leitner, A., Leibundgut, M., Salem, M., Boehringer, D., Leulliot, N., Aebersold, R., Panse, V.G., Ban, N., 2016. Insertion of the Biogenesis Factor Rei1 Probes the Ribosomal Tunnel during 60S Maturation. Cell 164, 91–102.

Grela, P., Szajwaj, M., Horbowicz-Droz˙dz˙al, P., Tchórzewski, M., 2019. How Ricin Damages the Ribosome. Toxins (Basel). 11, 1–16.

Gupta, P., Liu, B., Klepacki, D., Gupta, V., Schulten, K., Mankin, A.S., Vázquez-laslop, N., 2016. Nascent peptide assists the ribosome in recognizing chemically distinct small molecules. Nat. Chem. Biol. 12, 153–159.

Halfon, Y., Matzov, D., Eyal, Z., Bashan, A., Zimmerman, E., Kjeldgaard, J., Ingmer, H., Yonath, A., 2019. Exit tunnel modulation as resistance mechanism of S . aureus erythromycin resistant mutant. Sci. Rep. 1–8.

Harger, J.W., Dinman, J.D., 2003. An in vivo dual-luciferase assay system for studying translational recoding in the yeast Saccharomyces cerevisiae 1019–1024.

Harnpicharnchai, P., Jakovljevic, J., Horsey, E., Miles, T., Roman, J., Rout, M., Meagher, D., Imai, B., Guo, Y., Brame, C.J., Shabanowitz, J., Hunt, D.F., Woolford, J.L., 2001. Composition and functional characterization of yeast 66S ribosome assembly intermediates. Mol. Cell 8, 505–515.

Hedges, J., West, M., Johnson, A.W., 2005. Release of the export adapter , Nmd3p , from and the cytoplasmic GTPase Lsg1p 24, 567–579.

Honma, Y., Kitamura, A., Shioda, R., Maruyama, H., Ozaki, K., Oda, Y., Mini, T., Jenö, P., Maki, Y., Yonezawa, K., Hurt, E., Ueno, M., Uritani, M., Hall, M.N., Ushimaru, T., 2006. TOR regulates late steps of ribosome maturation in the nucleoplasm via Nog1 in response to nutrients. EMBO J. 25, 3832–42.

Huang, S., Aleksashin, N.A., Loveland, A.B., Klepacki, D., Reier, K., Ke, A., Szal, T., Remme, J., Jaeger, L., Vázquez-laslop, N., Korostelev, A.A., Mankin, A.S., 2020. Ribosome engineering reveals the importance of 5S rRNA autonomy for ribosome assembly. Nat. Commun. 11, 1–13.

Huber, A., Bodenmiller, B., Uotila, A., Stahl, M., Wanka, S., Gerrits, B., Aebersold, R., Loewith, R., 2009. Characterization of the rapamycin-sensitive phosphoproteome reveals that Sch9 is a central coordinator of protein synthesis. Genes Dev. 23, 1929–1943.

Hung, N.-J., Johnson, A.W., 2006. Nuclear recycling of the pre-60S ribosomal subunit-associated factor Arx1 depends on Rei1 in Saccharomyces cerevisiae. Mol. Cell. Biol. 26, 3718–3727.

Ingolia, N.T., 2014. Ribosome profiling: new views of translation, from single codons to genome scale. Nat. Publ. Gr. 15, 205–213.

Jakovljevic, J., Ohmayer, U., Gamalinda, M., Talkish, J., Alexander, L., Linnemann, J., Milkereit, P., Woolford, J.L., 2012. Ribosomal proteins L7 and L8 function in concert with six A_3 assembly factors to propagate assembly of domains I and II of 25S rRNA in yeast 60S ribosomal subunits. RNA 18, 1805–1822.

Jenner, L., Melnikov, S., De, N.G., Ben-shem, A., Iskakova, M., Urzhumtsev, A.,

Meskauskas, A., Dinman, J., Yusupova, G., Yusupov, M., 2012. Crystal structure of the 80S yeast ribosome. Curr. Opin. Struct. Biol. 22, 759–767.

Jomaa, A., Jain, N., Davis, J.H., Williamson, J.R., Britton, R.A., Ortega, J., 2014. Functional domains of the 50S subunit mature late in the assembly process. Nucleic Acids Res. 42, 3419–3435.

Kappel, L., Loibl, M., Zisser, G., Klein, I., Fruhmann, G., Gruber, C., Unterweger, S., Rechberger, G., Pertschy, B., Bergler, H., 2008. Rlp24 activates the AAA-ATPase Drg1 to initiate cytoplasmic pre-60S maturation. J. Cell Biol. 199, 771–782.

Kater, L., Mitterer, V., Thoms, M., Cheng, J., Berninghausen, O., Beckmann, R., Hurt, E., Kater, L., Mitterer, V., Thoms, M., Cheng, J., Berninghausen, O., Beckmann, R., 2020. Construction of the Central Protuberance and L1 Stalk during 60S Subunit Biogenesis. Mol. Cell 79, 1–14.

Kater, L., Thoms, M., Barrio-garcia, C., Sinning, I., Hurt, E., Beckmann, R., Kater, L., Thoms, M., Barrio-garcia, C., Cheng, J., Ismail, S., Ahmed, Y.L., 2017. Visualizing the Assembly Pathway of Nucleolar Pre-60S Ribosomes. Cell 171, 1599–1610.

Katunin, V.I., Muth, G.W., Strobel, S.A., Wintermeyer, W., Rodnina, M. V, Haven, N., 2002. Important Contribution to Catalysis of Peptide Bond Formation by a Single Ionizing Group within the Ribosome. Mol. Cell 10, 339–346.

Kemmler, S., Occhipinti, L., Veisu, M., Panse, V.G., 2009. Yvh1 is required for a late maturation step in the 60S biogenesis pathway. J. Cell Biol. 186, 863–880.

Khaitovich, P., Mankin, A.S., Ave, S.A., 1999. Effect of Antibiotics on Large Ribosomal Subunit Assembly Reveals Possible Function of 5 S rRNA. J. Mol. Biol. 291, 1025–1034.

Kitakawa, M., Isono, K., 1991. The mitochondrial ribosomes. Biochimie 73, 813–825.

Klingauf-Nerurkar, P., Gillet, L.C., Portugal-Calisto, D., Oborská-Oplová, M., Jäger, M., Schubert, O.T., Pisano, A., Peña, C., Rao, S., Altvater, M., Chang, Y., Aebersold, R., Panse, V.G., 2020. The GTPase Nog1 co-ordinates the assembly, maturation and quality control of distant ribosomal functional centers. Elife 9, 1–25.

Klinge, S., Woolford, J.L., 2019. Ribosome assembly coming into focus. Nat. Rev. Mol. Cell Biol. 20, 116–131.

Konikkat, S., Biedka, S., Woolford, J.L., 2017. The assembly factor Erb1 functions in multiple remodeling events during 60S ribosomal subunit assembly in S . cerevisiae 1–13.

Koripella, R.K., Sharma, M.R., Bhargava, K., Datta, P.P., Kaushal, P.S., Keshavan, P., Spremulli, L.L., Banavali, N.K., Agrawal, R.K., 2020. Structures of the human mitochondrial ribosome bound to EF-G1 reveal distinct features of mitochondrial translation elongation. Nat. Commun. 11.

Kos-braun, I.C., Jung, I., Kos, M., 2017. Tor1 and CK2 kinases control a switch between alternative ribosome biogenesis pathways in a growth-dependent manner 1.

Kucukelbir, A., Sigworth, F.J., Tagare, H.D., 2014. Quantifying the local resolution of cryo-EM density maps. Nat. Methods 11, 63–65.

Kühlbrandt, W., 2014. The Resolution Revolution. Science (80-.). 343, 1443–1444.

Lapeyre, B., Purushothaman, S.K., 2004. Spb1p-Directed Formation of Gm 2922 in the Ribosome Catalytic Center Occurs at a Late Processing Stage 16, 663–669.

Lawrence, M.G., Shamsuzzaman, M., Kondopaka, M., Pascual, C., Zengel, J.M., Lindahl, L., 2016. The extended loops of ribosomal proteins uL4 and uL22 of Escherichia coli contribute to ribosome assembly and protein translation. Nucleic Acids Res. 44, 5798–5810.

Leidig, C., Thoms, M., Holdermann, I., Bradatsch, B., Berninghausen, O., Bange, G., Sinning, I., Hurt, E., Beckmann, R., 2014. 60S ribosome biogenesis requires rotation of the 5S ribonucleoprotein particle. Nat. Commun. 5, 1–8.

Li, C.O., Chen, D., Luo, M., Ge, M., Zhu, J., 2014. Knockdown of ribosomal protein L39 by RNA interference inhibits the growth of human pancreatic cancer cells in vitro and in vivo. Biotechnol. J. 9, 652–663.

Li, N., Chen, Y., Guo, Q., Zhang, Y., Yuan, Y., Ma, C., Deng, H., Lei, J., Gao, N., 2013. Cryo-EM structures of the late-stage assembly intermediates of the bacterial 50S ribosomal subunit. Nucleic Acids Res. 41, 7073–7083.

Liang, X., Zuo, M., Zhang, Y., Li, N., Dong, M., Gao, N., Ma, C., 2020. Structural snapshots of human pre-60S ribosomal particles before and after nuclear export. Nat. Commun. 11, 1–14.

Liutkute, M., Samatova, E., Rodnina, M. V, 2020. Cotranslational Folding of Proteins on the Ribosome. Biomolecules 10, 1–5.

Lo, K.Y., Li, Z., Bussiere, C., Bresson, S., Marcotte, E.M., Johnson, A.W., 2010. Defining the pathway of cytoplasmic maturation of the 60S ribosomal subunit. Mol. Cell 39, 196–208.

Longtine, M.S., McKenzie, A., Demarini, D.J., Shah, N.G., Wach, A., Brachat, A., Philippsen, P., Pringle, J.R., 1998. Additional modules for versatile and economical PCR-based gene deletion and modification in Saccharomyces cerevisiae. Yeast 14, 953–961.

Ma, C., Wu, S., Li, N., Chen, Y., Yan, K., Li, Z., Zheng, L., Lei, J., Jr, J.L.W., Gao, N., 2017. Structural snapshot of cytoplasmic pre-60S ribosomal particles bound by Nmd3 , Lsg1 , Tif6 and Reh1. Nat. Struct. Mol. Biol. 24, 214–220.

Malyutin, A.G., Musalgaonkar, S., Patchett, S., Frank, J., Johnson, A.W., 2017. Nmd3 is a structural mimic of eIF5A , and activates the cpGTPase Lsg1 during 60S ribosome biogenesis. EMBO J. 36, 854–868.

Manikas, R.G., Thomson, E., Thoms, M., Hurt, E., 2016. The K+-dependent GTPase Nug1 is implicated in the association of the helicase Dbp10 to the immature peptidyl transferase centre during ribosome maturation. Nucleic Acids Res. 44, 1800–1812.

Mankin, A.S., 2006. Nascent peptide in the ‘ birth canal ’ of the ribosome. Trends Biochem. Sci. 31, 11–13.

Mankin, A.S., 2011. Picky nascent peptides do not talk to foreign ribosomes. Proc. Natl. Acad. Sci. 108, 5931–5932.

Maracci, C., Rodnina, M. V, 2016. Translational GTPases. Biopolymers 105, 463–475.

Mastronarde, D.N., 2005. Automated electron microscope tomography using robust prediction of specimen movements. J. Struct. Biol. 152, 36–51.

Matsuo, Y., Granneman, S., Thoms, M., Manikas, R., Tollervey, D., Hurt, E., 2014. Coupled GTPase and remodelling ATPase activities form a checkpoint for ribosome export. Nature 505, 112–116.

Micic, J., Li, Y., Wu, S., Wilson, D., Tutuncuoglu, B., Gao, N., Jr, J.L.W., 2020. Coupling of 5S RNP rotation with maturation of functional centers during large ribosomal subunit assembly. Nat. Commun. 11, 1–16.

Mulder, A., Yoshioka, C., Beck, A., Bunner, A., Milligan, R., Potter, C., Carragher, B., Williamson, J.R., 2011. Visualizing Ribosome Biogenesis: Parallel Assembly Pathways for the 30S Subunit. Science (80-.). 673, 673–677.

Musalgaonkar, S., Black, J.J., Johnson, A.W., 2019. The L1 stalk is required for efficient export of nascent large ribosomal subunits in yeast. RNA 25, 1549–1560.

Parnell, K.M., Bass, B.L., 2009. Functional redundancy of yeast proteins Reh1 and Rei1 in cytoplasmic 60S subunit maturation. Mol. Cell. Biol. 29, 4014–23.

Patchett, S., Musalgaonkar, S., Malyutin, A.G., Johnson, A.W., 2017. The T-cell leukemia related rpl10-R98S mutant traps the 60S export adapter Nmd3 in the ribosomal P site in yeast. PLoS Genet. 13, e1006894.

Peña, C., Hurt, E., Panse, V.G., 2017. Eukaryotic ribosome assembly, transport and quality control. Nat. Struct. Mol. Biol. 24, 689–699.

Pettersen, E.F., Goddard, T.D., Huang, C.C., Couch, G.S., Greenblatt, D.M., Meng, E.C., Ferrin, T.E., 2004. UCSF Chimera — A Visualization System for Exploratory Research and Analysis. In: Wiley InterScience. pp. 1605–1612.

Pillet, B., García-Gómez, J.J., Pausch, P., Falquet, L., Bange, G., de la Cruz, J., Kressler, D., 2015. The Dedicated Chaperone Acl4 Escorts Ribosomal Protein Rpl4 to Its Nuclear Pre-60S Assembly Site. PLoS Genet. 11, 1–34.

Polacek, N., Mankin, A.S., 2005. The Ribosomal Peptidyl Transferase Center: Structure, Function, Evolution, Inhibition. Crit. Rev. Biochem. Mol. Biol. 9238, 285–311.

Réblová, K., Šponer, J., Lankaš, F., 2012. Structure and mechanical properties of the ribosomal L1 stalk three-way junction. Nucleic Acids Res. 40, 6290–6303.

Rodgers, M.L., Woodson, S.A., Rodgers, M.L., Woodson, S.A., 2019. Transcription Increases the Cooperativity of Ribonucleoprotein Assembly Article. Cell 179, 1370-1381.e12.

Sahasranaman, A., Dembowski, J., Strahler, J., Andrews, P., Maddock, J., Woolford, J.L., 2011. Assembly of Saccharomyces cerevisiae 60S ribosomal subunits: role of factors required for 27S pre-rRNA processing. EMBO J. 30, 4020–4032.

Sanghai, Z.A., Miller, L., Molloy, K.R., Barandun, J., Hunziker, M., Chaker-Margot, M.,

Wang, J., Chait, B.T., Klinge, S., 2018. Modular assembly of the nucleolar pre-60S ribosomal subunit. Nature 556, 126–129.

Sarkar, A., Thoms, M., Barrio-garcia, C., Thomson, E., Flemming, D., Beckmann, R., Hurt, E., 2017. Preribosomes escaping from the nucleus are caught during translation by cytoplasmic quality control. Nat. Struct. Mol. Biol. 24, 1107–1115.

Scheres, S.H.W., 2012. RELION: Implementation of a Bayesian approach to cryo-EM structure determination. J. Struct. Biol. 180, 519–530.

Schindelin, J., Arganda-carreras, I., Frise, E., Kaynig, V., Longair, M., Pietzsch, T., Preibisch, S., Rueden, C., Saalfeld, S., Schmid, B., Tinevez, J., White, D.J., Hartenstein, V., Eliceiri, K., Tomancak, P., Cardona, A., 2012. Fiji : an open-source platform for biological-image analysis. Nat. Methods 9.

Seefeldt, A.C., Graf, M., Natacha, P., Nguyen, F., Arenz, S., Mardirossian, M., Scocchi, M., Wilson, D.N., Innis, A., Pramps, P., 2016. Structure of the mammalian antimicrobial peptide Bac7 (1 – 16) bound within the exit tunnel of a bacterial ribosome 44, 2429–2438.

Seefeldt, A.C., Nguyen, F., Antunes, S., Pérébaskine, N., Graf, M., Arenz, S., Inampudi, K.K., Douat, C., Guichard, G., Wilson, D.N., Innis, C.A., 2015. The proline-rich antimicrobial peptide Onc112 inhibits translation by blocking and destabilizing the initiation complex 22.

Shaikh, T.R., Gao, H., Baxter, W.T., Asturias, F.J., Boisset, N., Leith, A., Frank, J., 2008. Spider image processing for single-particle reconstruction of biological macromolecules from electron micrographs. Nat. Protoc. 3, 1941–1974.

Smith, M.W., Meskauskas, A., Wang, P., Sergiev, P. V, Dinman, J.D., 2001. Saturation Mutagenesis of 5S rRNA in Saccharomyces cerevisiae. Mol. Cell. Biol. 21, 8264–

8275.

Steffen, K.K., Mccormick, M.A., Pham, K.M., Mackay, V.L., Delaney, J.R., Murakami, C.J., Kaeberlein, M., Kennedy, B.K., 2012. Ribosome Deficiency Protects Against ER Stress in Saccharomyces cerevisiae. Genetics 191, 107–118.

Stelter, P., Huber, F.M., Kunze, R., Flemming, D., Hoelz, A., Hurt, E., 2015. Coordinated Ribosomal L4 Protein Assembly into the Pre-Ribosome Is Regulated by Its Eukaryote-Specific Extension. Mol. Cell 58, 854–862.

Strunk, B.S., Karbstein, K., 2009. Powering through ribosome assembly. RNA 15, 2083–2104.

Su, T., Cheng, J., Sohmen, D., Hedman, R., Berninghausen, O., Heijne, G. Von, Wilson, D.N., Beckmann, R., 2017. The force-sensing peptide VemP employs extreme compaction and secondary structure formation to induce ribosomal stalling. Elife 1–17.

Talkish, J., Biedka, S., Jakovljevic, J., Zhang, J., Tang, L., Strahler, J.R., Andrews, P.C., Maddock, J.R., Woolford, J.L., 2016. Disruption of ribosome assembly in yeast blocks co-transcriptional pre-rRNA processing and affects the global hierarchy of ribosome biogenesis. Rna 22, 852–866.

Talkish, J., Zhang, J., Jakovljevic, J., Horsey, E.W., Woolford, J.L., 2012. Hierarchical recruitment into nascent ribosomes of assembly factors required for 27SB pre-rRNA processing in Saccharomyces cerevisiae. Nucleic Acids Res. 40, 8646–8661.

Thoms, M., Mitterer, V., Kater, L., Falquet, L., Beckmann, R., Kressler, D., Hurt, E., 2018. Suppressor mutations in Rpf2–Rrs1 or Rpl5 bypass the Cgr1 function for pre-ribosomal 5S RNP-rotation. Nat. Commun. 9, 1–13.

Tutuncuoglu, B., Jakovljevic, J., Wu, S., Gao, N., Woolford, J.L., 2016. The N-terminal

extension of yeast ribosomal protein L8 is involved in two major remodeling events during late nuclear stages of 60S ribosomal subunit assembly. RNA 22, 1386–1399.

Vanrobays, E., Leplus, A., Osheim, Y.N., Beyer, A.L., Wacheul, L., Lafontaine, D.L.J., 2008. TOR regulates the subcellular distribution of DIM2, a KH domain protein required for cotranscriptional ribosome assembly and pre-40S ribosome export. RNA 14, 2061–2073.

Vázquez-Laslop, N., Mankin, A.S., 2018. How Macrolide Antibiotics Work. Trends Biochem. Sci. 43, 1–17.

Voorhees, R.M., Ramakrishnan, V., 2013. Structural basis of the translational elongation cycle. Annu. Rev. Biochem. 203–236.

Wekselman, I., Zimmerman, E., Davidovich, C., Lindahl, L., Zengel, J.M., Yonath, A., Wekselman, I., Zimmerman, E., Davidovich, C., Belousoff, M., Matzov, D., Krupkin, M., Rozenberg, H., Bashan, A., Friedlander, G., Kjeldgaard, J., Ingmer, H., Lindahl, L., Zengel, J.M., 2017. The Ribosomal Protein uL22 Modulates the Shape of the Protein Exit Tunnel Article The Ribosomal Protein uL22 Modulates the Shape of the Protein Exit Tunnel. Structure 25, 1–9.

Wilson, D., Bhushan, S., Becker, T., Beckmann, R., 2011. Nascent polypeptide chains within the ribosomal tunnel analyzed by cryo-EM. Ribos. Struct. Funct. Dyn. 23, 393–404.

Wilson, D.M., Li, Y., LaPeruta, A., Gamalinda, M., Gao, N., Jr, J.L.W., 2020. Structural insights into assembly of the ribosomal nascent polypeptide exit tunnel. Nat. Commun. 11, 1–15.

Wilson, D.N., Arenz, S., Beckmann, R., 2016. Translation regulation via nascent

polypeptide-mediated ribosome stalling. Curr. Opin. Struct. Biol. 37, 123–133.

Wilson, D.N., Beckmann, R., 2011. The ribosomal tunnel as a functional environment for nascent polypeptide folding and translational stalling. Curr. Opin. Struct. Biol. 21, 274–282.

Woolford, J.L., Baserga, S.J., 2013. Ribosome biogenesis in the yeast Saccharomyces cerevisiae. Genetics 195, 643–681.

Wu, C., Wei, J., Lin, P.-J., Tu, L., Deutsch, C., Johnson, A.E., Sachs, M.S., 2012. Arginine changes the conformation of the arginine attenuator peptide relative to the ribosome tunnel. J. Mol. Biol. 416, 518–533.

Wu, S., Tutuncuoglu, B., Yan, K., Brown, H., Zhang, Y., Tan, D., Gamalinda, M., Yuan, Y., Li, Z., Jakovljevic, J., Ma, C., Lei, J., Dong, M.-Q., Woolford, J.L.J., Gao, N., 2016. Diverse roles of assembly factors revealed by structures of late nuclear pre-60S ribosomes. Nature 534, 133–137.

Zaman, S., Fitzpatrick, M., Lindahl, L., Zengel, J., 2007. Novel mutations in ribosomal proteins L4 and L22 that confer erythromycin resistance in Escherichia coli. Mol. Microbiol. 66, 1039–1050.

Zavialov, A. V, Mora, L., Buckingham, R.H., Uppsala, S.-, Physico-chimique, I.D.B., 2002. Release of Peptide Promoted by the GGQ Motif of Class 1 Release Factors Regulates the GTPase Activity of RF3. Mol. Cell 10, 789–798.

Zhang, J., Harnpicharnchai, P., Jakovljevic, J., Tang, L., Guo, Y., Oeffinger, M., Rout, M.P., Hiley, S.L., Hughes, T., Woolford, J.L., 2007. Assembly factors Rpf2 and Rrs1 recruit 5S rRNA and ribosomal proteins rpL5 and rpL11 into nascent ribosomes. Genes Dev. 21, 2580–2592.

Zhang, K., 2016. Gctf: Real-time CTF determination and correction. J. Struct. Biol. 193,

1–12.

Zhang, X., Yan, K., Zhang, Yixiao, Li, N., Ma, C., Li, Z., Zhang, Yanqing, Feng, B., Liu, J., Sun, Y., Xu, Y., Lei, J., Gao, N., 2014. Structural insights into the function of a unique tandem GTPase EngA in bacterial ribosome assembly. Nucleic Acids Res. 42, 13430–13439.

Zhao, M., Wu, S., Zhou, Q., Vivona, S., Cipriano, D.J., Cheng, Y., Brunger, A.T., Physiology, C., Francisco, S., 2015. Mechanistic insights into the recycling machine of the SNARE complex. Nature 518, 61–67.

Zheng, S.Q., Palovcak, E., Armache, J.P., Verba, K.A., Cheng, Y., Agard, D.A., 2017. MotionCor2: Anisotropic correction of beam-induced motion for improved cryo-electron microscopy. Nat. Methods 14, 331–332.

Zhou, Y., Musalgaonkar, S., Johnson, A.W., Taylor, D., 2018. Tightly-orchestrated rearrangements govern catalytic center assembly of the ribosome. Nat. Commun. 10, 1–34.

Strain	Genotype	Source
JWY11801	MATa ura3-52 trp1-1 lys2-801 his3-Δ200 leu2-Δ1 *GAL-HA-NOG1* KANMX6 pRS315 LEU2	Gal-HA-Nog1 +pRS315
JWY11802	MATa ura3-52 trp1-1 lys2-801 his3-Δ200 leu2-Δ1 *GAL-HA-NOG1* KANMX6 pRS315 LEU2	Gal-HA-Nog1 +pRS315
JWY11803	MATa ura3-52 trp1-1 lys2-801 his3-Δ200 leu2-Δ1 *GAL-HA-NOG1* KANMX6 pRS315_*nog1 GESDR-AAAAA* LEU2	Gal-HA-Nog1 +pRS315 *nog1 GESDR-AAAAA*
JWY11804	MATa ura3-52 trp1-1 lys2-801 his3-Δ200 leu2-Δ1 *GAL-HA-NOG1* KANMX6 pRS315_*nog1 GESDR-AAAAA* LEU2	Gal-HA-Nog1 +pRS315 *nog1 GESDR-AAAAA*
JWY11805	MATa ura3-52 trp1-1 lys2-801 his3-Δ200 leu2-Δ1 *GAL-HA-NOG1* KANMX6 pRS315_*nog1 KHLF-AAAA* LEU2	Gal-HA-Nog1 +pRS315 *nog1 KHLF-AAAA*
JWY11806	MATa ura3-52 trp1-1 lys2-801 his3-Δ200 leu2-Δ1 *GAL-HA-NOG1* KANMX6 pRS315_*nog1 KHLF-AAAA* LEU2	Gal-HA-Nog1 +pRS315 *nog1 KHLF-AAAA*
JWY11807	MATa ura3-52 trp1-1 lys2-801 his3-Δ200 leu2-Δ1 *GAL-HA-NOG1* KANMX6 pRS315_*nog1 SGKR-AAAA* LEU2	Gal-HA-Nog1 +pRS315 *nog1 SGKR-AAAA*

JWY11808	MATa ura3-52 trp1-1 lys2-801 his3-Δ200 leu2-Δ1 *GAL-HA-NOG1* KANMX6 pRS315_*nog1 SGKR-AAAA* LEU2	Gal-HA-Nog1 +pRS315 *nog1 SGKR-AAAA*
JWY11809	MATa ura3-52 trp1-1 lys2-801 his3-Δ200 leu2-Δ1 *GAL-HA-NOG1* KANMX6 pRS315_*nog1 +35aa on C-term* LEU2	Gal-HA-Nog1 +pRS315 *nog1 +35aa on C-term*
JWY11810	MATa ura3-52 trp1-1 lys2-801 his3-Δ200 leu2-Δ1 *GAL-HA-NOG1* KANMX6 pRS315_*nog1 +35aa on C-term* LEU2	Gal-HA-Nog1 +pRS315 *nog1 +35aa on C-term*
JWY11811	MATa ura3-52 trp1-1 lys2-801 his3-Δ200 leu2-Δ1 *GAL-HA-NOG1* KANMX6 pRS315_*nog1Δ642-647* LEU2	Gal-HA-Nog1 +pRS315 *nog1Δ642-647*
JWY11812	MATa ura3-52 trp1-1 lys2-801 his3-Δ200 leu2-Δ1 *GAL-HA-NOG1* KANMX6 pRS315_*nog1Δ642-647* LEU2	Gal-HA-Nog1 +pRS315 *nog1Δ642-647*
JWY11813	MATa ura3-52 trp1-1 lys2-801 his3-Δ200 leu2-Δ1 *GAL-HA-NOG1* KANMX6 pRS315_*nog1 +35aa on C-term* LEU2 pRS316 Nop1-mRFP L25-eGFP URA3	Gal-HA-Nog1 +pRS315 *nog1 +35aa on C-term* +pRS316 Nop1-mRFP L25-eGFP
JWY11814	MATa ura3-52 trp1-1 lys2-801 his3-Δ200 leu2-Δ1	Gal-HA-Nog1 +pRS315 *nog1 +35aa on C-term* +pRS316 Nop1-mRFP L25-eGFP

	GAL-HA-NOG1 KANMX6 pRS315_*nog1 +35aa on C-term* LEU2 pRS316 Nop1-mRFP L25-eGFP URA3	
JWY11815	MATa ura3-52 trp1-1 lys2-801 his3-∆200 leu2-∆1 *GAL-HA-NOG1* KANMX6 pRS315_*nog1Δ642-647* LEU2 pRS316 Nop1-mRFP L25-eGFP URA3	Gal-HA-Nog1 +pRS315 *nog1Δ642-647* +pRS316 Nop1-mRFP L25-eGFP
JWY11816	MATa ura3-52 trp1-1 lys2-801 his3-∆200 leu2-∆1 *GAL-HA-NOG1* KANMX6 pRS315_*nog1Δ642-647* LEU2 pRS316 Nop1-mRFP L25-eGFP URA3	Gal-HA-Nog1 +pRS315 *nog1Δ642-647* +pRS316 Nop1-mRFP L25-eGFP
JWY11817	MATa ura3-52 trp1-1 lys2-801 his3-∆200 leu2-∆1 *GAL-HA-NOG1* KANMX6 pRS315_*nog1 GVGK-AAAA* LEU2	Gal-HA-Nog1 +pRS315 *nog1 GVGK-AAAA*
JWY11818	MATa ura3-52 trp1-1 lys2-801 his3-∆200 leu2-∆1 *GAL-HA-NOG1* KANMX6 pRS315_*nog1 GVGK-AAAA* LEU2	Gal-HA-Nog1 +pRS315 *nog1 GVGK-AAAA*
JWY11819	MATa ura3-52 trp1-1 lys2-801 his3-∆200 leu2-∆1 *GAL-HA-NOG1* KANMX6 pRS315_*nog1 TDFR-AAAA* LEU2	Gal-HA-Nog1 +pRS315 *nog1 TDFR-AAAA*
JWY11820	MATa ura3-52 trp1-1 lys2-801 his3-∆200 leu2-∆1 *GAL-HA-NOG1* KANMX6 pRS315_*nog1 TDFR-AAAA* LEU2	Gal-HA-Nog1 +pRS315 *nog1 TDFR-AAAA*

JWY11821	MATa ura3-52 trp1-1 lys2-801 his3-Δ200 leu2-Δ1 *GAL-HA-NOG1* KANMX6 pRS315_*nog1 TDFR-AAAA* LEU2 pRS316 Nop1-mRFP L25-eGFP URA3	Gal-HA-Nog1 +pRS315 *nog1 TDFR-AAAA* +pRS316 Nop1-mRFP L25-eGFP
JWY11822	MATa ura3-52 trp1-1 lys2-801 his3-Δ200 leu2-Δ1 *GAL-HA-NOG1* KANMX6 pRS315_*nog1 TDFR-AAAA* LEU2 pRS316 Nop1-mRFP L25-eGFP URA3	Gal-HA-Nog1 +pRS315 *nog1 TDFR-AAAA* +pRS316 Nop1-mRFP L25-eGFP
JWY11823	MATa ura3-52 trp1-1 lys2-801 his3-Δ200 leu2-Δ1 *GAL-HA-NOG1* KANMX6 pRS315_*nog1 KHLF-AAAA* LEU2 pRS316 Nop1-mRFP L25-eGFP URA3	Gal-HA-Nog1 +pRS315 *nog1 KHLF-AAAA* +pRS316 Nop1-mRFP L25-eGFP
JWY11824	MATa ura3-52 trp1-1 lys2-801 his3-Δ200 leu2-Δ1 *GAL-HA-NOG1* KANMX6 pRS315_*nog1 KHLF-AAAA* LEU2 pRS316 Nop1-mRFP L25-eGFP URA3	Gal-HA-Nog1 +pRS315 *nog1 KHLF-AAAA* +pRS316 Nop1-mRFP L25-eGFP
JWY11825	MATa ura3-52 trp1-1 lys2-801 his3-Δ200 leu2-Δ1 *GAL-HA-NOG1* KANMX6 pRS315_*NOG1* LEU2	Gal-HA-Nog1 +pRS315 *NOG1*
JWY11826	MATa ura3-52 trp1-1 lys2-801 his3-Δ200 leu2-Δ1 *GAL-HA-NOG1* KANMX6 pRS315_*NOG1* LEU2	Gal-HA-Nog1 +pRS315 *NOG1*

JWY11827	MATa ura3-52 trp1-1 lys2-801 his3-Δ200 leu2-Δ1 *GAL-NOG1* TRP1	Gal-Nog1
JWY11828	MATa ura3-52 trp1-1 lys2-801 his3-Δ200 leu2-Δ1 *GAL-NOG1* TRP1	Gal-Nog1
JWY11829	MATa his3Δ1 leu2Δ0 met15Δ0 ura3Δ0 rei1::KANMX6	*rei1Δ* From Arlen Johnson
JWY11830	MATa his3Δ1 leu2Δ0 met15Δ0 ura3Δ0 rei1::KANMX6	*rei1Δ* From Arlen Johnson
JWY11831	MATa his3Δ ade2 leu2Δ trp1Δ ura3Δ arx1::Arx1-GFP HIS3MX	Arx1-GFP From Arlen Johnson
JWY11832	MATa his3Δ ade2 leu2Δ trp1Δ ura3Δ trp1Δ ura3Δ arx1::Arx1-GFP HIS3MX	Arx1-GFP From Arlen Johnson
JWY11833	MATa his3Δ ade2 leu2Δ trp1Δ ura3Δ	*drg1-ts* From Arlen Johnson
JWY11834	MATa his3Δ ade2 leu2Δ trp1Δ ura3Δ	*drg1-ts* From Arlen Johnson
JWY11835	MATa his3Δ1 leu2Δ0 met15Δ0 ura3Δ0 arx1::Arx1-GFP HIS3MX	Arx1-GFP From Arlen Johnson
JWY11836	MATa his3Δ1 leu2Δ0 met15Δ0 ura3Δ0 arx1::Arx1-GFP HIS3MX	Arx1-GFP From Arlen Johnson
JWY11837	MATa his3Δ1 leu2Δ0 met15Δ0 ura3Δ0 tif6::Tif6-GFP HIS3MX	Tif6-GFP From Arlen Johnson
JWY11838	MATa his3Δ1 leu2Δ0 met15Δ0 ura3Δ0 tif6::Tif6-GFP HIS3MX	Tif6-GFP From Arlen Johnson

JWY11839	MATa his3Δ1 leu2Δ0 met15Δ0 ura3Δ0 tif6::Tif6-GFP HIS3MX rei1::KANMX	Tif6-GFP *rei1Δ* From Arlen Johnson
JWY11840	MATa his3Δ1 leu2Δ0 met15Δ0 ura3Δ0 tif6::Tif6-GFP HIS3MX rei1::KANMX	Tif6-GFP *rei1Δ* From Arlen Johnson
JWY11841	MATa his3Δ ade2 leu2Δ trp1Δ ura3Δ tif6::Tif6-GFP HIS3MX	Tif6-GFP From Arlen Johnson
JWY11842	MATa his3Δ ade2 leu2Δ trp1Δ ura3Δ tif6::Tif6-GFP HIS3MX	Tif6-GFP From Arlen Johnson
JWY11843	MATa his3Δ ade2 leu2Δ trp1Δ ura3Δ tif6::Tif6-GFP HIS3MX	*drg1-ts* Tif6-GFP From Arlen Johnson
JWY11844	MATa his3Δ ade2 leu2Δ trp1Δ ura3Δ tif6::Tif6-GFP HIS3MX	*drg1-ts* Tif6-GFP From Arlen Johnson
JWY11845	MATa his3Δ ade2 leu2Δ trp1Δ ura3Δ arx1::Arx1-GFP HIS3MX	*drg1-ts* Arx1-GFP From Arlen Johnson
JWY11846	MATa his3Δ ade2 leu2Δ trp1Δ ura3Δ arx1::Arx1-GFP HIS3MX	*drg1-ts* Arx1-GFP From Arlen Johnson
JWY11847	MATa his3Δ1 leu2Δ0 met15Δ0 ura3Δ0 rei1::KANMX6 arx1::Arx1-GFP HIS3	Arx1-GFP *rei1Δ* From Arlen Johnson
JWY11848	MATa his3Δ1 leu2Δ0 met15Δ0 ura3Δ0 rei1::KANMX6 arx1::Arx1-GFP HIS3	Arx1-GFP *rei1Δ* From Arlen Johnson
JWY11849	MATa his3Δ1 leu2Δ0 met15Δ0 ura3Δ0 nog1::Nog1-GFP HIS3 nog2::Nog2-TAP URA3	Nog1-GFP Nog2-TAP

JWY11850	MATa his3Δ1 leu2Δ0 met15Δ0 ura3Δ0 nog1::Nog1-GFP HIS3 nog2::Nog2-TAP URA3	Nog1-GFP Nog2-TAP
JWY11851	MATa his3Δ1 leu2Δ0 met15Δ0 ura3Δ0 nog1::Nog1-GFP HIS3 nop7::Nop7-TAP URA3	Nog1-GFP Nop7-TAP
JWY11852	MATa his3Δ1 leu2Δ0 met15Δ0 ura3Δ0 nog1::Nog1-GFP HIS3 nop7::Nop7-TAP URA3	Nog1-GFP Nop7-TAP
JWY11853	MATa ura3-52 trp1-1 lys2-801 his3-Δ200 leu2-Δ1 *GAL-NOG1*::TRP1 nop7::Nop7-TAP URA3	Gal-Nog1 Nop7-TAP
JWY11854	MATa ura3-52 trp1-1 lys2-801 his3-Δ200 leu2-Δ1 *GAL-NOG1*::TRP1 nop7::Nop7-TAP URA3	Gal-Nog1 Nop7-TAP
JWY11855	MATa ura3-52 trp1-1 lys2-801 his3-Δ200 leu2-Δ1 *GAL-NOG1*::TRP1 nog2::Nog2-TAP URA3	Gal-Nog1 Nog2-TAP
JWY11856	MATa ura3-52 trp1-1 lys2-801 his3-Δ200 leu2-Δ1 *GAL-NOG1*::TRP1 nog2::Nog2-TAP URA3	Gal-Nog1 Nog2-TAP
JWY11857	MATa his3Δ1 leu2Δ0 met15Δ0 ura3Δ0 rei1::KANMX6 tif6::Tif6-GFP HIS3 nog1::Nog1-TAP URA3	Tif6-GFP Nog1-TAP *rei1Δ* From Arlen Johnson

JWY11858	MATa his3Δ1 leu2Δ0 met15Δ0 ura3Δ0 rei1::KANMX6 tif6::Tif6-GFP HIS3 nog1::Nog1-TAP URA3	Tif6-GFP Nog1-TAP *rei1Δ* From Arlen Johnson
JWY11859	MATa his3Δ1 leu2Δ0 met15Δ0 ura3Δ0 rei1::KANMX6 arx1::Arx1-GFP HIS3 nog1::Nog1-TAP URA3	Arx1-GFP Nog1-TAP *rei1Δ* From Arlen Johnson
JWY11860	MATa his3Δ1 leu2Δ0 met15Δ0 ura3Δ0 rei1::KANMX6 arx1::Arx1-GFP HIS3 nog1::Nog1-TAP URA3	Arx1-GFP Nog1-TAP *rei1Δ* From Arlen Johnson
JWY11861	MATa ura3-52 trp1-1 lys2-801 his3-Δ200 leu2-Δ1 *GAL-NOG1*::TRP1 reh1::KANMX6	Gal-Nog1 *reh1Δ*
JWY11862	MATa ura3-52 trp1-1 lys2-801 his3-Δ200 leu2-Δ1 *GAL-NOG1*::TRP1 reh1::KANMX6	Gal-Nog1 *reh1Δ*
JWY11863	MATa ura3-52 trp1-1 lys2-801 his3-Δ200 leu2-Δ1 l4b::KANMX6 l4a::GAL-HA3-RPL4A TRP1 nog2::Nog2-TAP URA3	Gal-HA-L4A Nog2-TAP
JWY11864	MATa ura3-52 trp1-1 lys2-801 his3-Δ200 leu2-Δ1 l4b::KANMX6 l4a::GAL-HA3-RPL4A TRP1 nog2::Nog2-TAP URA3	Gal-HA-L4A Nog2-TAP

JWY11865	MATa ura3-52 trp1-1 lys2-801 his3-Δ200 leu2-Δ1 l4b::KANMX6 l4a::GAL-HA3-RPL4A TRP1 pRS315_L4ΔA63-87 LEU2	Gal-HA-L4A +pRS315 *rpl4Δ63-87*
JWY11866	MATa ura3-52 trp1-1 lys2-801 his3-Δ200 leu2-Δ1 l4b::KANMX6 l4a::GAL-HA3-RPL4A TRP1 pRS315_L4ΔA63-87 LEU2	Gal-HA-L4A +pRS315 *rpl4Δ63-87*
JWY11867	MATa ura3-52 trp1-1 lys2-801 his3-Δ200 leu2-Δ1 l4b::KANMX6 l4a::GAL-HA3-RPL4A TRP1 nog2::Nog2-TAP URA3 pRS315_L4ΔA63-87 LEU2	Gal-HA-L4A Nog2-TAP +pRS315 *rpl4Δ63-87*
JWY11868	MATa ura3-52 trp1-1 lys2-801 his3-Δ200 leu2-Δ1 l4b::KANMX6 l4a::GAL-HA3-RPL4A TRP1 nog2::Nog2-TAP URA3 pRS315_L4ΔA63-87 LEU2	Gal-HA-L4A Nog2-TAP +pRS315 *rpl4Δ63-87*
JWY11869	MATa ura3-52 trp1-1 lys2-801 his3-Δ200 leu2-Δ1 l4b::KANMX6 l4a::GAL-HA3-RPL4A TRP1 pRS315_L4Δ63-75 LEU2	Gal-HA-L4A +pRS315 *rpl4Δ63-75*
JWY11870	MATa ura3-52 trp1-1 lys2-801 his3-Δ200 leu2-Δ1 l4b::KANMX6 l4a::GAL-HA3-RPL4A TRP1 pRS315_L4Δ63-75 LEU2	Gal-HA-L4A +pRS315 *rpl4Δ63-75*
JWY11871	MATa ura3-52 trp1-1 lys2-801 his3-Δ200 leu2-Δ1 l4b::KANMX6 l4a::GAL-HA3-RPL4A TRP1 pRS315_L4Δ46-111 LEU2	Gal-HA-L4A Nog2-TAP +pRS315 *rpl4Δ46-111*

JWY11872	MATa ura3-52 trp1-1 lys2-801 his3-Δ200 leu2-Δ1 l4b::KANMX6 l4a::GAL-HA3-RPL4A TRP1 pRS315_L4Δ46-111 LEU2	Gal-HA-L4A Nog2-TAP +pRS315 *rpl4Δ46-111*
JWY11873	MATa ura3-52 trp1-1 lys2-801 his3-Δ200 leu2-Δ1 reh1::KANMX6	*reh1Δ*
JWY11874	MATa ura3-52 trp1-1 lys2-801 his3-Δ200 leu2-Δ1 reh1::KANMX6	*reh1Δ*
JWY11875	MATa his3Δ1 leu2Δ0 met15Δ0 ura3Δ0 reh1::KANMX6	*reh1Δ* (BY4741 background)
JWY11876	MATa his3Δ1 leu2Δ0 met15Δ0 ura3Δ0 reh1::KANMX6	*reh1Δ* (BY4741 background)
JWY11877	MATa his3Δ1 leu2Δ0 met15Δ0 ura3Δ0 reh1::KANMX6 nog1::Nog1-GFP HIS3	Nog1-GFP *reh1Δ*
JWY11878	MATa his3Δ1 leu2Δ0 met15Δ0 ura3Δ0 reh1::KANMX6 nog1::Nog1-GFP HIS3	Nog1-GFP *reh1Δ*
JWY11879	MATa ura3-52 trp1-1 lys2-801 his3-Δ200 leu2-Δ1 arx1::HIS3	*arx1Δ*
JWY11880	MATa ura3-52 trp1-1 lys2-801 his3-Δ200 leu2-Δ1 arx1::HIS3	*arx1Δ*
JWY 11881	MATa ura3-52 trp1-1 lys2-801 his3-Δ200 leu2-Δ1 l4b::KANMX6 l4a::GAL-HA3-RPL4A TRP1 pRS315_L4A LEU2 pRS316_Nop1-mRFP L25-eGFP URA3	Gal-HA-L4A +pRS315 *RPL4A* +pRS316 Nop1-mRFP L25-eGFP

JWY 11882	MATa ura3-52 trp1-1 lys2-801 his3-Δ200 leu2-Δ1 l4b::KANMX6 l4a::GAL-HA3-RPL4A TRP1 pRS315_L4A LEU2 pRS316_Nop1-mRFP L25-eGFP URA3	Gal-HA-L4A +pRS315 *RPL4A* +pRS316 Nop1-mRFP L25-eGFP
JWY11883	MATa ura3-52 trp1-1 lys2-801 his3-Δ200 leu2-Δ1 l4b::KANMX6 l4a::GAL-HA3-RPL4A TRP1 pRS315 LEU2 pRS316_Nop1-mRFP L25-eGFP URA3	Gal-HA-L4A +pRS315 +pRS316 Nop1-mRFP L25-eGFP
JWY11884	MATa ura3-52 trp1-1 lys2-801 his3-Δ200 leu2-Δ1 l4b::KANMX6 l4a::GAL-HA3-RPL4A TRP1 pRS315 LEU2 pRS316_Nop1-mRFP L25-eGFP URA3	Gal-HA-L4A +pRS315 +pRS316 Nop1-mRFP L25-eGFP
JWY11885	MATa ura3-52 trp1-1 lys2-801 his3-Δ200 leu2-Δ1 l4b::KANMX6 l4a::GAL-HA3-RPL4A TRP1 pRS315_L4AΔ63-75 LEU2 pRS316_Nop1-mRFP L25-eGFP URA3	Gal-HA-L4A +pRS315 *rpl4Δ63-75* +pRS316 Nop1-mRFP L25-eGFP
JWY11886	MATa ura3-52 trp1-1 lys2-801 his3-Δ200 leu2-Δ1 l4b::KANMX6 l4a::GAL-HA3-RPL4A TRP1 pRS315_L4AΔ63-75 LEU2 pRS316_Nop1-mRFP L25-eGFP URA3	Gal-HA-L4A +pRS315 *rpl4Δ63-75* +pRS316 Nop1-mRFP L25-eGFP
JWY11887	MATa ura3-52 trp1-1 lys2-801 his3-Δ200 leu2-Δ1 l4b::KANMX6 l4a::GAL-HA3-RPL4A TRP1	Gal-HA-L4A +pRS315 *rpl4Δ63-87*

	pRS315_L4A63-87 LEU2 pRS316_Nop1-mRFP L25-eGFP URA3	+pRS316 Nop1-mRFP L25-eGFP
JWY11888	MATa ura3-52 trp1-1 lys2-801 his3-Δ200 leu2-Δ1 l4b::KANMX6 l4a::GAL-HA3-RPL4A TRP1 pRS315_L4A63-87 LEU2 pRS316_Nop1-mRFP L25-eGFP URA3	Gal-HA-L4A +pRS315 *rpl4Δ63-87* +pRS316 Nop1-mRFP L25-eGFP
JWY11899	MATa ura3-52 trp1-1 lys2-801 his3-Δ200 leu2-Δ1 arx1::Arx1-GFP HIS3 rei1::KANMX6	Arx1-GFP *rei1Δ*
JWY11900	MATa ura3-52 trp1-1 lys2-801 his3-Δ200 leu2-Δ1 arx1::Arx1-GFP HIS3 rei1::KANMX6	Arx1-GFP *rei1Δ*
JWY11901	MATa ura3-52 trp1-1 lys2-801 his3-Δ200 leu2-Δ1 arx1::Arx1-GFP HIS3 rei1::KANMX6 nog1::Nog1-TAP URA3	Arx1-GFP Nog1-TAP *rei1Δ*
JWY11902	MATa ura3-52 trp1-1 lys2-801 his3-Δ200 leu2-Δ1 arx1::Arx1-GFP HIS3 rei1::KANMX6 nog1::Nog1-TAP URA3	Arx1-GFP Nog1-TAP *rei1Δ*
JWY11903	MATa ura3-52 trp1-1 lys2-801 his3-Δ200 leu2-Δ1 arx1::Arx1-GFP HIS3 *GAL-NOG1* TRP1	Gal-Nog1 Arx1-GFP

JWY11904	MATa ura3-52 trp1-1 lys2-801 his3-Δ200 leu2-Δ1 arx1::Arx1-GFP HIS3 *GAL-NOG1* TRP1	Gal-Nog1 Arx1-GFP
JWY11905	MATa ura3-52 trp1-1 lys2-801 his3-Δ200 leu2-Δ1 arx1::Arx1-GFP nop7::Nop7-TAP URA3	Arx1-GFP Nop7-TAP
JWY11906	MATa ura3-52 trp1-1 lys2-801 his3-Δ200 leu2-Δ1 arx1::Arx1-GFP nop7::Nop7-TAP URA3	Arx1-GFP Nop7-TAP
JWY11907	MATa ura3-52 trp1-1 lys2-801 his3-Δ200 leu2-Δ1 arx1::Arx1-GFP nog2::Nog2-TAP URA3	Arx1-GFP Nog2-TAP
JWY11908	MATa ura3-52 trp1-1 lys2-801 his3-Δ200 leu2-Δ1 arx1::Arx1-GFP nog2::Nog2-TAP URA3	Arx1-GFP Nog2-TAP
JWY11909	MATa ura3-52 trp1-1 lys2-801 his3-Δ200 leu2-Δ1 arx1::HA-Arx1 nog2::Nog2-TAP URA3	HA-Arx1 Nog2-TAP
JWY11910	MATa ura3-52 trp1-1 lys2-801 his3-Δ200 leu2-Δ1 arx1::HA-Arx1 nog2::Nog2-TAP URA3	HA-Arx1 Nog2-TAP
JWY11911	MATa ura3-52 trp1-1 lys2-801 his3-Δ200 leu2-Δ1 arx1::HA-Arx1 nog2::Nog2-TAP URA3 nog1::Nog1-GFP HIS3	HA-Arx1 Nog2-TAP Nog1-GFP

JWY11912	MATa ura3-52 trp1-1 lys2-801 his3-Δ200 leu2-Δ1 arx1::HA-Arx1 nog2::Nog2-TAP URA3 nog1::Nog1-GFP HIS3	HA-Arx1 Nog2-TAP Nog1-GFP
JWY11913	MATa ura3-52 trp1-1 lys2-801 his3-Δ200 leu2-Δ1 reh1::KANMX6 *GAL-NOG1* TRP1 pRS315_ *NOG1* LEU2	Gal-Nog1 *reh1Δ* +pRS315 *NOG1*
JWY11914	MATa ura3-52 trp1-1 lys2-801 his3-Δ200 leu2-Δ1 reh1::KANMX6 *GAL-NOG1* TRP1 pRS315_ *NOG1* LEU2	Gal-Nog1 *reh1Δ* +pRS315 *NOG1*
JWY11915	MATa ura3-52 trp1-1 lys2-801 his3-Δ200 leu2-Δ1 reh1::KANMX6 *GAL-NOG1* TRP1 arx1::Arx1-GFP HIS3 pRS315_ *NOG1* LEU2	Gal-Nog1 Arx1-GFP *reh1Δ* +pRS315 *NOG1*
JWY11916	MATa ura3-52 trp1-1 lys2-801 his3-Δ200 leu2-Δ1 reh1::KANMX6 *GAL-NOG1* TRP1 arx1::Arx1-GFP HIS3 pRS315_ *NOG1* LEU2	Gal-Nog1 Arx1-GFP *reh1Δ* +pRS315 *NOG1*
JWY11917	MATa ura3-52 trp1-1 lys2-801 his3-Δ200 leu2-Δ1 reh1::KANMX6 *GAL-NOG1* TRP1 arx1::Arx1-GFP HIS3 pRS315_ *nog1Δ595-647* LEU2	Gal-Nog1 Arx1-GFP *reh1Δ* +pRS315 *nog1Δ595-647*
JWY11918	MATa ura3-52 trp1-1 lys2-801 his3-Δ200 leu2-Δ1	Gal-Nog1 Arx1-GFP *reh1Δ* +pRS315 *nog1Δ595-647*

	reh1::KANMX6 *GAL-NOG1* TRP1 arx1::Arx1-GFP HIS3 pRS315_ *nog1Δ595-647* LEU2	
JWY11919	MATa ura3-52 trp1-1 lys2-801 his3-Δ200 leu2-Δ1 reh1::KANMX6 *GAL-NOG1* TRP1 arx1::Arx1-GFP HIS3 pRS315_ *nog1Δ595-647* LEU2	Gal-Nog1 Arx1-GFP *reh1Δ* +pRS315 *nog1Δ595-647*
JWY11920	MATa ura3-52 trp1-1 lys2-801 his3-Δ200 leu2-Δ1 reh1::KANMX6 *GAL-NOG1* TRP1 arx1::Arx1-GFP HIS3 pRS315_ *nog1Δ595-647* LEU2	Gal-Nog1 Arx1-GFP *reh1Δ* +pRS315 *nog1Δ595-647*
JWY11921	MATa ura3-52 trp1-1 lys2-801 his3-Δ200 leu2-Δ1 reh1::KANMX6 *GAL-NOG1* TRP1 pRS315_ *nog1Δ575-647* LEU2	Gal-Nog1 *reh1Δ* +pRS315 *nog1Δ575-647*
JWY11922	MATa ura3-52 trp1-1 lys2-801 his3-Δ200 leu2-Δ1 reh1::KANMX6 *GAL-NOG1* TRP1 pRS315_ *nog1Δ575-647* LEU2	Gal-Nog1 *reh1Δ* +pRS315 *nog1Δ575-647*
JWY11923	MATa ura3-52 trp1-1 lys2-801 his3-Δ200 leu2-Δ1 reh1::KANMX6 *GAL-NOG1* TRP1 pRS315_ *nog1Δ595-647* LEU2	Gal-Nog1 *reh1Δ* +pRS315 *nog1Δ595-647*
JWY11924	MATa ura3-52 trp1-1 lys2-801 his3-Δ200 leu2-Δ1 reh1::KANMX6 *GAL-NOG1* TRP1 pRS315_ *nog1Δ595-647* LEU2	Gal-Nog1 *reh1Δ* +pRS315 *nog1Δ595-647*
JWY11925	MATa ura3-52 trp1-1 lys2-801 his3-Δ200 leu2-Δ1	Gal-Nog1 *reh1Δ* +pRS315 *nog1Δ595-647*

	reh1::KANMX6 *GAL-NOG1* TRP1 pRS315_ *nog1Δ595-647* LEU2	
JWY11926	MATa ura3-52 trp1-1 lys2-801 his3-Δ200 leu2-Δ1 *GAL-NOG1*::TRP1 nop7::Nop7-TAP URA3 pRS315_*NOG1* LEU2	Gal-Nog1 Nop7-TAP +pRS315 *NOG1*
JWY11927	MATa ura3-52 trp1-1 lys2-801 his3-Δ200 leu2-Δ1 *GAL-NOG1*::TRP1 nop7::Nop7-TAP URA3 pRS315_ *nog1Δ575-674* LEU2	Gal-Nog1 Nop7-TAP +pRS315 *nog1Δ575-674*
JWY11928	MATa ura3-52 trp1-1 lys2-801 his3-Δ200 leu2-Δ1 *GAL-NOG1*::TRP1 nop7::Nop7-TAP URA3 pRS315_ *nog1Δ575-674* LEU2	Gal-Nog1 Nop7-TAP +pRS315 *nog1Δ575-674*
JWY11929	MATa ura3-52 trp1-1 lys2-801 his3-Δ200 leu2-Δ1 *GAL-NOG1*::TRP1 nop7::Nop7-TAP URA3 rei1::KANMX6 pRS315_ *nog1Δ575-674* LEU2	Gal-Nog1 Nop7-TAP *rei1Δ* +pRS315 *nog1Δ575-674*
JWY11930	MATa ura3-52 trp1-1 lys2-801 his3-Δ200 leu2-Δ1 *GAL-NOG1*::TRP1 nop7::Nop7-TAP URA3 rei1::KANMX6 pRS315_ *nog1Δ575-674* LEU2	Gal-Nog1 Nop7-TAP *rei1Δ* +pRS315 *nog1Δ575-674*
JWY11931	MATa ura3-52 trp1-1 lys2-801 his3-Δ200 leu2-Δ1	Gal-Nog1 Nmd3-TAP *rei1Δ* +pRS315 *nog1Δ575-674*

	GAL-NOG1::TRP1 nmd3::Nmd3-TAP URA3 rei1::KANMX6 pRS315_ *nog1Δ575-674* LEU2	
JWY11932	MATa ura3-52 trp1-1 lys2-801 his3-Δ200 leu2-Δ1 *GAL-NOG1*::TRP1 nmd3::Nmd3-TAP URA3 rei1::KANMX6 pRS315_ *nog1Δ575-674* LEU2	Gal-Nog1 Nmd3-TAP *rei1Δ* +pRS315 *nog1Δ575-674*
JWY11932	MATa ura3-52 trp1-1 lys2-801 his3-Δ200 leu2-Δ1 *GAL-NOG1*::TRP1 nmd3::Nmd3-TAP URA3	Gal-Nog1 Nmd3-TAP
JWY11933	MATa ura3-52 trp1-1 lys2-801 his3-Δ200 leu2-Δ1 *GAL-NOG1*::TRP1 nmd3::Nmd3-TAP URA3	Gal-Nog1 Nmd3-TAP
JWY11934	MATa ura3-52 trp1-1 lys2-801 his3-Δ200 leu2-Δ1 *GAL-NOG1*::TRP1 nmd3::Nmd3-TAP URA3	Gal-Nog1 Nmd3-TAP
JWY11935	MATa ura3-52 trp1-1 lys2-801 his3-Δ200 leu2-Δ1 *GAL-NOG1*::TRP1 nmd3::Nmd3-TAP URA3 rei1::KANMX6	Gal-Nog1 Nmd3-TAP *rei1Δ*
JWY11936	MATa ura3-52 trp1-1 lys2-801 his3-Δ200 leu2-Δ1 *GAL-NOG1*::TRP1 nmd3::Nmd3-TAP URA3 rei1::KANMX6	Gal-Nog1 Nmd3-TAP *rei1Δ*
JWY11937	MATa ura3-52 trp1-1 lys2-801 his3-Δ200 leu2-Δ1	*nog1Δ595-647* Nog2-TAP

	nog1::Nog1Δ595-647 KANMX nog2::Nog2-TAP URA3	
JWY11938	MATa ura3-52 trp1-1 lys2-801 his3-Δ200 leu2-Δ1 nog1::Nog1Δ595-647 KANMX nog2::Nog2-TAP URA3	*nog1Δ595-647* Nog2-TAP
JWY11939	MATa ura3-52 trp1-1 lys2-801 his3-Δ200 leu2-Δ1 nog1::Nog1Δ595-647 KANMX nmd3::Nmd3-TAP URA3	*nog1Δ595-647* Nmd3-TAP
JWY11940	MATa ura3-52 trp1-1 lys2-801 his3-Δ200 leu2-Δ1 nog1::Nog1Δ595-647 KANMX nmd3::Nmd3-TAP URA3	*nog1Δ595-647* Nmd3-TAP
JWY11941	MATa ura3-52 trp1-1 lys2-801 his3-Δ200 leu2-Δ1 nog1::Nog1Δ595-647 KANMX rei1::Rei1Δ341-393 HIS3 reh1::Reh1Δ380-432 TRP1 nop7::Nop7-TAP URA3	Triple Tail mutant Nop7-TAP
JWY11942	MATa ura3-52 trp1-1 lys2-801 his3-Δ200 leu2-Δ1 nog1::Nog1Δ595-647 KANMX rei1::Rei1Δ341-393 HIS3 reh1::Reh1Δ380-432 TRP1 nop7::Nop7-TAP URA3	Triple Tail mutant Nop7-TAP
JWY11943	MATa ura3-52 trp1-1 lys2-801 his3-Δ200 leu2-Δ1 nog1::Nog1Δ595-647 KANMX rei1::Rei1Δ341-393 HIS3	Triple Tail mutant Nog2-TAP

	reh1::Reh1Δ380-432 TRP1 nog2::Nog2-TAP URA3	
JWY11944	MATa ura3-52 trp1-1 lys2-801 his3-Δ200 leu2-Δ1 nog1::Nog1Δ595-647 KANMX rei1::Rei1Δ341-393 HIS3 reh1::Reh1Δ380-432 TRP1 nog2::Nog2-TAP URA3	Triple Tail mutant Nog2-TAP
JWY11945	MATa ura3-52 trp1-1 lys2-801 his3-Δ200 leu2-Δ1 nog1::Nog1Δ595-647 KANMX rei1::Rei1Δ341-393 HIS3 reh1::Reh1Δ380-432 TRP1 nmd3::Nmd3-TAP URA3	Triple Tail mutant Nmd3-TAP
JWY11946	MATa ura3-52 trp1-1 lys2-801 his3-Δ200 leu2-Δ1 nog1::Nog1Δ595-647 KANMX rei1::Rei1Δ341-393 HIS3 reh1::Reh1Δ380-432 TRP1 nmd3::Nmd3-TAP URA3	Triple Tail mutant Nmd3-TAP
JWY11947	MATa ura3-52 trp1-1 lys2-801 his3-Δ200 leu2-Δ1 nog1::Nog1Δ595-647 KANMX nop7::Nop7-TAP URA3	*nog1Δ595-647* Nop7-TAP
JWY11948	MATa ura3-52 trp1-1 lys2-801 his3-Δ200 leu2-Δ1 nog1::Nog1Δ595-647 KANMX nop7::Nop7-TAP URA3	*nog1Δ595-647* Nop7-TAP
JWY11949	MATa his3Δ1 leu2Δ0 met15Δ0 ura3Δ0 nsa1::Nsa1Δ434-463 KANMX6	*nsa1Δ434-463*

JWY11950	MATa his3Δ1 leu2Δ0 met15Δ0 ura3Δ0 nsa1::Nsa1Δ434-463 KANMX6	*nsa1Δ434-463*
JWY11951	MATa ura3-52 trp1-1 lys2-801 his3-Δ200 leu2-Δ *GAL-DRS1* TRP1 nsa1::Nsa1-TAP URA3 pRS315_*drs1Δ585* LEU2	Gal-Drs1 Nsa1-TAP +pRS315 *drs1Δ585*
JWY11952	MATa ura3-52 trp1-1 lys2-801 his3-Δ200 leu2-Δ *GAL-DRS1* TRP1 nsa1::Nsa1-TAP URA3 pRS315_*drs1Δ585* LEU2	Gal-Drs1 Nsa1-TAP +pRS315 *drs1Δ585*
JWY11953	MATa ura3-52 trp1-1 lys2-801 his3-Δ200 leu2-Δ *GAL-DRS1* TRP1 nsa1::Nsa1-TAP nsa1::Nsa1Δ434-463 KANMX6	Gal-Drs1 Nop7-TAP *nsa1Δ434-463*
JWY11954	MATa ura3-52 trp1-1 lys2-801 his3-Δ200 leu2-Δ *GAL-DRS1* TRP1 nsa1::Nsa1-TAP nsa1::Nsa1Δ434-463 KANMX6	Gal-Drs1 Nop7-TAP *nsa1Δ434-463*
JWY11955	MATa ura3-52 trp1-1 lys2-801 his3-Δ200 leu2-Δ *GAL-DRS1* TRP1 nsa1::Nsa1-TAP nsa1::Nsa1Δ434-463 KANMX6 pRS315_*drs1Δ585* LEU2	Gal-Drs1 Nop7-TAP *nsa1Δ434-463* +pRS315 *drs1Δ585*
JWY11956	MATa ura3-52 trp1-1 lys2-801 his3-Δ200 leu2-Δ	Gal-Drs1 Nop7-TAP *nsa1Δ434-463* +pRS315 *drs1Δ585*

	GAL-DRS1 TRP1 nsa1::Nsa1-TAP nsa1::Nsa1Δ434-463 KANMX6 pRS315_*drs1Δ585* LEU2	
JWY11957	MATa ura3-52 trp1-1 lys2-801 his3-Δ200 leu2-Δ *GAL-DRS1* TRP1 nsa1::Nsa1-TAP nsa1::Nsa1Δ434-463 KANMX6 pRS315_*drs1Δ672* LEU2	Gal-Drs1 Nop7-TAP *nsa1Δ434-463* +pRS315 *drs1Δ672*
JWY11958	MATa ura3-52 trp1-1 lys2-801 his3-Δ200 leu2-Δ *GAL-DRS1* TRP1 nsa1::Nsa1-TAP nsa1::Nsa1Δ434-463 KANMX6 pRS315_*drs1Δ672* LEU2	Gal-Drs1 Nop7-TAP *nsa1Δ434-463* +pRS315 *drs1Δ672*
JWY11959	MATa ura3-52 trp1-1 lys2-801 his3-Δ200 leu2-Δ1 nog1::Nog1Δ627-647 KANMX	*nog1Δ627-647*
JWY11960	MATa ura3-52 trp1-1 lys2-801 his3-Δ200 leu2-Δ1 nog1::Nog1Δ627-647 KANMX	*nog1Δ627-647*
JWY11961	MATa ura3-52 trp1-1 lys2-801 his3-Δ200 leu2-Δ1 nog1::Nog1Δ640-647 KANMX	*nog1Δ640-647*
JWY11962	MATa ura3-52 trp1-1 lys2-801 his3-Δ200 leu2-Δ1 nog1::Nog1Δ640-647 KANMX	*nog1Δ640-647*
JWY11963	MATa ura3-52 trp1-1 lys2-801 his3-Δ200 leu2-Δ1 *GAL-HA-NSA1* KANMX6	Gal-HA-Nsa1

JWY11964	MATa ura3-52 trp1-1 lys2-801 his3-Δ200 leu2-Δ1 *GAL-HA-NSA1* KANMX6	Gal-HA-Nsa1
JWY11965	MATa ura3-52 trp1-1 lys2-801 his3-Δ200 leu2-Δ1 *GAL-HA-NSA1* KANMX6 nop7::Nop7-TAP URA3	Gal-HA-Nsa1 Nop7-TAP
JWY11966	MATa ura3-52 trp1-1 lys2-801 his3-Δ200 leu2-Δ1 *GAL-HA-NSA1* KANMX6 nop7::Nop7-TAP URA3	Gal-HA-Nsa1 Nop7-TAP
JWY11967	MATa ura3-52 trp1-1 lys2-801 his3-Δ200 leu2-Δ1 *GAL-DRS1* TRP1 nop7::Nop7-TAP URA3 pRS315_Nop1-mRFP L25eGFP LEU2	Gal-Drs1 Nop7-TAP +pRS315 Nop1-mRFP L25-eGFP
JWY11968	MATa ura3-52 trp1-1 lys2-801 his3-Δ200 leu2-Δ1 *GAL-DRS1* TRP1 nop7::Nop7-TAP URA3 pRS315_Nop1-mRFP L25eGFP LEU2	Gal-Drs1 Nop7-TAP +pRS315 Nop1-mRFP L25-eGFP
JWY11969	MATa ura3-52 trp1-1 lys2-801 his3-Δ200 leu2-Δ1 nog1::Nog1Δ595-647 KANMX rei1::Rei1Δ341-393 HIS3 reh1::Reh1Δ380-432 TRP1 pRS315_Nop1-mRFP L25eGFP LEU2	Triple Tail mutant Nop7-TAP +pRS315 Nop1-mRFP L25-eGFP
JWY11970	MATa ura3-52 trp1-1 lys2-801 his3-Δ200 leu2-Δ1 nog1::Nog1Δ595-647 KANMX rei1::Rei1Δ341-393 HIS3	Triple Tail mutant Nop7-TAP +pRS315 Nop1-mRFP L25-eGFP

	reh1::Reh1Δ380-432 TRP1 pRS315_Nop1-mRFP L25eGFP LEU2	
JWY11971	MATa ura3-52 trp1-1 lys2-801 his3-Δ200 leu2-Δ1 *GAL-NOG2* TRP1 nmd3::Nmd3-TAP URA3	Gal-Nog2 Nmd3-TAP
JWY11972	MATa ura3-52 trp1-1 lys2-801 his3-Δ200 leu2-Δ1 *GAL-NOG2* TRP1 nmd3::Nmd3-TAP URA3	Gal-Nog2 Nmd3-TAP
JWY11973	MATa ura3-52 trp1-1 lys2-801 his3-Δ200 leu2-Δ1 l4b::KANMX6 l4a::GAL-HA3-RPL4A TRP1 nmd3::Nmd3-TAP URA3	Gal-HA-L4A Nmd3-TAP
JWY11974	MATa ura3-52 trp1-1 lys2-801 his3-Δ200 leu2-Δ1 l4b::KANMX6 l4a::GAL-HA3-RPL4A TRP1 nmd3::Nmd3-TAP URA3	Gal-HA-L4A Nmd3-TAP
JWY11975	MATa ura3-52 trp1-1 lys2-801 his3-Δ200 leu2-Δ1 l4b::KANMX6 l4a::GAL-HA3-RPL4A TRP1 nmd3::Nmd3-TAP URA3 pRS315_L4AΔ63-87 LEU2	Gal-HA-L4A Nmd3-TAP +pRS315 *rpl4Δ63-87*
JWY11976	MATa ura3-52 trp1-1 lys2-801 his3-Δ200 leu2-Δ1 l4b::KANMX6 l4a::GAL-HA3-RPL4A TRP1 nmd3::Nmd3-TAP URA3 pRS315_L4AΔ63-87 LEU2	Gal-HA-L4A Nmd3-TAP +pRS315 *rpl4Δ63-87*

JWY11977	MATa ura3-52 trp1-1 lys2-801 his3-Δ200 leu2-Δ1 l4b::KANMX6 l4a::GAL-HA3-RPL4A TRP1 pRS315_L4A R69E LEU2	Gal-HA-L4A Nog2-TAP +pRS315 *rpl4 R69E*
JWY11978	MATa ura3-52 trp1-1 lys2-801 his3-Δ200 leu2-Δ1 l4b::KANMX6 l4a::GAL-HA3-RPL4A TRP1 pRS315_L4A R69E LEU2	Gal-HA-L4A Nog2-TAP +pRS315 *rpl4 R69E*
JWY11979	MATa ura3-52 trp1-1 lys2-801 his3-Δ200 leu2-Δ1 l4b::KANMX6 l4a::GAL-HA3-RPL4A TRP1 pRS315_L4A R73E LEU2	Gal-HA-L4A Nog2-TAP +pRS315 *rpl4 R73E*
JWY11980	MATa ura3-52 trp1-1 lys2-801 his3-Δ200 leu2-Δ1 l4b::KANMX6 l4a::GAL-HA3-RPL4A TRP1 pRS315_L4A R73E LEU2	Gal-HA-L4A Nog2-TAP +pRS315 *rpl4 R73E*
JWY11981	MATa ura3-52 trp1-1 lys2-801 his3-Δ200 leu2-Δ1 l4b::KANMX6 l4a::GAL-HA3-RPL4A TRP1 pRS315_L4A R69E + R73E LEU2	Gal-HA-L4A Nog2-TAP +pRS315 *rpl4 R69E,R73E*
JWY11982	MATa ura3-52 trp1-1 lys2-801 his3-Δ200 leu2-Δ1 l4b::KANMX6 l4a::GAL-HA3-RPL4A TRP1 pRS315_L4A R69E + R73E LEU2	Gal-HA-L4A Nog2-TAP +pRS315 *rpl4 R69E,R73E*
JWY11983	MATa ura3-52 trp1-1 lys2-801 his3-Δ200 leu2-Δ1	Nog2-TAP (JWY background)

	Nog2::Nog2-TAP URA3	
JWY11984	MATa ura3-52 trp1-1 lys2-801 his3-Δ200 leu2-Δ1 Nog2::Nog2-TAP URA3	Nog2-TAP (JWY background)
JWY11985	MATa ura3-52 trp1-1 lys2-801 his3-Δ200 leu2-Δ1 rpl39::KANMX6 nog2::Nog2-TAP URA3	Nog2-TAP *rpl39Δ* From Jesus de la Cruz
JWY11986	MATa ura3-52 trp1-1 lys2-801 his3-Δ200 leu2-Δ1 rpl39::KANMX6 nog2::Nog2-TAP URA3	Nog2-TAP *rpl39Δ* From Jesus de la Cruz

Table 0.1 Yeast strain list

Table 0.2. Bacteria strain list

Strain	Description	Notes
JWB10301	Nmd3(AAA)-GFP LEU2 CEN	From Arlen Johnson
JWB10302	Nmd3(AAA)-GFP LEU2 CEN	From Arlen Johnson
JWB10303	Nmd3(AAA)-GFP URA3 CEN	From Arlen Johnson
JWB10304	Nmd3(AAA)-GFP URA3 CEN	From Arlen Johnson
JWB10305	Tif6-GFP LEU2 CEN	From Arlen Johnson
JWB10306	Tif6-GFP LEU2 CEN	From Arlen Johnson
JWB10307	Tif6-GFP URA3 CEN	From Arlen Johnson
JWB10308	Tif6-GFP URA3 CEN	From Arlen Johnson
JWB10309	Arx1-GFP URA3 CEN	From Arlen Johnson

JWB10310	Arx1-GFP URA3 CEN	From Arlen Johnson
JWB10311	Arx1-GFP LEU2 CEN	From Arlen Johnson
JWB10312	Arx1-GFP LEU2 CEN	From Arlen Johnson
JWB10313	pRS315 *rpl4Δ63-75*	
JWB10314	pRS315 *rpl4Δ63-75*	
JWB10315	pRS315 *rpl4Δ63-87*	
JWB10316	pRS315 *rpl4Δ63-87*	
JWB10317	pRS315 *nog1Δ2-35*	
JWB10318	pRS315 *nog1Δ2-35*	